

FY 2019 Doctoral Thesis

**Investigation of Planform Dependency
for Low-drag/ Low-boom Supersonic Wing
Using Multi-Additional-Sampling Multi-Fidelity Approach**

多点追加サンプリング **Multi-fidelity** 設計法を用いた
低抵抗・低ソニックブーム超音速主翼の平面形依存性調査

March 2020

Tokyo Metropolitan University
Graduate School of System Design
Department of Aerospace Engineering
Doctoral Program

Student No. 15991503: Yuki KISHI

Supervisor: Masahiro KANAZAKI

Abstract

To realize innovative supersonic transport (SST), design knowledge to reduce aerodynamic drag and the impact of sonic booms is required. However, few studies have been conducted on the planform dependency on supersonic wing's for low aerodynamic drag and low sonic booms. To enhance knowledge on supersonic wings, a highly efficient design method is desirable because simultaneous evaluations of the aerodynamic drag and sonic boom tend to be time-consuming. Thus, this dissertation has two main objectives. The first objective is to understand the planform dependency on a supersonic wing to simultaneously reduce the aerodynamic drag and sonic-boom under cruise conditions. The second is to apply the design method with improved efficiency, which integrates the multi-fidelity approach and the concept of multi-additional sampling, to solve the optimum design problem. This dissertation is divided into five chapters.

Chapter 1 introduces the studies that motivated this study. It also surveys the global situation surrounding SST research and development and optimization methods for aircraft design.

Chapter 2 focuses on drag reduction for two supersonic wing planforms: a cranked arrow wing with a large backward-swept angle and a single-tapered wing with a small backward-swept angle. For each planform, the optimal airfoil distributions along the span direction were designed under supersonic and transonic cruise conditions. In the design process, the efficient global optimization (EGO) method using a Kriging surrogate model was employed. To realize minimum drag in the entire cruise, the objective functions were the pressure drag coefficients at Mach 1.6 (over sea) and Mach 0.8 (over ground). The design results show that, for both planforms, no trade-off occurred between the objective functions. According to the functional analysis of variance, for both planforms, the design variable contributing the most to drag reduction at Mach 1.6 was the camber height at the kink. However, the design value contributing the most to drag reduction at Mach 0.8 differed between the planforms. In the cranked arrow wing case, it was the camber height at the kink, whereas in the single-tapered wing case, it was the twisted angle or camber height at the tip.

Chapter 3 presents the study developed based on Chapter 2. It discusses the optimal airfoil distributions for the cranked arrow wing and single-tapered wing while considering the aerodynamic interference between the engine, fuselage, and wing. The design problems were solved using a multi-fidelity approach consisting of a hybrid surrogate model assisted by evolutionary computation. To evaluate the aerodynamic performance, the compressible Euler equation was used to consider spatial pressure propagation and linearized compressible potential equation to acquire the surface pressure distribution were employed as high- and low-level fidelity solvers, respectively. The objective function was the pressure drag coefficient during the Mach 1.6 level flight. Several geometric parameters of modified PARSEC methods were used as the

design variables. By design optimization, the contributions of different cross-sectional parameters to drag reduction were determined. It was found that for both wing planforms, shape of the forward camber and twist angle around the middle of the wing had the most significant influence on drag reduction because most of the aerodynamic force was generated near the wing mid-span. For a wing with a large backward-swept angle, a cross-sectional geometry involving a small positive camber at the leading edge and a small twisted angle were optimum. For a wing with a small backward-swept angle, a cross-sectional geometry involving a negative camber at the leading edge, a small leading edge radius, and a higher twisted angle than those for a large backward-swept wing were optimum because of the generation of a shock wave at the leading edge.

Chapter 4 focuses on the simultaneous reduction of the drag and sonic boom. A parametric study was performed to investigate the relationship between the sonic boom performance, and backward-swept/forward-swept angle. Using the knowledge gained from these parametric studies, optimal airfoil distributions for the forward-swept and backward-swept wings were designed to determine the planform dependency on a low-drag, low-boom wing while considering the airfoil distribution. For the sonic-boom evaluation, the augmented Burgers equation and multipole analysis were applied to the near-field pressure distribution calculated with the Euler simulation to evaluate each sample. However, this process was extremely time-consuming. Thus, a new multi-fidelity approach was developed, which was integrated with a multi-additional sampling concept and was more efficient than the conventional multi-fidelity approach for application to the design problem. Low-drag and low-boom solutions were then obtained for both planforms. It was found that the forward-swept wing can reduce the sonic boom and aerodynamic drag more efficiently than the backward-swept wing. Based on the functional analysis of variance, the design variables that contributed to the reduction of the various objective functions were different.

Finally, Chapter 5 discusses the conclusions of the series of studies. By solving the optimal design problems for several planforms, knowledge regarding the planform dependency on a supersonic wing for the simultaneous reduction of aerodynamic drag and sonic boom during cruising was obtained. In addition, the multi-additional-sampling, multi-fidelity approach was proven to solve these optimization problems more efficiently.

Acknowledgement

I would like to thank a number of people who directly and indirectly contributed to the completion of this thesis. First of all, I would like to express my sincerely thank to my supervisor, Assoc. Prof. Masahiro Kanazaki, for all of his patient guidance, understanding and continuous support throughout my whole study. I would also like to acknowledge Dr. Yoshikazu Makino, Mr. Satoshi Kondo, and Dr. Tatsunori Yuhara from the Japan Aerospace Exploration Agency (JAXA) for their interesting discussions and help with regard my research.

I would like to dedicate my special thanks to all of my seniors and juniors in my laboratory. Certainly, special mention goes to Dr. Atthaphon Ariyarat, Mr. Shinya Kitazaki, Mr. Yusuke Yamada, Mr. Nao Setoguchi, and Mr. Seiya Nomura for their help and friendship.

I would like to dedicate my grateful and deep appreciation to my parents and brothers for their constant support and encouragement throughout my life.

Finally, I would like to dedicate my special thanks to my caregiver, Mr. Tadahiro Ichihara. Thanks to him, I could feel comfortable in my research activities and university life.

Contents

Chapter 1	Introduction	1
1.1	Current Situation of SST Research and Development	1
1.2	Reviews of Optimization Techniques	5
1.3	Objective of this study	7
Chapter 2	Planform Dependency Investigation of Low-Drag Airfoil at Supersonic and Transonic speeds	12
2.1	Introduction	12
2.2	Design Method	13
2.2.1	Overview of Efficient Global Optimization	13
2.2.2	Latin Hypercube Sampling for Initial Samples	14
2.2.3	Kriging Surrogate Model	15
2.2.4	Expected Improvement (EI)	16
2.2.5	Divided Range Multi-Objective Genetic Algorithm (DRMOGA)	17
2.3	Analysis Method for Design Results	18
2.4	Aerodynamic Evaluation	19
2.5	Design Problems	20
2.5.1	Design Targets and Design Cases	20
2.5.2	Design Space	20
2.5.3	Objective Functions and Constrains	21
2.6	Results and Discussion	23
2.6.1	Sampling Results	23
2.6.2	Knowledge Discovery by Functional ANOVA	24
2.6.3	Design Examples	25

2.6.3.1	Comparison of Low-drag Solutions at Both Speeds between Selected Planforms	25
2.6.3.2	Comparison of the Lowest-drag Solutions in Case 1 between Supersonic and Transonic Conditions	28
2.6.3.3	Comparison of the Lowest-drag Solutions in Case 2 between Supersonic and Transonic Conditions	31
2.7	Conclusion	34
Chapter 3 Planform Dependency Investigation of Low-Drag Supersonic Airfoil for Wing-Body-Nacelle Configuration		
3.1	Introduction	37
3.2	Design Method	38
3.2.1	Overview of Multi-Fidelity Efficient Global Optimization	38
3.2.2	Surrogate Model	39
3.2.2.1	Radial Basis Function Model (RBF model)	39
3.2.2.2	Hybrid Surrogate Model	40
3.2.3	Optimization Method	41
3.3	Visualization Method of Design Results	41
3.4	Aerodynamic Evaluation	42
3.4.1	High-Fidelity Evaluation	42
3.4.2	Low-Fidelity Evaluation	42
3.5	Design Problems	43
3.5.1	Design Targets and Design Cases	43
3.5.2	Modified Parametric Section (PARSEC) for Airfoil Definition	43
3.5.3	Design Space	44

3.5.4	Objective Function and Constrains	45
3.6	Results and Discussion	46
3.6.1	Validation of Configuration Fidelity	46
3.6.2	Sampling Results	47
3.6.3	Difference between Low-Drag Airfoil Distribution for Each Case	48
3.6.3.1	Geometric Difference	48
3.6.3.2	Aerodynamic Characteristics Difference	50
3.6.4	Trend of Solution Space	56
3.6.4.1	Knowledge Discovery by Functional ANOVA	56
3.6.4.2	Knowledge Discovery by PCP	57
3.6.5	Conclusion	59
Chapter 4	Planform Dependency of Low-Drag Low-Boom Supersonic Airfoil for a Wing-Body-Nacelle Configuration	62
4.1	Introduction	62
4.2	Evaluation Method of Aerodynamics and Sonic Boom	63
4.2.1	Overview	63
4.2.2	Aerodynamic Evaluation	64
4.2.3	Sonic Boom Evaluation	65
4.2.4	Validation of Grid Dependency	66
4.2.4.1	Standard Richardson Extrapolation (SRE)	66
4.2.4.2	Results	67
4.3	Parametric Study of Aerodynamic Performance of a Forward-Swept Wing	68
4.3.1	Specifications of Target Aircrafts	68
4.3.2	Results and Discussion	70

4.3.2.1	Comparisons between Backward- and Forward- Swept Wings	70
4.3.2.2	Comparisons of Pressure Fields	71
4.3.2.2.1	Leading boom	74
4.3.2.2.2	Trailing boom	74
4.3.2.2.3	$\Lambda = 30^\circ, 20^\circ,$ and 10° configurations	78
4.4	Low-Drag Low-Boom Wing Design	83
4.4.1	Design Method	83
4.4.1.1	Multi-objective Multi-fidelity Optimization with Multi-additional Sampling	83
4.4.1.1.1	Overview	83
4.4.1.1.2	Demonstration of Proposed Approach Using a Test Problem	85
4.4.1.2	Expected Hyper-Volume Improvement (EHVI)	90
4.4.2	Design Problems	92
4.4.2.1	Design Targets and Design Cases	92
4.4.2.2	Design Space	93
4.4.2.3	Objective Function and Constrains	95
4.4.3	Results and Discussion	95
4.4.3.1	Sampling Results	95
4.4.3.2	Knowledge Discovery by Functional ANOVA	96
4.4.3.3	Comparison between Representative Solutions	98
4.5	Conclusion	104
Chapter 5	Conclusion	107

List of Figures

Figure 1-1 Aerion AS2.	4
Figure 1-2 Overture (near side) and XB-1 (far side), developed by Boom Technology.	4
Figure 2-1 Flow chart of EGO.	14
Figure 2-2 Concept of Kriging surrogate model.	16
Figure 2-3 Improvement of the surrogate model.	17
Figure 2-4 Base airfoils for each case.	21
Figure 2-5 Relationship between the location of the center of pressure and the horizontal tail wing angle, determined by a first-order regression model.	23
Figure 2-6 Sampling results.	24
Figure 2-7 Functional ANOVA ($dv\sim$ means design variable defined in Table 2-2).	25
Figure 2-8 Surface C_p distributions for low-drag solutions in the both cruise conditions.	26
Figure 2-9 Cross sectional airfoils of representative solutions.	27
Figure 2-10 Cross sectional C_p distribution at the kink (63% semi-span).	28
Figure 2-11 Surface C_p distributions for the lowest-drag solutions in the transonic cruise condition.	29
Figure 2-12 Airfoil geometries of each cross section for Designs 1-2 and 1-3.	30
Figure 2-13 Surface C_p distributions for lowest-drag solutions in the supersonic cruise condition.	32
Figure 2-14 Airfoil geometries of each cross section for Designs 2-2 and 2-3.	33
Figure 3-1 Flow chart of multi-fidelity efficient global optimization.	39
Figure 3-2 Concept of the hybrid surrogate model.	41
Figure 3-3 Overview of the two evaluated wing planforms.	43
Figure 3-4 Aerodynamic performance of initial samples via Euler simulation.	46

Figure 3-5 Aerodynamic performance of additional samples via Euler simulation.	48
Figure 3-6 Results of LOOCV for the hybrid surrogate model.	48
Figure 3-7 Airfoil geometries of representative solutions at Cross section #2.	49
Figure 3-8 Surface C_p distributions of representative solutions (engine-integrated) by Euler simulation.	52
Figure 3-9 Cross-sectional C_p distribution for the representative solutions along Cross section #2.	53
Figure 3-10 Surface C_p distributions of representative solutions (clean configuration) by Euler simulation.	53
Figure 3-11 Values of C_{DP} for each component of the representative solutions by Euler simulation.	54
Figure 3-12 Surface C_p distributions near the engine intake and nacelle.	54
Figure 3-13 Cross-sectional area distribution along the body axis.	54
Figure 3-14 Cross-sectional C_p distributions near the engine intake (from front side). ...	55
Figure 3-15 Contribution ratios of design variables to C_{DP} (the functional ANOVA results).	57
Figure 3-16 Local deviation of C_{DP}	57
Figure 3-17 Visualization of design variables and C_{DP} for all samples determined by PCP.	58
Figure 4-1 Flowchart of the numerical evaluation.	64
Figure 4-2 Calculation results of the grid validation.	67
Figure 4-3 Baseline configuration.	68
Figure 4-4 Overview of the evaluated wing planforms.	69
Figure 4-5 Airfoil geometries of the baseline.	69

Figure 4-6 Evaluation results of each solution.	71
Figure 4-7 Pressure signatures at the near-field of the aircraft and the ground.	72
Figure 4-8 Pressure signatures during the process of propagating to the ground.	72
Figure 4-9 Lift distributions of the aircraft along the body axis.	73
Figure 4-10 Surface C_p distribution for representative configurations.	73
Figure 4-11 Surface C_p distribution on the aft body and cross-sectional C_p distribution.	76
Figure 4-12 Pressure signature at the ground for $\Lambda = 30^\circ, 20^\circ,$ and 10° configurations. .	81
Figure 4-13 Function curve in which the second order differential takes negative, positive, and negative values in sequence.	81
Figure 4-14 Trailing pressure signatures on the ground of configurations ($\Lambda \leq 10^\circ$).	82
Figure 4-15 Flow chart of multi-objective multi-fidelity optimization methods.	84
Figure 4-16 Example of distribution of random solutions $m = 5$	87
Figure 4-17 Additional sampling result for each case when 50 additional samples were obtained.	88
Figure 4-18 LOOCV results for each proposed approach case.	89
Figure 4-19 Additional sampling result for each case (Number of main loop iterations was matched).	89
Figure 4-20 History of hypervolume.	90
Figure 4-21 Concept of HVI (when the number of the object functions is two).	91
Figure 4-22 Cross sections of airfoil definition.	92
Figure 4-23 Sampling result.	96
Figure 4-24 Contribution ratios of design variables to each objective function.	98
Figure 4-25 Surface C_p distributions for representative solutions.	100

Figure 4-26 Airfoil geometries of representative solutions.	101
Figure 4-27 Cross sectional C_p distributions for representative solutions.	102
Figure 4-28 Pressure signature for minimum PL solutions.	103
Figure 4-29 Pressure signatures for minimum PL solutions during the process of propagating to the ground.	103

List of Tables

Table 2-1 Dimensions of the planforms.	20
Table 2-2 Design space.	21
Table 3-1 Design space.	45
Table 4-1 Specifications of wing planforms for the evaluated aircrafts.	69
Table 4-2 Positions of the center of gravity and the aerodynamic center for each configuration.	70
Table 4-3 AoA of the horizontal tail wing for each configuration.	77
Table 4-4 Lift coefficients of each component.	78
Table 4-5 Optimization conditions.	88
Table 4-6 Design space regarding thickness distribution.	93
Table 4-7 Design space regarding camber and twisted-down angle of airfoil.	94

Nomenclature

a_n	Real coefficient
b	Span length
b_0	Real coefficient
b_n	Real coefficient
C_{DP}	Pressure drag coefficient
c_0	Speed of sound
$(\Delta c)_\nu$	Increment of speed of sound related relaxation in chemical species ν
$EHVI$	Value of the expected hypervolume improvement
EI	Value of the expected improvement
\mathbf{f}	Vector that contains the evaluation value of each sample point
f_{coarse}	Solution based on the coarse grid
f_{fine}	Solution based on the fine grid
F_M	Margin factor
f_{max}	Maximum value among all available sample points
f_{min}	Minimum value among all available sample points
f_{MOP2_1}	First objective function in MOP2 in Van Valedhuizen's test suite
$f_{\text{MOP2}_1} _{\text{Low}}$	Low-fidelity function of f_{MOP2_1}
f_{MOP2_2}	Second objective function in MOP2 in Van Valedhuizen's test suite
$f_{\text{MOP2}_2} _{\text{Low}}$	Low-fidelity function of f_{MOP2_2}
f_{obj_i}	i -th objective function
$f_{\text{obj}_i} _{\text{ref}}$	i -th objective function value at the reference point
F_{rv_i}	Gaussian random variable
f_{SRE}	Approximate solution of SRE when the distance between grids approaches zero
\mathbf{H}	Inviscid flux vector
HVI	Value of the hypervolume improvement
L	Total Lift
m	Number of design variables
M	Number of objective functions
M_∞	Mach number of the freestream
\mathbf{n}	Outward normal vector
N	Number of design samples
N_{initial}	Number of initial samples
n_{ult}	Ultimate load factor

p	Pressure fluctuation from atmospheric pressure
p_{dvi}	Contribution ratio to objective function for i -th design variable
\mathbf{q}	Conservative vector
\mathbf{r}	Correlation vector between an arbitrary point and a known sample point
\mathbf{R}	Matrix that denotes the correlation between known sample points
s	Coordinate along the ray
\hat{s}	Root of minimum square error of the surrogate model
S	Element of surface
S_{wing}	Wing area
t_{root}	Thickness of root cross section
V	Element of volume
$V(s)$	Blokhintsev invariant
W	Weight of the aircraft
$w_{\text{RBF}i}$	Weight coefficient of the i -th design sample
W_{TO}	Takeoff weight
W_{w}	Weight of wing
X_{CG}	Position coordinate of the center of gravity
X_{CP}	Position coordinate of the center of pressure
\mathbf{x}_{dv}	Vector in design space
\mathbf{x}_{dv}^i	Vector of i -th sample in design space
x_{dvi}	i -th design variable
\hat{y}	Approximate solution on a surrogate model
\hat{y}_{hybrid}	Approximate solution on hybrid surrogate model
\hat{y}_{kriging}	Approximate solution on Kriging surrogate model
\hat{y}_{RBF}	Approximate solution on radial basis function model
z_{c}	Camber height
z_{t}	Half of airfoil thickness
α	Angle of attack of the aircraft
β_{RBF}	A positive coefficient
γ	Heat capacity ratio
δ	Thermal viscosity diffusivity of sound
ε	Local deviation from the global model
Λ	Backward-swept angle of the leading edge
μ	Constant global model
μ	Total mean

μ_i	Variance of a design variable x_{dv_i}
ν	Chemical species
ρ_0	Atmospheric density
τ	Retardation time
τ_ν	Relaxation time in chemical species ν
Φ	Cumulative distribution function of the standard normal distribution
ϕ	Probability density function of the standard normal distribution
φ	Velocity potential

Chapter 1 Introduction

1.1 Current Situation of SST Research and Development

Despite the retirement of the first supersonic passenger jet airliner, the Concorde, in 2003, expectations of civilian supersonic transport (SST) still exist. This is because it has been proven that the demand for air travel will increase and become diversified within the next 20 years [1, 2]. From the passengers' point of view, SST provides a greater number of active choices at departures and destinations due to shorter flight times. For people who cannot bear long flights because of physical disabilities, SST expands their travel radius. From airlines' point of view, SSTs can increase the number of flights within a certain period of time as compared to conventional transonic jets, especially in long-distance flights. Thus, an increase of sales volume per unit of time is to be expected, assuming the running cost of SSTs is sufficiently low. Two important aerodynamic requirements must be satisfied in order to develop the next generation SST: fuel efficiency and regulation of the amount of noise generated during cruising, also known as "sonic boom" [3, 4]. To overcome these issues, drastic reductions in aerodynamic drag and sonic boom are required.

According to one estimate [5], the demand for smaller SSTs increases due to a relationship between development cost and customer demand. Smaller SSTs can reduce the amount of noise generated by sonic booms to a greater extent than large SSTs can, for example the Concorde. This is because of the Mach cut-off effect [6, 7]. For this reason, several ventures in the United States have been formed to develop a supersonic business jet (SSBJ). Aerion Corporation started development of an SSBJ carrying eight to 12 passengers, called "*Aerion AS2*" in 2014 (Figure 1-1). This project is supported by Airbus, Lockheed Martin and Boeing (the original project, called "*Aerion SBJ*", was started in 2004) [8,9]. Aerion AS2 aims for speeds of Mach 1.6, with a

Chapter 1

supersonic natural laminar flow wing, for a minimum projected range of 4,750 nm (or 8,800 km), with targets to achieve FAA certification in 2021 and to enter service in 2025. Likewise, Boom Technology is designing a 55 to 75 passenger SST, with a range of 4,500 nm (or 8,300 km) at Mach 2.2, to be introduced in the mid-2020s, called “*Overture*” (Figure 1-2). Japan Airlines and Virgin Group have invested tens of millions of dollars in total; 30 aircraft in all have been preordered. Boom Technology anticipates that a one third scale demonstrator, called “*Boom XB-1 Baby Boom*” (Figure 1-2), will be flight tested in 2020.

In Japan, several studies establishing the essential technologies for the realization of SST have been performed within the government, industry and academic communities. Japan Aerospace Exploration Agency (JAXA) recently conducted two large flight experiments. The first, called national experimental supersonic transport-1 (NEXST-1), involved a small-scale SST experimental model. It featured a natural laminar flow wing, optimized by the inverse design [10] and a fuselage designed using area rule [11] to minimize the wave drag. The flight testing was done at Woomera experimental yard in Australia in 2002 and 2005 [12]; a reduction in aerodynamic drag by as much as approximately 13%, was achieved beyond that of the Concorde. The Drop test for Simplified Evaluation of Non-symmetrically Distributed sonic boom (D-SEND) project [13,14] was conducted at the Esrange Space Center in Sweden in 2011 and 2015 to demonstrate and evaluate the design concept in terms of its ability to reduce the impact of sonic booms. The D-SEND project had two phases, D-SEND#1 and D-SEND#2. In each phase, sonic booms were measured using an aerial boom measurement system with microphone systems installed along the line of a tethered blimp. In D-SEND#1, two different axisymmetric bodies were dropped. In these tests, distinct sonic boom signatures arising from the differently shaped test bodies were captured as intended. D-SEND#2 used an experimental supersonic airplane, unmanned without an engine, based on JAXA's low sonic boom design technology. The flight

tests of the experimental supersonic airplane were successfully conducted; JAXA's low boom design concepts were validated in the flight test while considering the effects of atmospheric turbulence.

The basis of modern aerodynamic designs for SST is the sweep theory proposed [15, 16] in the 1960s using the liner theory [17]. It suggests that the wing that has the larger backward-swept angle can reduce wave drag in transonic and supersonic cruises. In addition, recent studies [18, 19 and 20] by computational fluid dynamics (CFD) suggest that the lower backward-swept wing can also reduce the wave drag for the wing which has the supersonic leading edge. Thus, SST wing designs utilize a wing with a large backward-swept angle and small taper ratio in order to reduce wave drag at sonic speeds; several studies regarding wings with large backward-swept angle [21, 22 and 23] were carried out. Forward-swept wing design is also an effective method to reduce wave drag due to the same reason as backward-swept wing design; however, forward-swept wing design has not been focused on because of a risk of structural disorder due to aeroelastic divergence [24]. Although, given the development of composite material and an aeroelastic tailoring technology [25], the use of a forward-swept wing design is getting closer to reality. A study by Horinouchi [26] suggests that the forward-swept wing design can be expected to achieve simultaneous reduction of drag and sonic boom.

Additional perspectives are also required regarding sonic boom reduction and improvement of low speed aerodynamic performance for supersonic wings. An SST designer needs to design a wing by choosing a wing planform that satisfies mission requirements by utilizing knowledge concerning the relationship between a supersonic wing's planform and the simultaneous reduction of aerodynamic drag and sonic booms generated during cruising. Few studies delving into this relationship have been performed, however.



Figure 1-1 Aerion AS2.



Figure 1-2 Overture (near side) and XB-1 (far side), developed by Boom Technology.

1.2 Reviews of Optimization Techniques

Optimizations for engineering designs refers to finding the best feasible solution that satisfies all design criteria. In other words, a maximization or minimization problem for objective functions is solved under defined constrains. Optimization techniques can broadly be divided into gradient-based methods (GMs) [27] and evolutionary algorithms (EAs) [28]. The GM is traditional, and it uses function gradients, for example, the Newton method [29] or sequential quadratic programming (SQP) [30]; optimum search is performed for the direction that has the maximum gradient. While GMs are simple and popular algorithms, the function gradient cannot be easily defined for real-world problems when using GMs, and they have difficulties in attaining the global optimum. In contrast, EAs are a part of evolutionary computation [31] and are inspired by biological evolution. They can be divided based on four major methodologies: genetic algorithms (GAs) [32], genetic programming (GP) [33], evolutionary strategy (ES) [34], and evolutionary programming [31]. Among these, the GA is the most extensively used algorithm. In a GA, function gradients are not required for optimization, and the evaluation values of several candidates are required. In addition, the multi-point simultaneous search of GAs is capable of suppressing local convergence and obtaining an exact or approximate global optimum solution even when a multimodal problem is solved.

Owing to advancements in numerical simulation technologies (e.g., CFD) and optimization techniques (e.g., EAs), design methods that combine CFD with GAs have been applied to transport vehicles such as aircraft [35, 36], high speed trains [37] and automobiles [38]; the effectiveness of these methods (i.e., a more efficient design process than conventional methods utilizing experimentation and manual design) and the results of these innovative designs have been confirmed.

However, a number of candidates have to be evaluated in a GA to obtain the global optimum.

Furthermore, if the evaluation process using numerical simulation is time consuming, the time required to finish the optimization becomes prohibitively expensive. Jones, et al [39] proposed efficient global optimization (EGO), which was introduced by the Kriging surrogate model [40, 41]. In this method, the evaluation value of several candidates is transferred from a surrogate model that has been constructed using the information of the already known samples. Additional samples obtained from the optimal search are evaluated without the surrogate model; the surrogate model is then updated with the information of the additional sample. EGO was applied to several aircraft designs [42, 43] and optimal solutions were obtained in each research investigation.

Even if a surrogate model was used to evaluate an objective function using an optimization method such as EGO, further efficiency improvement of the optimization method is expected when the evaluation of a candidate is time consuming. The multi-fidelity approach [44, 45, and 46] is a candidate solution. In this approach, a low-fidelity evaluation, which takes lesser time and has a rougher accuracy than high-fidelity evaluation, is used together with a high-fidelity evaluation. Choi, et al [44] proposed a method wherein the fidelity of evaluation was enhanced sequentially. In a study by Rajnarayan, et al [45], an effective method was proposed that consisted of a differential model comprising a high-fidelity surrogate model and a low-fidelity surrogate model; the low-fidelity surrogate model was upgraded using the differential model. In contrast, in a study by Kanazaki et al [46], the high-fidelity surrogate model was upgraded using the differential model. This method was applied to a low-boom SST wing design problem; thus, a higher reduction of the computational cost was achieved compared to single fidelity EGO while the equivalent design knowledge could be obtained. However, the merits of parallel computational environments such as super computers are not utilized in these three multi-fidelity approaches because only one additional sample is obtained and evaluated to upgrade the surrogate model per optimization loop. To solve the multi-objective optimization problem for SST design, time-

consuming simultaneous evaluations of the impacts of aerodynamic drag and sonic booms are required. Therefore, a more efficient design method utilizing the merit of parallel computational environment is required.

1.3 Objective of this study

This study aims to design an optimal airfoil distribution for supersonic wing planforms by developing a multi-fidelity optimum design method that is more efficient than conventional methods, with the broader aim of contributing to the realization of innovative civil SST. The definitive purpose of this research is to obtain design knowledge regarding the relationship between supersonic wing planforms and optimal airfoil distribution to reduce aerodynamic drag and noise, which are caused by sonic booms generated at supersonic cruising speeds; this can be accomplished using the proposed design method, which integrates multi-fidelity approaches with the concept of multi-additional sampling.

Reference

- [1] Boeing, “Commercial Market Outlook 2019 – 2038”, 2019.
- [2] Airbus, “Global Market Forecast Cities, Airports & Aircraft 2019-2038”, 2019.
- [3] May, M., “Crackin' Good Mathematics”, *American Scientist*, Vol. 90, No.5, 2002, pp.415-416.
<http://www.jstor.org/stable/27857718>
- [4] Khasdeo, N., “Sonic Boom: Focusing and Mitigation: Focusing with Conservative Method and Mitigation with Shape Optimization”, *VDM Verlag*, 2009.
- [5] Liebhardt. B., Gollnick. V. and Luetjens. K., “Estimation of the Market Potential for Supersonic Airliners via Analysis of the Global Premium Ticket Market”, AIAA paper 2011-6806, September 2011. <https://doi.org/10.2514/6.2011-6806>
- [6] Yamashita. R and Suzuki. K., “Lateral Cutoff Analysis of Sonic boom Using Full-Field Simulation”, *Aerospace Science and Technology*, Vol. 88, 2019, pp.316-328.
<https://doi.org/10.1016/j.ast.2019.03.020>
- [7] Cliatt, L., Hill, M. and Haering, E., “Mach Cutoff Analysis and Results from NASA's Farfield Investigation of No-boom Thresholds”, AIAA Paper 2016-3011, 2016.
<https://doi.org/10.2514/6.2016-3011>
- [8] Garzon, A. and Matisheck, J., “Supersonic Testing of Natural Laminar Flow on Sharp Leading Edge Airfoils. Recent Experiments by Aerion Corporation”, AIAA paper 2012-3258, September 2012. <https://doi.org/10.2514/6.2012-3258>
- [9] Matisheck, J., “The Aerion AS2 and Mach Cut-Off”, *The Journal of the Acoustical Society of America*, Vol. 141, Issue 5, 2017, pp.3564-3564.
- [10] Jeong, S., Matsushima, K., Iwamiya, T., Obayashi, S. and Nakahashi, K., “Inverse Design Method for Wing of Supersonic Transport” AIAA Paper 98-0602, 1998.
<https://doi.org/10.2514/6.1998-602>
- [11] Jones, R., “Theory of Wing-body Drag at Supersonic Speeds”, NACA-TR-1284, January 1956.
- [12] Yoshida, K., “Supersonic Drag Reduction Technology in The Scaled Supersonic Experimental Airplane Project by JAXA”, *Progress in Aerospace Sciences*, Vol. 34, 2009, pp.124-146. <https://doi.org/10.1016/j.paerosci.2009.05.002>
- [13] Honda, M. and Yoshida, K., “D-SEND Project for Low Sonic boom Design Technology”, 28th Congress of the International Council of the Aeronautical Sciences, ICAS2012-1.2.1, September 2012.
- [14] Yoshida, K. and Honda, M., “D-SEND#2 – Flight Tests for Low Sonic boom Technology”,

- 30th Congress of the International Council of the Aeronautical Sciences, ICAS2016-1.6.3, September 2016.
- [15] Busemann, A., “Aerodynamic Lift at Supersonic Speeds”, Volta conference, Luftfahrtforschung, Ed.12, No.6, 1935, pp.210-220
- [16] Robert, J. and Cohen, D., “High Speed Wing Theory”, *Princeton University Press*, 1960.
- [17] Rathakrishnan, E., “Theoretical Aerodynamics”, *Wiley*, 2013.
- [18] Kishi, Y., “Panform Dependency of Multi-point Aerodynamic Performance for Supersonic Wing”, JSASS Paper 2013-5017, November 2013, (in Japanese).
- [19] Kashitani, M., Kusunose, K., Yamaguchi, Y. and Nakao, S., “A Preliminary Study on the Effects of Sweepback Angle in Supersonic Flow”, JSASS Paper 2014-5073, October 2014, (in Japanese).
- [20] Takeuchi, K., Matsushima, K., Kanazaki, M. and Kusunose, K., “CFD Analysis on Sweep Angles of The Leading Edge and Trailing Edges of Wing in Supersonic Flow”, Transactions of The JSME (In Japanese), Vol. 81, No.827, 2015, pp.15-37. <https://doi.org/10.1299/transjsme.15-00037>
- [21] Lei, Z., Makino, Y. and Yoshida, K., “Warp Design of a Supersonic Wing Using a Nonlinear Optimization Method”, AIAA Paper 2004-216, 2004. <https://doi.org/10.2514/6.2004-216>
- [22] Sol, M., and Vos, R., “Conceptual Design of Swept-Wing Root Airfoil”, AIAA Paper 2016-3285, 2016. <https://doi.org/10.2514/6.2016-3285>
- [23] Sundaram, S., Viswanath, P. and Subaschandar, N., “Viscous Drag Reduction Using Riblets on a Swept Wing”, AIAA Journal, Vol. 37, No.7, 1999, pp. 851-856. <https://doi.org/10.2514/2.7533>
- [24] Raymer, D., “Aircraft Design: A Conceptual Approach Fourth Edition”, Amer Inst of Aeronautics, 2006.
- [25] Shirk, M., Hertz, T. and Weisshaar, T., “Aeroelastic tailoring - Theory, practice, and promise”, *Journal of Aircraft*, Vol. 23, No.1, 1986, pp.6-18. <https://doi.org/10.2514/3.45260>
- [26] Horinouchi, S., “Conceptual Design of A Low Sonic boom SSBJ”, JAXA Research and Development Report, JAXA-RR-05-045, 2007, (in Japanese).
- [27] Polak, E., “Optimization: Algorithms and Consistent Approximations”, Springer, 1997.
- [28] Spears, W., “Evolutionary Algorithms: The Role of Mutation and Recombination”, *Springer Berlin Heidelberg*, 2010.
- [29] Süli, E. and Mayers, D., “An Introduction to Numerical Analysis”, *Cambridge University Press*, 2003.
- [30] Nocedal, J. and Wright, S., “Numerical Optimization”, *Springer*, 2006.

- [31] Eiben, A. and Smith, J., “Introduction to Evolutionary Computing”, *Springer*, 2003.
- [32] Kramer, O., “Genetic Algorithm Essentials”, *Springer*, 2018.
- [33] Turing, A., “Computing Machinery and Intelligence”, *Mind*, Vol.49, pp.433-460, 1950.
- [34] Beyer, H. and Schwefel, H., “Evolution strategies – A comprehensive introduction”, *Natural Computing*, Vol.1, Issue 1, pp.3-52, 2002. <https://doi.org/10.1023/A:1015059928466>
- [35] Ban, N., Yamazaki, W. and Kusunose, K., “Low-Boom/Low-Drag Design Optimization of Innovative Supersonic Transport Configuration”, *Journal of Aircraft*, Vol. 55, No.3, 2018, pp. 1071-1081. <https://doi.org/10.2514/1.C034171>
- [36] Kanazaki, M., Utsuki, M., Sato, T. and Matsushima, K., “Airfoil Design for Martin Airplane Considering Using Global Optimization Methodology”, *International Journal of Aerospace System Engineering*, Vol.2, No.2, pp.29-33, 2015. <http://ijase.sase.or.kr/MN/>
- [37] Suzuki, M. and Nakade, K., “Multi-Objective Design Optimization of High-Speed Train Nose”, *Journal of Mechanical Systems for Transportation and Logistics*, Vol.6, No.1, 2013, pp.54-64. <http://doi.org/10.1299/jmtl.6.54>
- [38] Kanazaki, M., Obayashi, S. and Nakahashi, K., “Exhaust Manifold Design with Tapered Pipes Using Divided Range MOGA”, *The report of the Institute of Fluid Science*, Vol.15, 2003.
- [39] Jones, D. R., Schonlau, M., and Welch, W. J., “Efficient Global Optimization of Expensive Black-Box Function”, *Journal of Global Optimization*, Vol.13, Issue 4, 1998, pp.455-492. <http://doi.org/10.1023/A:1008306431147>
- [40] Sacks, J., Welch, W.J., Mitchell, T. J., and Wynn, H. P., “Design and Analysis of Computer Experiments”, *Statistical Science*, Vol.4, No.4, 1989, pp.409-435. <http://doi.org/10.1214/ss/1177012415>
- [41] David, M., “Handbook of Applied Advanced Geostatistical Ore Reserve Estimation”, *Elsevier Scientific Publishing*, 1988.
- [42] Kanazaki, M., Jeong, S. and Yamamoto, K., “High-Lift System Optimization Based on Kriging Model Using High Fidelity Flow Solver”, *Transactions of The Japan Society for Aeronautical and Space Sciences*, Vol.49, Issue 165, 2006, pp.169-174. <https://doi.org/10.2322/tjsass.49.169>
- [43] Kanazaki, M. and Seto, N., “Efficient Global Optimization Applied to Design and Knowledge Discovery of Supersonic Wing”, *Journal of Computational Science and Technology*, Vol. 6, No.1, 2012, pp.1-15. <https://doi.org/10.1299/jcst.6.1>
- [44] Choi, S., Alonso, J., Kroo, I. and Wintzer, M., “Multi-Fidelity Design Optimization of Low-Boom Supersonic Business Jet”, *Journal of Aircraft*, Vol.45, No.1, 2008, pp.106-118.

<https://doi.org/10.2514/1.28948>

- [45] Rajnarayan, D., Haas, A. and Kroo, I., “A Multifidelity Gradient-Free Optimization Method and Application to Aerodynamic Design”, AIAA Paper 2008-6020, September 2008.
<https://doi.org/10.2514/6.2008-6020>
- [46] Kanazaki, M., Takagi, H., and Makino, Y., “Mixed-Fidelity Efficient Global Optimization Applied to Design of Supersonic Wing”, *Procedia Engineering*, Vol.67, 2013, pp.85-99.
<https://doi.org/10.1016/j.proeng.2013.12.008>

Chapter 2 Planform Dependency Investigation of Low-Drag Airfoil at Supersonic and Transonic speeds

2.1 Introduction

Several studies [1,2 and 3] by a CFD suggests SST designers can choose not only a high backward-swept planform but also a low backward-swept planform depending the mission and the flight profile of the designed SST. However, researchers have mainly focused on high backward-swept wings such as swept wings, delta wings, and cranked arrow wings, and only a few studies have examined a wing with small backward-swept angle. In addition, the CFD results also suggest that different optimal airfoils should be used depending on the planform because the trends of aerodynamic performance differ according to the planform. The several researches have been carried out regarding supersonic wing design [4,5]. In a study by Matsushima, et al [4], two supersonic wing design problems for the Japanese scaled experimental Supersonic Transport (SST) models, known as National experimental supersonic transport-1 (NEXST-1), equipped with high backward-swept angle leading edges were discussed. The inverse design technique was applied with a Navier-Stokes simulation for both a clean configuration that did not consider the influence of the propulsion systems and for a configuration that considered two engine nacelles, demonstrating that the design using the simple inverse problem was effective for three-dimensional geometry. In a study by Sasaki, et al [5], an evolutionary algorithm (EA) was employed to optimize both the wing planform and airfoil distributions with a Navier-Stokes simulation to meet three objectives: minimizing the drag at supersonic cruise, minimizing the drag at transonic cruise and minimizing the bending moment at the wing root at supersonic cruise. A four-objective design optimization, in which pitching moment minimization was added as an objective function, was then conducted based on the results of the previous optimization. All four

objective functions of the two “arrow wing” type solutions were found to be superior to those in the pre-optimized design. These studies could find optimum results for a planform. However, the influence by the difference of the planform was not investigated. Thus, it is necessary to obtain design knowledge regarding the differences in the aerodynamic performance of high and low backward-swept wings for the optimal airfoil for a given planform.

In this chapter, to discuss the design knowledge, a wing design problem was solved by the efficient global optimization (EGO) [6] for a multi-objective problem (MoPs) to acquire the knowledge regarding planform dependency in supersonic wing design. In this study, two planforms are compared: a cranked arrow wing with a high backward-swept leading edge and a single-tapered wing with a low backward-swept leading edge. This preliminary study focused on only drag reduction before considering simultaneous reduction of sonic boom. Design problem is formulated as the minimization of drag in transonic and supersonic simultaneously, because transonic cruise may also account for a large percentage of the whole flight of a SST.

2.2 Design Method

2.2.1 Overview of Efficient Global Optimization

In general, the objective function must be evaluated considering a large number of samples to obtain an optimum solution. If each sample is evaluated via numerical simulation based on the physical model, the gross calculation time is excessively large. Thus, surrogate models are often used in the optimization process. Figure 2-1 presents a flow chart of EGO [6] which is a design method combined with evolutionary computation and Kriging surrogate model [7]. EGO is capable to search an optimal solution efficiently in global design space. The difference between EGO in a previous research [6] and in this research is in the manner in which the expected improvement (EI) is maximized. In the study by Jones, et al [6], the branch-and-bound algorithm

was used, while in this study, the divided range multi-objective genetic algorithm (DRMOGA) [8] was used.

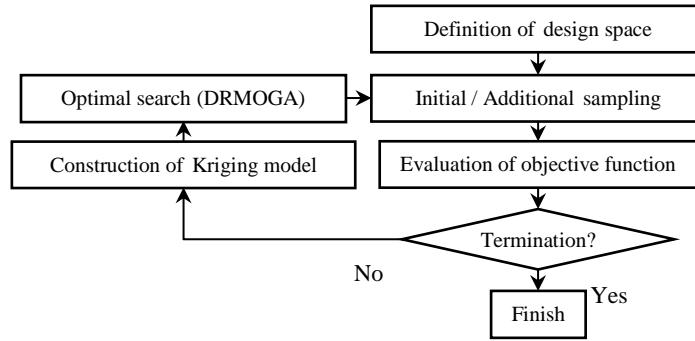


Figure 2-1 Flow chart of EGO.

2.2.2 Latin Hypercube Sampling for Initial Samples

Initial samples were obtained by Latin hypercube sampling (LHS) [9], which is multi-dimensionally developed from Latin square sampling and a typical the design of experiment (DoE) method. It allowed for the uniform extraction of sample points from the design space.

The number of initial samples N_{initial} is decided as following equation [10]:

$$N_{\text{initial}} = \frac{(m + 1)(m + 2)}{2} \times F_M \quad (F_M = 1.5 \sim 2.0) \quad (2-1)$$

where m and F_M presents the number of design variables and margin factor, respectively. This equation is based on the number of terms of m -dimensional quadric surface. Considering multimodality solution space, N_{initial} was calculated to multiply the number of terms of m -dimensional quadric surface by the margin factor.

2.2.3 Kriging Surrogate Model

A surrogate model was used to reduce the evaluation cost during the optimal search process. In general, the use of an EA is more advantageous as it ensures the diversity of global solutions. However, the computational cost of an EA is high. Therefore, a surrogate model, constructed using sample designs, was introduced to evaluate the unknown points more efficiently.

A Kriging surrogate model [7] is typically constructed to evaluate the spatial phenomena as a continuous random field. This enables the estimation of the value of an arbitrary point within a random field from observed data. The Kriging surrogate model can also estimate the error range between the true value and the value determined by the Kriging surrogate model at each point. However, when the solution space is complex, it is necessary for the Kriging surrogate model to calculate accurate local deviations in order to ensure high accuracy of the surrogate model, because the global model μ is constant (Figure 2-2). The Kriging surrogate model represents the value $\hat{y}_{\text{kriging}}(\mathbf{x}_{\text{dv}})$ at the unknown design point \mathbf{x}_{dv} as:

$$\hat{y}_{\text{kriging}}(\mathbf{x}_{\text{dv}}) = \mu + \varepsilon(\mathbf{x}_{\text{dv}}) \quad (2-2)$$

where μ denotes the constant global model and $\varepsilon(\mathbf{x}_{\text{dv}})$ represents the local deviation from the global model. The local deviation is expressed as:

$$\varepsilon(\mathbf{x}_{\text{dv}}) = \mathbf{r}(\mathbf{x}_{\text{dv}})^T \mathbf{R}^{-1}(\mathbf{f} - \mathbf{1}\mu) \quad (2-3)$$

where $\mathbf{r}(\mathbf{x}_{\text{dv}})$ is a vector that is expressed in terms of \mathbf{x}_{dv} . $\mathbf{r}(\mathbf{x}_{\text{dv}})$ is assigned the sample points, \mathbf{R} is a matrix that denotes the correlation between the sample points, and \mathbf{f} is a vector that contains the evaluation value of each sample point. The correlation between $\varepsilon(\mathbf{x}_{\text{dv}})$ and

$\varepsilon(\mathbf{x}_{\mathbf{dv}}^i)$ is related to the distance between the corresponding points, $\mathbf{x}_{\mathbf{dv}}$ and $\mathbf{x}_{\mathbf{dv}}^i$. In the Kriging surrogate model, the local deviation at an unknown point $\mathbf{x}_{\mathbf{dv}}$ is expressed through stochastic processes. A number of design points are calculated as sample points and then interpolated using a Gaussian random function as the correlation function for the estimation of the trend through the stochastic process.

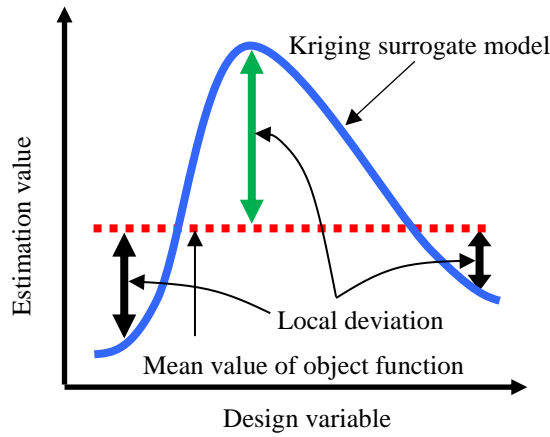


Figure 2-2 Concept of Kriging surrogate model.

2.2.4 Expected Improvement (EI)

To consider uncertainty at the predicted point in the Kriging surrogate model, the EI value [6] is used as an index for selecting additional samples. The EI value indicates the uncertainty of the accuracy of the surrogate model and optimality and calculated using each object function. The EI values for maximization problem are calculated as;

$$EI(\mathbf{x}_{\mathbf{dv}}) = \{\hat{y}(\mathbf{x}_{\mathbf{dv}}) - f_{max}\} \Phi\left(\frac{\hat{y}(\mathbf{x}_{\mathbf{dv}}) - f_{max}}{\hat{s}(\mathbf{x}_{\mathbf{dv}})}\right) + \hat{s}(\mathbf{x}_{\mathbf{dv}}) \phi\left(\frac{\hat{y}(\mathbf{x}_{\mathbf{dv}}) - f_{max}}{\hat{s}(\mathbf{x}_{\mathbf{dv}})}\right) \quad (2-4)$$

and the EI values for the minimization problem as;

$$EI(\mathbf{x}_{dv}) = \{f_{min} - \hat{y}(\mathbf{x}_{dv})\} \Phi \left(\frac{f_{min} - \hat{y}(\mathbf{x}_{dv})}{\hat{s}(\mathbf{x}_{dv})} \right) + \hat{s}(\mathbf{x}_{dv}) \phi \left(\frac{f_{min} - \hat{y}(\mathbf{x}_{dv})}{\hat{s}(\mathbf{x}_{dv})} \right) \quad (2-5)$$

The points where $EI(\mathbf{x}_{dv})$ attains the maximum value for each objective function are selected as additional sample points. For example, if the number of object functions is two, at least two new sample points should be selected as additional sampling points. The robust exploration of the global optimum and the improvement of the accuracy of the surrogate model can be simultaneously achieved as Figure 2-3.

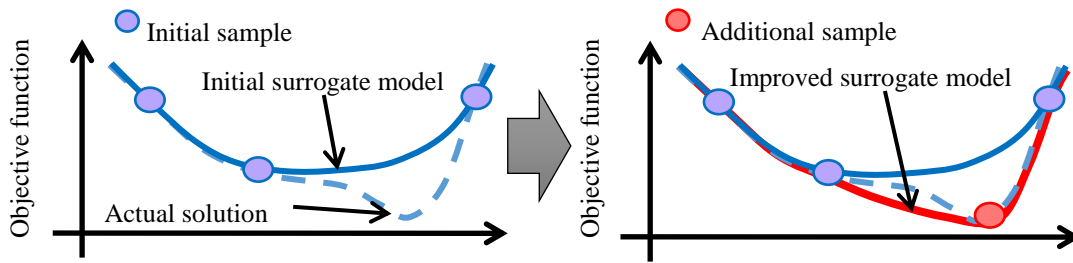


Figure 2-3 Improvement of the surrogate model.

2.2.5 Divided Range Multi-Objective Genetic Algorithm (DRMOGA)

To determine the optimum point, DRMOGA [8] was applied. In order to maintain the diversity of solutions, the population was divided into several sub-populations by the neighborhood cultivation scheme. Sub-populations were gathered at regular intervals. DRMOGA can improve the diversity of solutions in population because individuals evolve in each sub-population. In each sub-population, the fast non-dominated sorting genetic algorithm (NSGA-II) [11] was used for optimization. An elite strategy [12] and the roulette wheel method [12] were used in the selection process, a blended crossover (BLX)-0.5 [13] was used in the crossover process, and uniform mutation [12] with a mutation rate of 0.1 was used in the mutation process.

2.3 Analysis Method for Design Results

A functional analysis of variance (functional ANOVA) [14], which is a multi-variate analysis method, was used for the investigation for the relationship between the object function and the design variables. Applied to the ANOVA, the contribution of the design variables to the objective function can be calculated. In this study, the ANOVA was used to understand the influence that each design variable could have on the objective function. Using the results of ANOVA, designer can eliminate the design variables that do not considerably influence the objective function.

In order to evaluate the effect of each design variable, the total variance of the model was decomposed into the variance attributed to each design variable and the interactions between the design variables by integrating the variables of the surrogate model. The design variable x_i was normalized from zero to one and the variance of a design variable x_i (represented as $\mu_i(x_i)$) can be defined as

$$\mu_i(x_{dv_i}) = \int \cdots \int \hat{y}(x_{dv_1}, \cdots, x_{dv_i}, \cdots, x_{dv_m}) dx_{dv_1}, \cdots, dx_{dv_{i-1}}, dx_{dv_{i+1}}, \cdots, dx_{dv_m} - \mu \quad (2-6)$$

where μ is the total mean. In turn μ is calculated as:

$$\mu \equiv \int \cdots \int \hat{y}(x_{dv_1}, \cdots, x_{dv_i}, \cdots, x_{dv_m}) dx_{dv_1}, \cdots, dx_{dv_i}, \cdots, dx_{dv_m} \quad (2-7)$$

The ratio of the variance p_{variance_i} attributed to the design variable and the total variance of the surrogate model can be expressed as follows:

$$p_{dv_i} \equiv \frac{\int [\mu_i(x_{dv_i})]^2 dx_{dv_i}}{\int \cdots \int [\hat{y}(x_{dv_1}, \cdots, x_{dv_i}, \cdots, x_{dv_m}) - \mu]^2 dx_{dv_1}, \cdots, dx_{dv_i}, \cdots, dx_{dv_m}} \quad (2-8)$$

The value obtained using Eq. (2-8) represents the sensitivity of an objective function to the variance of the design variable x_{dvi} .

2.4 Aerodynamic Evaluation

The governing equation of the low-fidelity evaluation was the linearized compressible potential flow equation, which solves only for the surface of the objects.

$$(M_\infty^2 - 1) \frac{\partial^2 \varphi}{\partial x^2} - \frac{\partial^2 \varphi}{\partial y^2} - \frac{\partial^2 \varphi}{\partial z^2} = 0 \quad (1 < M_\infty) \quad (2-9)$$

$$(1 - M_\infty^2) \frac{\partial^2 \varphi}{\partial x^2} + \frac{\partial^2 \varphi}{\partial y^2} + \frac{\partial^2 \varphi}{\partial z^2} = 0 \quad (M_\infty < 1) \quad (2-10)$$

By dividing the object surface into panels, discretizing them, and adding two unknown quantities, Eq. (2-9) or (2-10) can be transformed into simultaneous linear equations. These equations are considered appropriate if the thickness of the object is negligible compared to its length, and if the flow velocity in the calculation space is considerably different from the speed of sound. A CAD-based Automatic Panel Analysis System (CAPAS) [15], developed by JAXA, was applied as the aerodynamic solver to evaluate the low-fidelity configuration in which the engine intake and the nacelle were not present.

2.5 Design Problems

2.5.1 Design Targets and Design Cases

In this study, wing design problems were solved for two cases—a cranked arrow wing (Case 1), which is the same as the concept model [16] proposed by JAXA, and a single-tapered wing (Case 2), which is similar to Aerion AS2's planform. The geometrical parameters of each planform are summarized in Table 2-1. To evaluate the aerodynamic performance, these calculation models comprising the wing, fuselage, and tail wing were considered.

Table 2-1 Dimensions of the planforms.

	Case 1	Case 2
Aspect ratio	2.5	3.4
Taper ratio of inboard	0.28	1.00
Taper ratio of outboard	0.37	0.31
Leading backward-swept angle of inboard	68°	20°
Leading backward-swept angle of outboard	52°	20°
Kink position	63% semi-span	
Wing area	175 m ²	

2.5.2 Design Space

The design space was defined for three sections, namely, root, kink and tip. The geometry between the root and kink were interpolated by a spline curve, and that between the kink and tip were linearly interpolated. The design variables and their ranges are summarized in Table 2-2. The base airfoil for Case 1 was the NACA 64A airfoil and that for Case 2 was a biconvex airfoil (see Figure 2-4).

Table 2-2 Design space.

			Lower bound	Upper bound
Thickness ratio	root	$dv1$	$0.03\%_c$	$0.06\%_c$
	kink	$dv2$	$0.03\%_c$	$0.05\%_c$
	tip	$dv3$	$0.02\%_c$	$0.05\%_c$
Forward camber position		$dv4$	$0.30\%_c$	$0.45\%_c$
Forward camber height	root	$dv5$	$0.02\%_c$	$0.05\%_c$
	kink	$dv6$	$-0.02\%_c$	$0.05\%_c$
	tip	$dv7$	$-0.02\%_c$	$0.04\%_c$
Aft camber position		$dv8$	$0.60\%_c$	$0.75\%_c$
Aft camber height	root	$dv9$	$-0.03\%_c$	$0.02\%_c$
	kink	$dv10$	$-0.02\%_c$	$0.02\%_c$
	tip	$dv11$	$-0.02\%_c$	$0.02\%_c$
Twisted angle	root	$dv12$	0.0°	2.0°
	kink	$dv13$	-2.0°	2.0°
	tip	$dv14$	-4.0°	0.0°

(%_c: The percentage of the chord length)

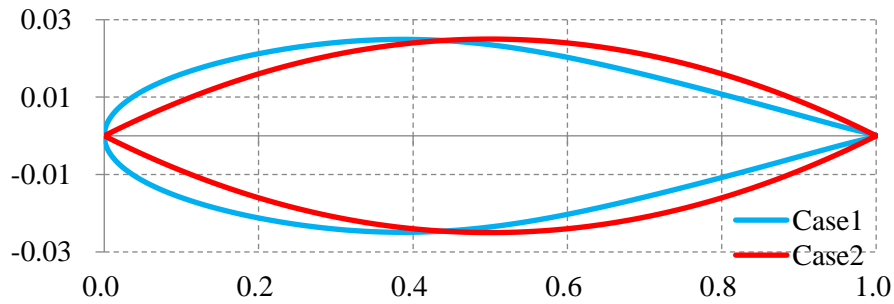


Figure 2-4 Base airfoils for each case.

2.5.3 Objective Functions and Constrains

The objective functions are expressed as follows;

$$\left\{ \begin{array}{l} \text{Minimize: } C_{DP} \text{ at } M_\infty = 1.6 \\ \text{Minimize: } C_{DP} \text{ at } M_\infty = 0.8 \end{array} \right.$$

$$\text{Subject to } L = W, X_{CP} = X_{CG}$$

Chapter 2

To improve the cruise efficiency of the SST, it is important to consider not only the supersonic condition, but also the transonic condition. The flying condition for the first objective was assumed as supersonic cruise at an altitude of 15,000 m, and that for the second objective was assumed as transonic cruise at an altitude of 11,000 m.

Through the aerodynamic evaluation, the pressure drag coefficient C_{DP} of the planforms at Mach 1.6 was determined under two constraints considered to ensure level flight. The first pertained to the weight of the aircraft (W) and lift (L), with change in the angle of attack (α) of the aircraft. To estimate the α for a level flight, at least two aerodynamic performance conditions for different α values were required because a first-order regression model was used to describe the relationship between the lift and the α of the aircraft. The required lift was calculated by statistically estimating the weight of wing [17,18,19 and 20] as

$$W_w = 5.63 \times 10^{-2} \times \left[\frac{W_{TO} \times n_{ult} \times b \times S_{wing}}{t_{root} \cos \Lambda} \right]^{0.501} \quad (2-11)$$

The weight of the aircraft in flight was estimated by adding W_w to the weight of the fuselage and the tail for JAXA's concept model [16]. The second constraint was used to match the location of the center of pressure (X_{CP}) to that of the center of the gravity (X_{CG}) to satisfy the trim stability condition for different horizontal tail wing angles, for each aerodynamic evaluation. Figure 2-5 denotes the relationship between the angle of the horizontal tail wing and the coordinate of the center of pressure. Yellow symbols were calculated with the method described in section 4.2. According to this figure, a first-order regression model can be defined between the angle of the horizontal tail wing and the coordinate of the center of pressure (X_{CP}). Thus, to estimate the trimmed angle of the horizontal tail wing, the first-order regression model was used in this study. When the AoA of the aircraft and the horizontal tail wing angle were calculated, the aerodynamic

evaluation was considered to correspond to level flight conditions. Calculations were performed 12 times for each sample to evaluate the aerodynamic performance under these constraints.

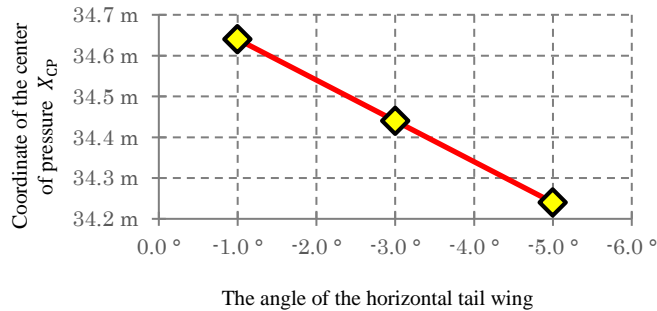


Figure 2-5 Relationship between the location of the center of pressure and the horizontal tail wing angle, determined by a first-order regression model.

2.6 Results and Discussion

2.6.1 Sampling Results

In this study, two additional samples were added in each additional sampling by DRMOGA. In DRMOGA, the total generation number is 64 and the size of population is 64. The population is divided into four sub-populations. Sub-populations are shuffled every four generations.

The aerodynamic performance of all initial and additional samples for both cases is shown in Figure 2-6. In this figure, each dot corresponds to each sample and the high direction of the optimality of samples is indicated by the arrow written “optimal direction”. In other word, low drag samples at the both Mach numbers are located in the lower left on Figure 2-6. Most of the additional samples in Case 1 exhibited better performances than the initial samples. On the other hands, in Case 2, several solutions could not be improved. This result suggests that Case 2 is more difficult to solve than Case 1.

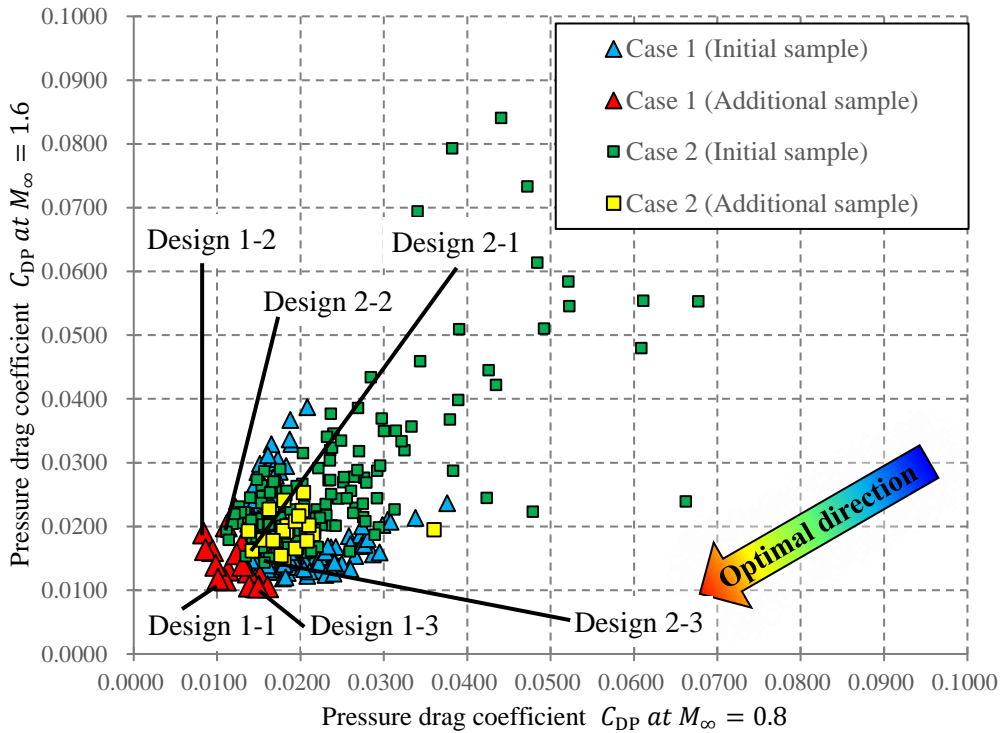


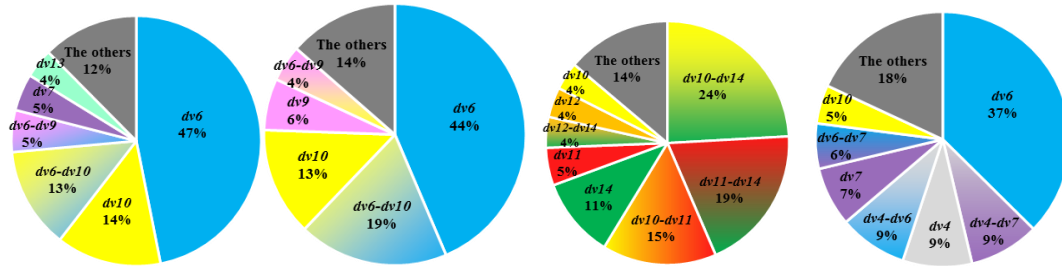
Figure 2-6 Sampling results.

2.6.2 Knowledge Discovery by Functional ANOVA

Visualization results of the design space and the solution space by the functional ANOVA are shown in Figure 2-7. In Case 1, the trend of C_{DP} at $M_\infty = 1.6$ is similar to that of C_{DP} at $M_\infty = 0.8$, because the wings in Case 1 have a subsonic leading edge for the both Mach numbers. The design variables for the camber shape at kink (such as $dv6$, $dv10$ and $dv4$ which were defined in Table 2-2) have a predominant effect at both Mach numbers because the kink geometry influences the inboard and the outboard.

On the other hand, the ANOVA results of Case 2 depend on the Mach number, because the speed of the freestream is different; a subsonic leading edge can be observed at $M_\infty = 0.80$ and a supersonic leading edge can be observed at $M_\infty = 1.6$. At $M_\infty = 0.8$, the design variables for the tip (such as $dv14$ and $dv11$) show the effect of the induced drag, while in Case 1, these design

variables for the tip show only small effects, because the chord length at the tip of Case 2 is longer than that of Case1.



(a) Case 1 ($M_\infty = 0.8$) (b) Case 1 ($M_\infty = 1.6$) (c) Case 2 ($M_\infty = 0.8$) (d) Case 2 ($M_\infty = 1.6$)

Figure 2-7 Functional ANOVA ($dv\sim$ means design variable defined in Table 2-2).

2.6.3 Design Examples

Designs 1-1, 1-2, 1-3, 2-1, 2-2, and 2-3 were selected from all samples as shown in Figure 2-6 to discuss and compare the trends of the optimal shape of each planform.

2.6.3.1 Comparison of Low-drag Solutions at Both Speeds between Selected Planforms

Designs 1-2 and 2-2 demonstrated the lowest drag at the transonic cruise condition in each planform case. Designs 1-3 and 2-3 achieved the lowest drag at the supersonic cruise condition in each planform case. The pressure distributions are compared in Figure 2-8. At each Mach number, the pressure at the leading edge of Design 2-1 was higher than that in Design 1-1. This was caused by the smaller backward-swept angle of Design 2-1 than that of Design 1-1. In the supersonic condition, Design 1-1 shows a suction peak at the upper surface of the wing, because a high backward-swept angle tends to inhibit the generation of shock waves [Figure 2-8 (a)(b)]. In contrast, in Design 2-1, a shock wave was observed at the leading edge owing to its low backward-swept angle [Figure 2-8(d)] in the supersonic condition. Thus, Design 2-1 could not obtain a lift at the leading edge; it is observed that a wide positive-pressure region on the lower

Chapter 2

surface of the aft can generate sufficient lift.

The airfoil geometry distributions of Designs 1-1 and 2-1 are shown in Figure 2-9. The slope of the leading edge was smaller in Design 2-1 than in Design 1-1, because the acceleration of the flow causes a shock wave, which indicates wave drag. For the tip airfoil, Design 1-1 has a positive camber, whereas Design 2-1 has a straight camber. The C_p distributions at the kinks in Designs 1-1 and 2-1 are shown in Figure 2-10. According to Figure 2-10 (a), the C_p distributions of Design 1-1 are similar to those of Design 2-1. This indicates that the lift was generated equally along the chord direction at the airfoil of the kink in both designs because a precipitous pressure fluctuation was not observed except for the leading edge in both solutions. On the contrary, Figure 2-10 (b) shows the difference in the C_p distributions of Designs 1-1 and 2-1. In Design 1-1, negative lift is developed near the leading edge, indicating pitch down moment. The C_p of Design 2-1 has the almost the same value at the upper and lower surfaces around the leading edge. This indicates that flow acceleration around the leading edge of Design 2-1 is suitable for reducing the wave drag.

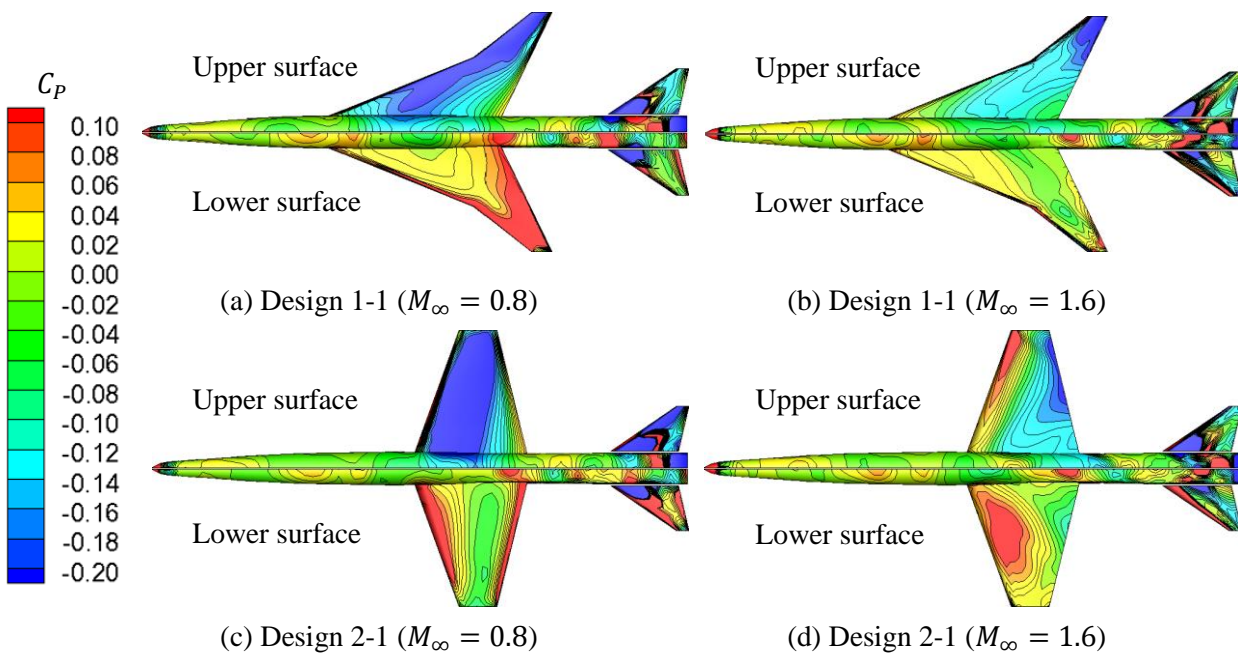


Figure 2-8 Surface C_p distributions for low-drag solutions in the both cruise conditions.

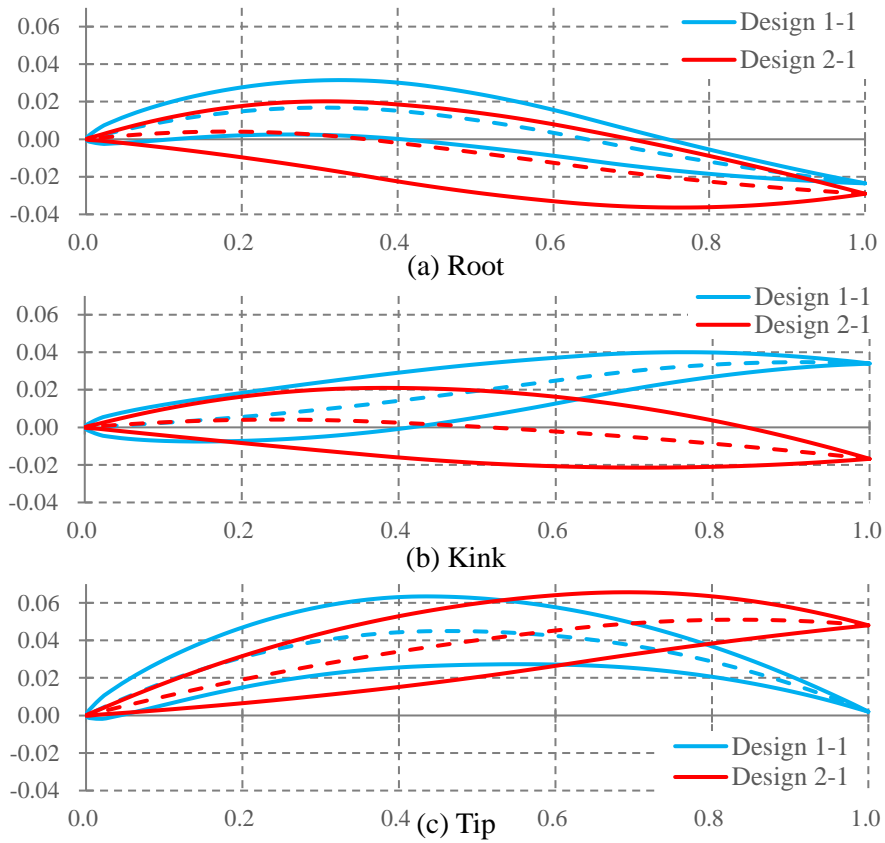
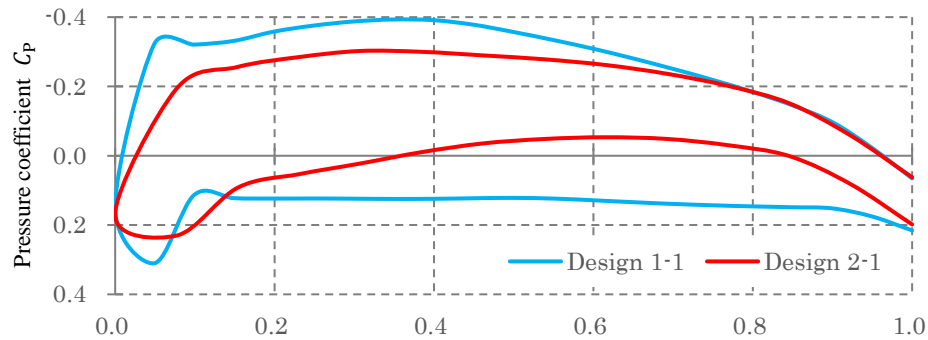
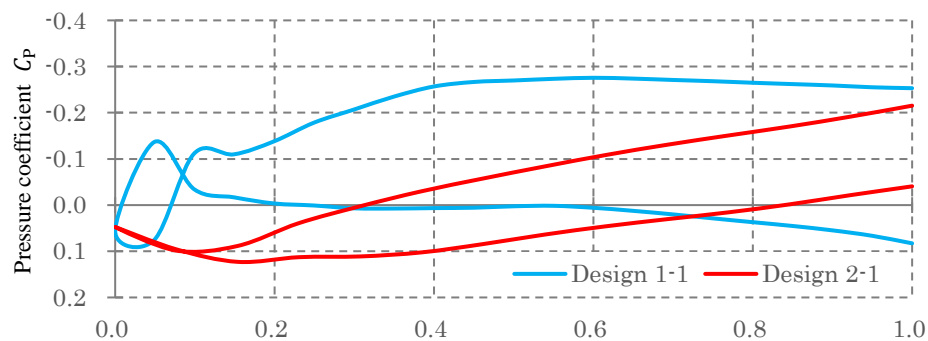


Figure 2-9 Cross sectional airfoils of representative solutions.



(a) $M_\infty = 0.8$



(b) $M_\infty = 1.6$

Figure 2-10 Cross sectional C_p distribution at the kink (63% semi-span).

2.6.3.2 Comparison of the Lowest-drag Solutions in Case 1 between Supersonic and Transonic Conditions

The surface C_p distributions and airfoil geometries of each cross section for Designs 1-2 and 1-3 are shown in Figure 2-11 and Figure 2-12, respectively. In the transonic condition ($M_\infty = 0.8$), Figure 2-11(a)(c) shows that the pressure of Design 1-2 is high (shown in red color) at the entire lower surface of the outboard wing; however, the high pressure region is at the leading edge on the lower surface of the outboard wing. Thus, the drag of Design 1-3 was larger than that of Design 1-2 on the lower surface of the outboard wing. Based on the airfoil geometries at these areas shown in Figure 2-12 (b)(c), the shape of the leading edge differed between Designs 1-2

and 1-3. This was due to the difference in the shape of the leading edge at the outboard wing between Designs 1-2 and 1-3. The cambers of the kink and tip of Design 1-2 are larger than those of Design 1-3. A large camber generates a pressure difference between the upper and lower surfaces. This resulted in the differences in flowfield and drag.

In the supersonic cruise condition ($M_\infty = 1.6$), the difference of the pressure distributions of Designs 1-2 and 1-3 at the leading edge can be observed in Figure 2-11(b)(d). Design 1-2 had a stronger shock wave at the leading edge than Design 1-3 because of larger camber at the kink and tip airfoils. This contributed to the difference in the drags of Designs 1-2 and 1-3.

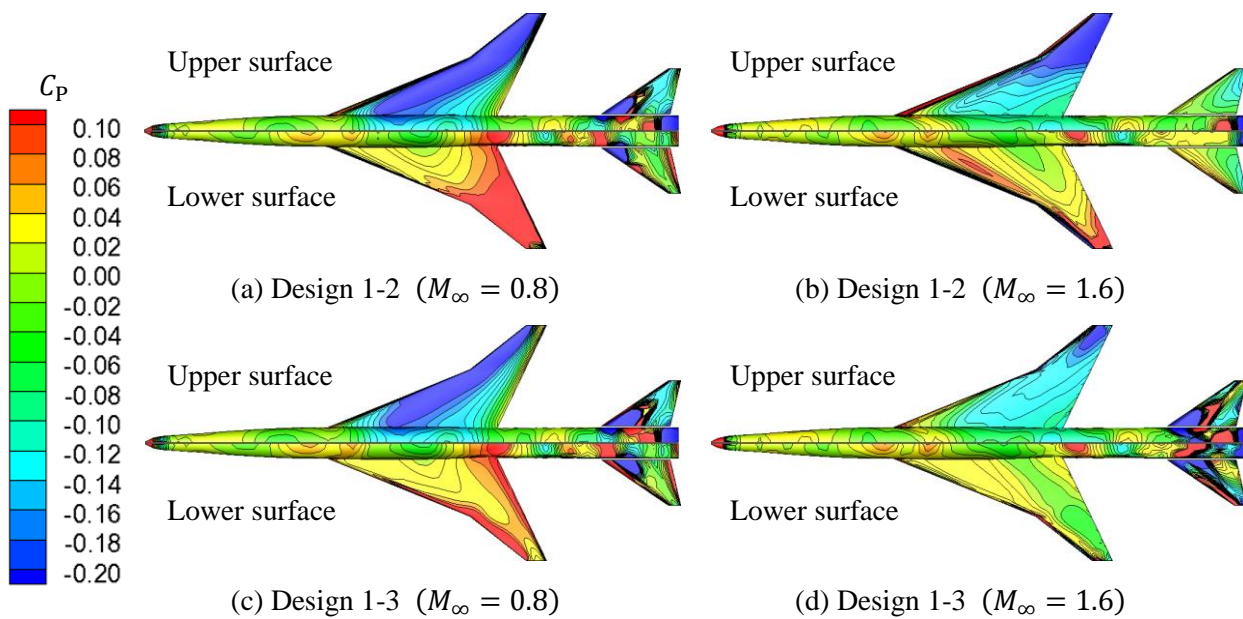
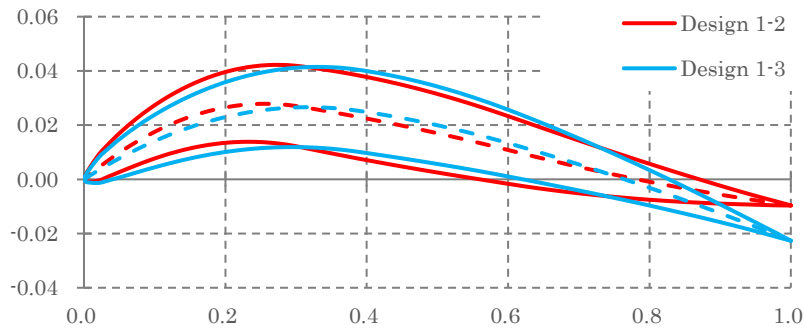
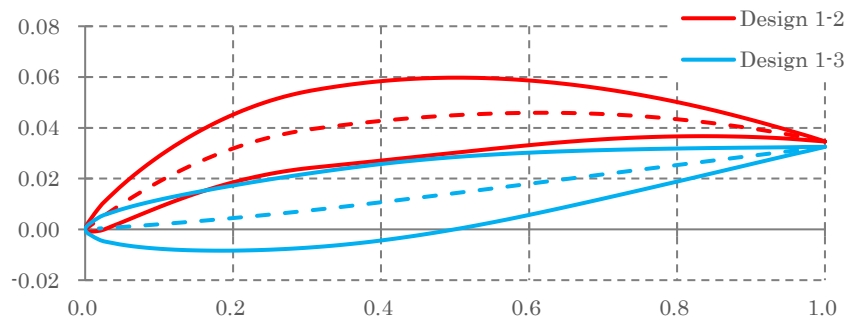


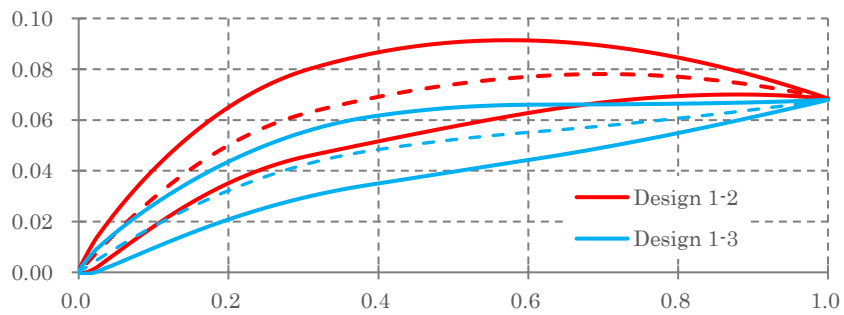
Figure 2-11 Surface C_p distributions for the lowest-drag solutions in the transonic cruise condition.



(a) Root



(b) Kink



(c) Tip

Figure 2-12 Airfoil geometries of each cross section for Designs 1-2 and 1-3.

2.6.3.3 Comparison of the Lowest-drag Solutions in Case 2 between Supersonic and Transonic Conditions

The surface C_p distributions and airfoil geometries of each cross section for Designs 2-2 and 2-3 are shown in Figure 2-13 and Figure 2-14, respectively. In the transonic condition ($M_\infty = 0.8$), remarkable difference in the surface C_p distribution of Designs 2-2 and 2-3 can be observed at the horizontal tail wing. The angle of attack of the horizontal tail wing of Designs 2-2 and 2-3 were 0.86° and 5.17° , respectively. Therefore the trim drag of Design 2-3 became larger than that of Design 2-2. According to Figure 2-14, the slope of the leading edge of Design 2-3 was smaller than that of Design 2-2. This affects the strength of the suction of the leading edge. The lift distributions of Designs 2-2 and 2-3 became different; thus the AoA of the horizontal tail wing differed.

In the supersonic cruise condition ($M_\infty = 1.6$), a difference in the pressure distributions of Designs 2-2 and 2-3 at the leading edge can be observed in Figure 2-13(b)(d). The high-pressure region (shown in red color) of Design 2-3 on the leading edge of the lower surface was narrower than that of Design 2-2. This pressure increase was caused by a shock wave at the leading edge. The shock wave of Design 2-3 was weaker than that of Design 2-2 because the slope of the leading edge of Design 2-3 was smaller than that of Design 2-2.

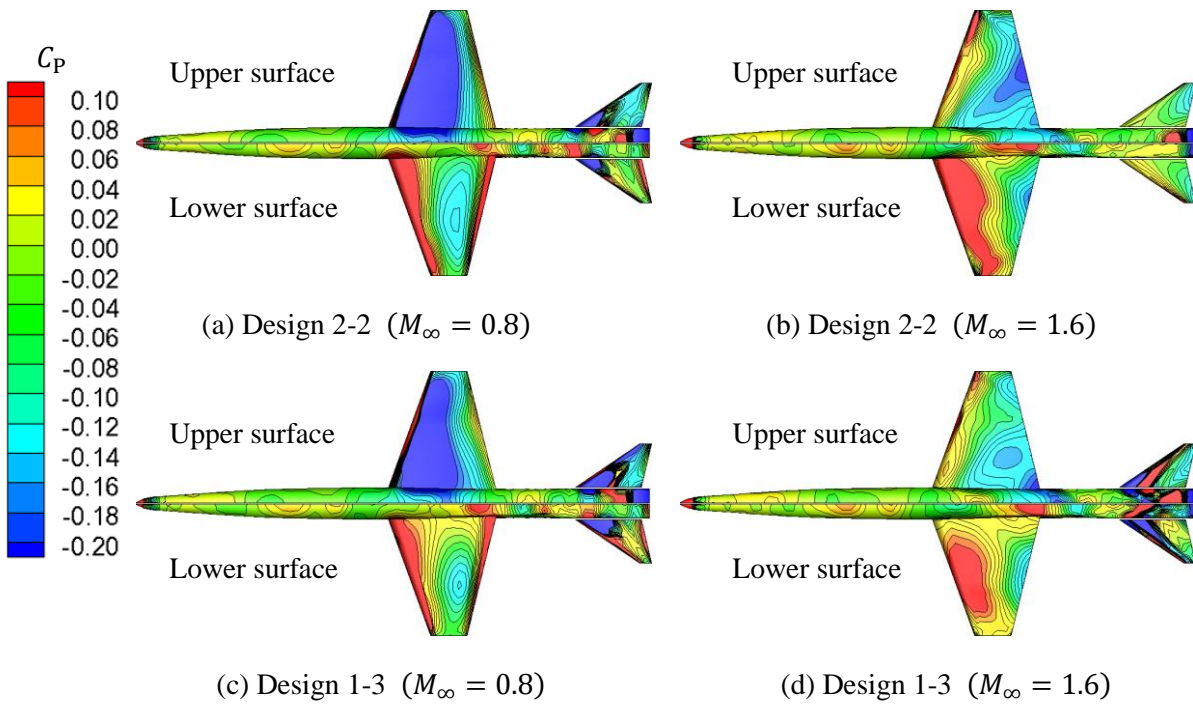
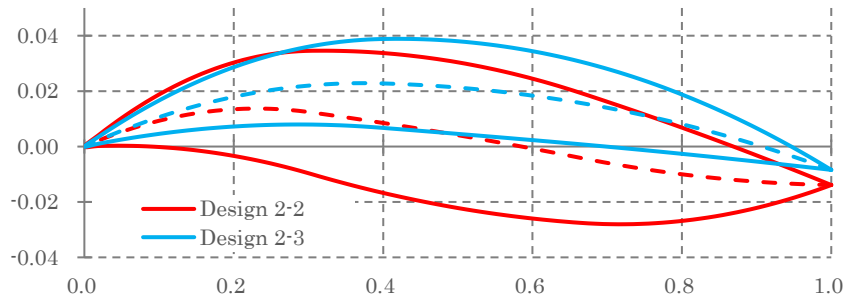
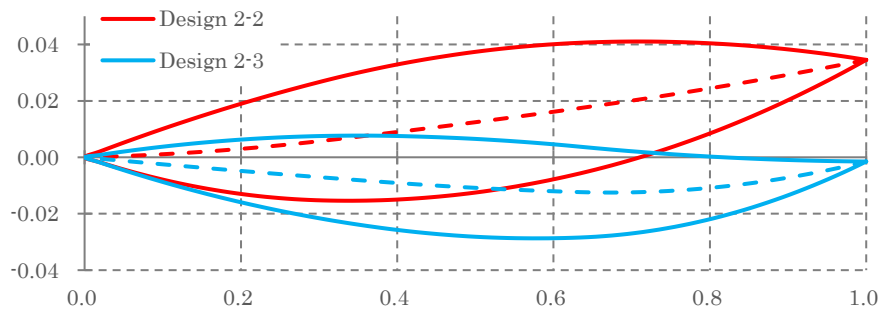


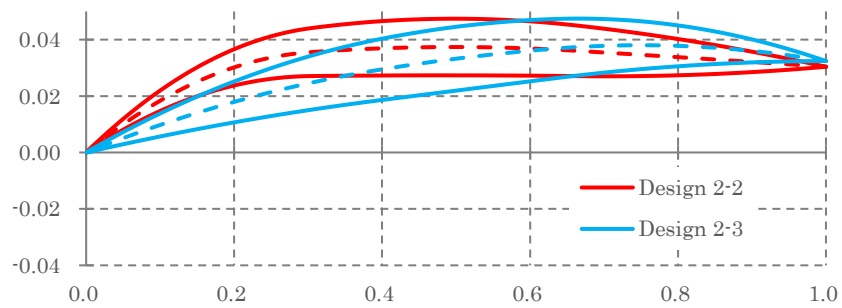
Figure 2-13 Surface C_p distributions for lowest-drag solutions in the supersonic cruise condition.



(a) Root



(b) Kink



(c) Tip

Figure 2-14 Airfoil geometries of each cross section for Designs 2-2 and 2-3.

2.7 Conclusion

To obtain the design knowledge of the planform dependency of airfoil design results, the aerodynamic designs of an airfoil for a cranked arrow wing and a single-tapered wing were studied using EGO. Each defined airfoil had different optimum geometries for the two wing planforms. For example, the slope of the leading edge is smaller in the case of the single-tapered wing than in the case of the cranked arrow wing to inhibit shock waves. In addition, the results of functional ANOVA show that the trends of contribution ratios of design variables to drag reduction differ with planforms. At supersonic speeds, the cranked arrow wing and the single-tapered wing are similar from the viewpoint of the dominant design variables; this is because the aim is to reduce wave drag, which defines the camber height of the kink airfoil. In contrast, at transonic speeds, the dominant design variables of the two wings are different. In the cranked arrow wing, the camber height of the kink airfoil is dominant at supersonic speeds. In the single-tapered wing, the design variables for the tip are dominant due to induced drag.

The comparison between the low-drag solutions at supersonic and transonic speeds showed that the slope of the leading edge of the single-tapered wing was smaller than that of the cranked arrow wing, because a shock wave can occur more easily in the single-tapered wing than in the cranked arrow wing. Comparing the lowest-drag solutions in the supersonic and transonic conditions, the low-drag solution in the supersonic condition tends to have a smaller camber than that in the transonic condition in both planforms. This affects the strength of the suction of the leading edge. The suction in the supersonic cruise condition should be weaker than that in the transonic cruise condition owing to the inhibition of generation of shock waves.

Reference

- [1] Kishi, Y., “Panform Dependency of Multi-point Aerodynamic Performance for Supersonic Wing”, JSASS Paper 2013-5017, November 2013, (in Japanese).
- [2] Kashitani, M., Kusunose, K., Yamaguchi, Y. and Nakao, S., “A Preliminary Study on the Effects of Sweepback Angle in Supersonic Flow”, JSASS Paper 2014-5073, October 2014, (in Japanese).
- [3] Takeuchi, K., Matsushima, K., Kanazaki, M. and Kusunose, K., “CFD Analysis on Sweep Angles of The Leading Edge and Trailing Edges of Wing in Supersonic Flow”, *Transactions of The JSME (In Japanese)*, Vol. 81, No.827, 2015, pp.15-37. <https://doi.org/10.1299/transjsme.15-00037>
- [4] Matsushima, K., Iwamiya, T. and Nakahashi, K., “Wing Design for Supersonic Transports using Integral Equation Method”, *Engineering Analysis with Boundary Elements*, Vol.28, Issue 3, 2004, pp.247-255. [https://doi.org/10.1016/S0955-7997\(03\)00055-9](https://doi.org/10.1016/S0955-7997(03)00055-9)
- [5] Sasaki, D., Obayashi, S. and Nakahashi, K., “Navier-Stokes Optimization of Supersonic Wings with Four Design Objectives using Evolutionary Algorithm”, *Journal of Aircraft*, Vol. 39, No. 4, 2002, pp.621-629. <https://doi.org/10.2514/2.2974>
- [6] Jones, D. R., Schonlau, M., and Welch, W. J., “Efficient Global Optimization of Expensive Black-Box Function”, *Journal of Global Optimization*, Vol.13, Issue 4, 1998, pp.455-492. <http://doi.org/10.1023/A:1008306431147>
- [7] Sacks, J., Welch, W.J., Mitchell, T. J., and Wynn, H. P., “Design and Analysis of Computer Experiments”, *Statistical Science*, Vol.4, No.4, 1989, pp.409-435. <http://doi.org/10.1214/ss/1177012415>
- [8] Hiroyasu, T., Miki, M. and Watanabe. S. “Divided Range Genetic Algorithm in Multiobjective Optimization Problems”, *Proceedings of International Workshop on Emergent Synthesis*, Kobe, Hyogo, 1999, pp.57-66.
- [9] Ye, K. Q., “Orthogonal Column Latin Hypercubes and Their Application in Computer Experiments”, *Journal of the American Statistical Association*, Vol.93, No.444, 1998, pp.1430-1439. <http://doi.org/10.2307/2670057>
- [10] Kodaira, T., Nakamoto, T., Koike, M., Amano, K., Nishii, R., and Qin, P., “Multidisciplinary Design Optimization for Car-Body Structure Using Sequential Design of Experiments”, *Journal of Society of Automotive Engineers of Japan*, Vol.44, No.2, 2013, pp.535-541 (in Japanese). <https://doi.org/10.11351/jsaeronbun.44.535>
- [11] Deb, K., Pratap, A., Agarwal, S. and Meyarivan, T., “A fast elitist multi-objective genetic

Chapter 2

- algorithm: NSGA-II”, *IEEE Transactions on Evolutionary Computation*, Vol.6, Issue 2, 2002, pp.182-197. <https://doi.org/10.1109/4235.996017>
- [12] Mitchell, M., “An Introduction to Genetic Algorithms”, A Bradford Book The MIT Press, 1998.
- [13] Eshelman, L. J. and Schaffer, J. D., “Real-coded genetic algorithms and intrval schemata, Foundations of Genetic Algorithms2”, *Morgan Kaufmann Publishers, Inc.*, 1993.
- [14] Inselberg, A., “The Plane with Parallel Coordinates”, *The Visual Computer*, Vol.1, Issue 2, 1985, pp.69-91.
- [15] Makino, Y., “Low Sonic boom Design of a Silent Supersonic Technology Demonstrator ~ Development of CAPAS and its Application ~”, The 4th SST-CFD Workshops (International Workshops on Numerical Simulation Technology for Design of Next Generation Supersonic Civil Transport), 2007, pp.697-704.
- [16] Horinouchi, S., Makino, Y. and Noguchi, M., “Conceptual Study of a Quiet Small Supersonic Transport (Part2)”, JSASS Paper 2009-5014, November 2009, (in Japanese).
- [17] Mack, R. J., “A Supersonic Business-Jet Concept Designed for Low Sonic boom”, NASA TM-2003-212435, October 2003.
- [18] Mascitti, V. R., “A Preliminary Study of the Performance and Characteristics of a Supersonic Executive Aircraft”, NASA TM-74055, September 1997.
- [19] Fenbert, J. W., Ozoroski, L., P., Geiselhart, K., A., Shields, E. W. and McElroy, M. O., “Concept Development of a Mach 2.4 High-Speed Civil Transport”, NASA TP-1999-209694, December 1999.
- [20] Robins, A. W., Dollyhigh, S. M., Beissner, F. L., Geiselhart, K., Martin, G. L., Coen, P. G. and Morris, S. J., “Concept Development of a Mach 3.0 High-Speed Civil Transport”, NASA TM-4058, January 1988.

Chapter 3 Planform Dependency Investigation of Low-Drag Supersonic Airfoil for Wing-Body-Nacelle Configuration

3.1 Introduction

In the previous chapter, the planform dependency of the low-drag airfoil design results was discussed with the aerodynamic designs of an airfoil for a cranked arrow wing and a single-tapered using EGO. Though variable knowledge was obtained from these studies, this information does not include the aerodynamic interference that occurs between the engine intake and the wing; an example of such interference is a shock wave, which occurs at the engine intake and affects the flow field of the wing. Thus, an integrated design in which the aerodynamic interference between each component (particularly the interference between the wing, the fuselage, and the engine) is considered should be employed from the beginning of the conceptual design process.

Thus, in this chapter, the design knowledge which had been obtained in previous study was developed by considering the effect of the aerodynamic interference between the engine intake and the wing. Therefore, a supersonic wing design problem was solved for a supersonic transport (SST) with an integrated engine intake and a nacelle. The following two planforms were considered: a quadruple-tapered wing with a large backward-swept angle and a single-tapered wing with a small backward-swept angle.

To consider the effect of the aerodynamic interference between the engine intake and the wing, a high-fidelity solver is required, which is significantly time consuming. If the number of individuals used for the optimization are decreased or a low-fidelity model is used in aerodynamic evaluation, the computation time reduces; however, it becomes more difficult to obtain optimum solutions. Even if a surrogate model was used to evaluate an object function in optimization such

as EGO, further efficiency improvement of optimization is expected. Thus, multi-fidelity approach and surrogate model method were applied to reduce the gross calculation time to evaluate samples. In the multi-fidelity approach, high-fidelity and low-fidelity evaluations are performed. Compared to optimization which is used only high-fidelity evaluation, the gross calculation time is reduced without any degradation in the performance of optimization. In the evolutionary calculation process employed in this study, each individual was evaluated via a surrogate model, and not via direct aerodynamic calculation, which also significantly reduced the calculation time.

3.2 Design Method

3.2.1 Overview of Multi-Fidelity Efficient Global Optimization

Multi-fidelity efficient global optimization [1] is a method that integrated the multi-fidelity approach with the efficient global optimization (EGO) [2]. The multi-fidelity approach is a method in which in a high-fidelity evaluation and a low-fidelity evaluation are simultaneously carried out to maintain the accuracy of the surrogate model. Figure 3-1 shows the flow chart of the multi-fidelity efficient global optimization used in this study. First, the initial samples for the high-fidelity evaluation and auxiliary samples for the low-fidelity evaluation were obtained. In this study, the low-fidelity evaluation takes approximately 30 min per sample and the high-fidelity evaluation takes approximately 12 h per sample. The initial and auxiliary samples were generated individually by Latin hypercube sampling (LHS) (See section 2.2.2). While the number of auxiliary samples was decided by Eq. (2-1), the number of initial samples was decided considering evaluation time [if N_{initial} in Eq. (2-1) initial samples can be evaluated in realistic time, it is better to use Eq. (2-1)]. After all samples were evaluated, the hybrid surrogate model was constructed. An additional sample was obtained with solving EI value [2] (see section 2.2.4)

maximization problem using the NSGA-II [3], which was executed in the space of a hybrid surrogate model consisting of a combined Kriging surrogate model [4] (see section 2.2.3) and radial basis function model [5] to save computational cost, and then evaluation was performed using a high-fidelity solver. The evaluation of this additional sample was then incorporated into an updated surrogate model. Subsequently, the optimal search was conducted again to obtain a new additional sample. This process was iterated until the solutions of subsequent models converged. The optimization process including the construction of the hybrid surrogate model was executed with a work station PC. The total calculation time was approximately 24 h excluding the aerodynamic calculations per loop.

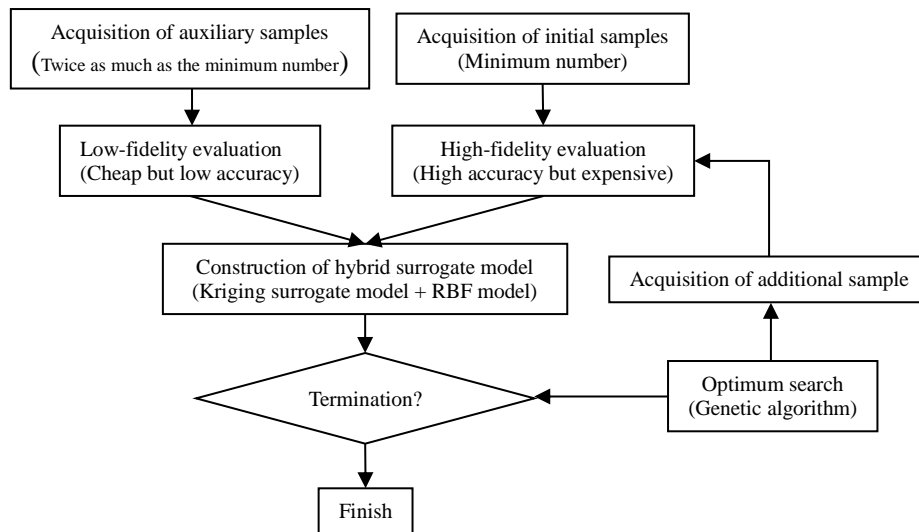


Figure 3-1 Flow chart of multi-fidelity efficient global optimization.

3.2.2 Surrogate Model

3.2.2.1 Radial Basis Function Model (RBF model)

An RBF [5] is a method for interpolating an unknown function via the superposition of localized basis functions. The $\hat{y}_{\text{RBF}}(\mathbf{x}_{\text{dv}})$ at an unknown design point \mathbf{x}_{dv} can be expressed as

$$\hat{y}_{\text{RBF}}(\mathbf{x}_{\text{dv}}) = \sum_{i=1}^N w_{\text{RBF}_i} \cdot \exp\left(-\beta_{\text{RBF}}|\mathbf{x}_{\text{dv}} - \mathbf{x}_{\text{dv}}^i|^2\right) \quad (3-1)$$

where N is the number of design samples, w_i denotes the weight coefficient of the i th design sample, and β_{RBF} represents a positive coefficient.

3.2.2.2 Hybrid Surrogate Model

To use the multi-fidelity approach, a hierarchical Kriging surrogate model [4] or a hybrid surrogate model [6], which connect a high-fidelity evaluation with a low-fidelity evaluation are useful. The hierarchical Kriging surrogate model refers to a surrogate model of a high-fidelity function that uses a Kriging surrogate model of a sampled low-fidelity evaluation as a model trend. In general, it is time consuming to construct a Kriging surrogate model because the maximization problem of a likelihood function must be solved. Thus, our hybrid surrogate model [1], was generated by the integration of the RBF model into the Kriging surrogate model, and it was developed for the multi-fidelity approach (Figure 3-2). An RBF model can be constructed more easily than a Kriging surrogate model. The integration of the RBF model into the Kriging surrogate model facilitates the description of a complex solution space. The hybrid surrogate model can be described using Eq. (8) as follows:

$$\hat{y}_{\text{hybrid}}(\mathbf{x}_{\text{dv}}) = \mu + \hat{y}_{\text{RBF}}(\mathbf{x}_{\text{dv}}) + \mathbf{r}(\mathbf{x}_{\text{dv}})^T \mathbf{R}^{-1}[\mathbf{f} - \mathbf{1}\mu - \mathbf{1}\hat{y}_{\text{RBF}}(\mathbf{x}_{\text{dv}})] \quad (3-2)$$

In this study, $\hat{y}_{\text{RBF}}(\mathbf{x}_{\text{dv}})$ was calculated using the data of auxiliary samples that were evaluated using the low-fidelity solver.

To update the hybrid surrogate model, in a study by Zhang, et al [7], the high-fidelity evaluation result and the low-fidelity evaluation result were added and the surrogate model were upgraded. This method was validated by solving the design problems of the airfoil and three-dimensional

wing. The difference of in the fidelity was only in term of the number of calculation grids. In contrast, in this study, the differences in the fidelity were in term of the governing equations and the geometric configurations used for the numerical simulations. In this study, the aerodynamic interference between the wing and the engine was focused on, and only the high-fidelity evaluation results were used for updating the hybrid surrogate model.

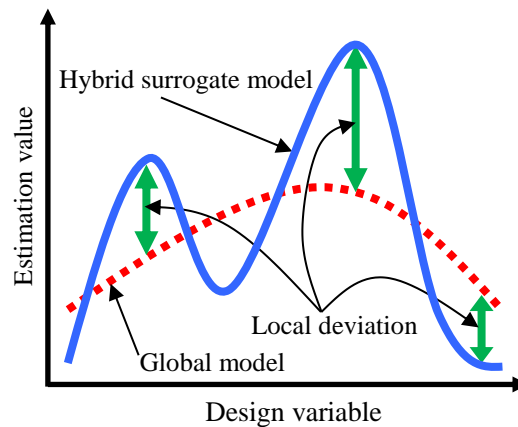


Figure 3-2 Concept of the hybrid surrogate model.

3.2.3 Optimization Method

In this study, NSGA-II was applied to solve the maximization problem of the EI which was the indicator of updating the surrogate model. An elite strategy [8] and the roulette wheel method [8] were used in the selection process, a blended crossover (BLX)-0.5 [9] was used in the crossover process, and uniform mutation [8] with a mutation rate of 0.1 was used in the mutation process.

3.3 Visualization Method of Design Results

A parallel coordinate plot (PCP) [10] which is a graphical method for visualizing multi-variate data, and was applied in this study for the observation of the trends in the representative solutions. In a PCP, the axes of the variables, such as the design variables and the objective functions, are parallel. Each sample is represented by a dashed line that intersects these axes. In this study, modeFRONTIER® version 4.4.4, developed by ESTECO®, was used to generate the PCPs.

In addition, a functional analysis of variance (functional ANOVA) which was mentioned in Section 2.3 was also used for the investigation for the relationship between the object function and the design variables.

3.4 Aerodynamic Evaluation

3.4.1 High-Fidelity Evaluation

The governing equation of the high-fidelity evaluation was the compressible Euler equation:

$$\frac{\partial}{\partial t} \int_V \mathbf{q} dV + \int_S \mathbf{H} \cdot \mathbf{n} dS = 0 \quad (3-3)$$

where \mathbf{q} is a conservative vector, \mathbf{H} is an inviscid flux vector, and \mathbf{n} is the outward normal vector on the boundary surface of a control volume. To evaluate the numerical functions, the Harten-Lax-van Leer-Einfeldt-Wada (HLLW) scheme [11] was employed. Additionally, the lower-upper symmetric Gauss-Seidel (LU-SGS) implicit method [11] was used for time integration. The number of calculation grids was approximately 30 million. The FAST Aerodynamic Routines (FaSTAR) [12] approach was used as the aerodynamic solver. An unstructured hexahedral mesh was generated around the aircraft using HexaGrid [13,14], an automatic mesh generation software package developed by JAXA. These calculations were performed on the JAXA Supercomputer System Generation 2 (JSS2) to evaluate the high-fidelity configuration, which integrated the engine intake and the flow through the nacelle.

3.4.2 Low-Fidelity Evaluation

The low-fidelity evaluation method was same as Section 2.4. Calculations based on the potential equation were performed to the low-fidelity configuration in which the engine intake and the nacelle were not present.

3.5 Design Problems

3.5.1 Design Targets and Design Cases

All components except for the main wing used in this study, were based on the concept model for the next-generation supersonic civil transport proposed by the Japan Aerospace Exploration Agency (JAXA). This concept has 36-50 seats and can cruise at Mach 1.6. The length of the body is 47.8 m. The following two planforms were considered for the wing design: a quadruple-tapered wing with a large backward-swept angle (Case 1), which matches the concept model proposed by JAXA, and a single-tapered wing with a small backward-swept angle (Case 2), which is similar to the planform proposed for the Aerion AS2. An overview of the planforms, indicating the locations of the defined cross sections, is shown in Figure 3-3.

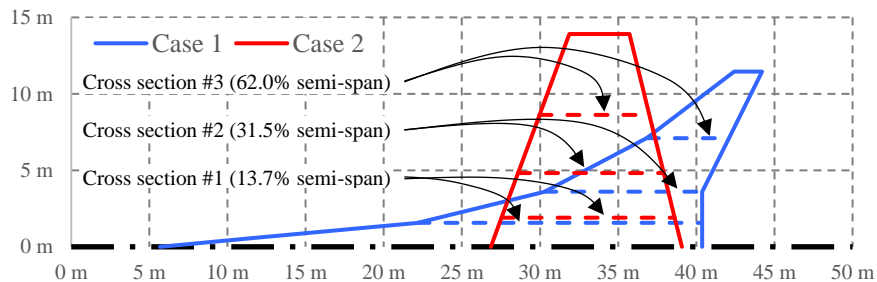


Figure 3-3 Overview of the two evaluated wing planforms.

3.5.2 Modified Parametric Section (PARSEC) for Airfoil Definition

The parametric section (PARSEC) method [15], modified according to a study by Kanazaki, et al [16] was used to define the airfoil geometries. In this method, the thickness and camber of the airfoil were defined individually, allowing various airfoils to be described (including super critical airfoils, thin airfoils, and airfoils with a large leading edge radius) because the center of the leading edge radius can be positioned on the camber line. This method that has been previously applied to various wing designs, such as a transonic airfoil [17], the SST airfoil [18],

and a low Reynolds number airfoil [19]. The distribution of airfoil thickness and camber are defined by Eqs. (3-4) and (3-5), respectively.

$$z_t(x) = \sum_{n=1}^6 a_n \times x^{\frac{2n-1}{2}} \quad (3-4)$$

$$z_c(x) = b_0 \times \sqrt{x} + \sum_{n=1}^5 b_n \times x^n \quad (3-5)$$

Where z_t denotes the distribution of the airfoil thickness; a_n denotes a real coefficient; x denotes a coordinate along the chord direction; z_c denotes a camber height; b_0 denotes a real coefficient; and b_n denotes a real coefficient.

3.5.3 Design Space

The design space was defined for the three cross sections shown in Figure 3-3. A total of two variables per cross section (including the twist angle) were present in the modified PARSEC method. If all the geometric parameters of all cross sections were defined as design variables, the design space would become considerably large. Therefore, the five variables that were found to contribute most significantly to drag reduction in a previous research [20] were extracted from the full set of variables. To ensure the diversity of the solution, the range of the design variables was set wider than that in the study [20]. The five selected variables and their ranges of variation are provided in Table 3-1. The values of the remaining parameters were fixed to match the values developed for the SST by JAXA. The change in geometry between each section was then interpolated using a spline curve.

Table 3-1 Design space.

			Lower bound	Upper bound
The curvature radius of the camber at the leading edge	Cross section #2	$dv1$	-0.00025	0.00025
	Cross section #3	$dv2$	-0.00025	0.00025
Location of maximum camber	Cross section #1	$dv3$	0.35	0.55
Maximum camber height	Cross section #2	$dv4$	-0.0050	0.0015
Twist angle (Twisted-down direction is positive)	Cross section #2	$dv5$	-1.0°	2.0°

3.5.4 Objective Function and Constrains

The objective function pertaining to drag reduction in the supersonic cruise condition was defined as follows:

$$\text{Minimize: } C_{DP} \text{ at } M_{\infty} = 1.6$$

$$\text{Subject to } L = W$$

$$X_{CP} = X_{CG}$$

Through the aerodynamic evaluation, the pressure drag coefficient C_{DP} of the planforms at Mach 1.6 was determined under two constraints considered to ensure level flight. These two constraints were same as the study of Chapter 2.

3.6 Results and Discussion

3.6.1 Validation of Configuration Fidelity

In this study, the configuration fidelity was added to the fidelity of the aerodynamic solver, regardless of the integration of the engine intake and the nacelle in the calculation. To validate the concept of configuration fidelity, the aerodynamic performance was compared in terms of high-fidelity and low-fidelity configurations, as shown in Figure 3-4. Each initial sample of Case 1 had the same combination of design variable values as that of Case 2. The number of initial samples was 15. Figure 3-4 shows that 15-20 drag counts increased in each sample for Case 1, and 30-45 drag counts increased in each sample for Case 2, when the engine intakes and the nacelles were integrated. However, the magnitude of the drag for the initial samples does not change in the both cases regardless of the integration of the engine intakes and nacelles. This shows that the effect of the presence or absence of engine intakes and nacelles does not contribute to the drag as much as the wing configuration. Therefore, the multi-fidelity designs that were used in this study considered the configuration fidelity in addition to the fidelity of the aerodynamic solver, because a global trend might be obtained even after considering the configuration fidelity.

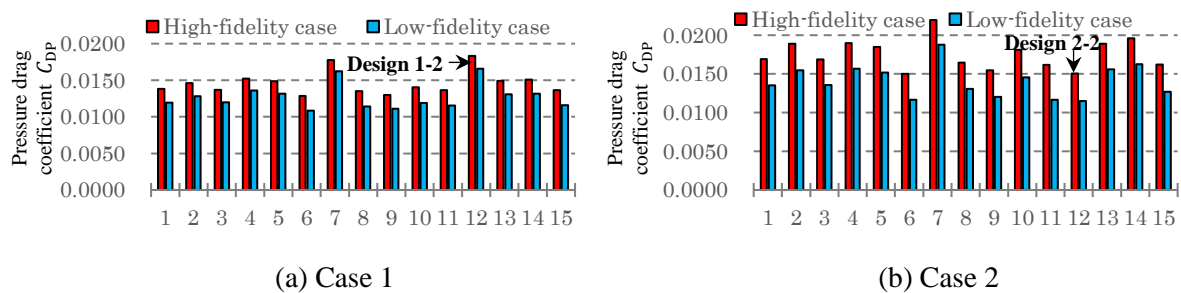


Figure 3-4 Aerodynamic performance of initial samples via Euler simulation.

3.6.2 Sampling Results

To obtain the global trend in the solution space, the low-fidelity solver evaluated 40 samples. In this optimization, the total generation number is 100 and the size of population is 64. The population is divided into four sub-populations. The additional sampling was iterated until a sample with a drag lower than that of the minimum value among the initial samples was obtained. Figure 3-4 and Figure 3-5 show the aerodynamic performance of the initial samples and the additional samples. According to Figure 3-4, most of the samples in Case 1 exhibited lower-drag than those in Case 2, except for Design 1-2 (Case 1) and Design 2-2 (Case 2), owing to the positions of the engine intake and nacelle. These positions were determined for JAXA's SSBJ model, which is the same wing planform as used in Case 1. Therefore, a different shape and relative position should be optimum for Case 2. The additional sampling process was conducted 10 times for Case 1 and 15 times for Case 2. This increased sampling may be caused by the different difficulties of improving each surrogate model. To investigate this difference, a leave-one-out cross validations (LOOCV) [21] was conducted. The LOOCV compares the true solution for a design point with its approximate solution estimated by the surrogate model that was constructed for all design points except for the initial design point. Figure 3-6 presents cross validation results for Case 1 and Case 2. It is noted that if most of the designs are located near or on the diagonal dashed line in Figure 3-6, the approximate value based on the surrogate model is close to the actual measured value, indicating that the surrogate model is accurate. For Case 1, most designs are closely distributed along the diagonal dashed line. On the contrary, several designs in Case 2 are far from the diagonal dashed line, though the number of additional sampled was higher in Case 2 than in Case 1. This implies that the structure of the solution space of Case 2 was more complex than that for Case 1. A wing with a small backward-swept angle, such as that in Case 2, tends to generate a shock wave at its leading edge, suggesting that the shape of the

leading edge in Case 2 may be more sensitive to drag reduction measures than that in Case 1.

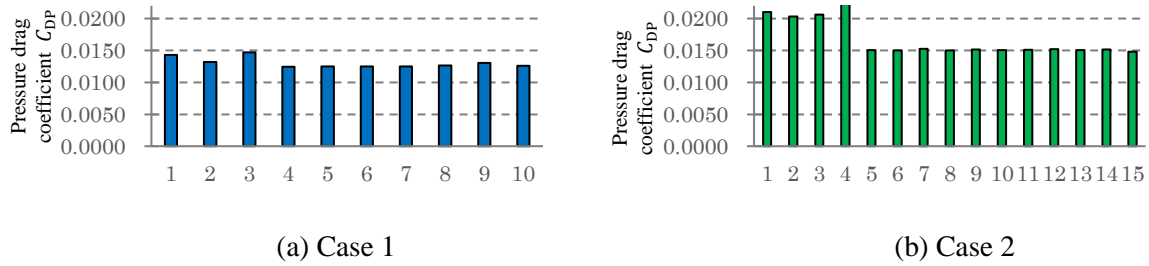


Figure 3-5 Aerodynamic performance of additional samples via Euler simulation.

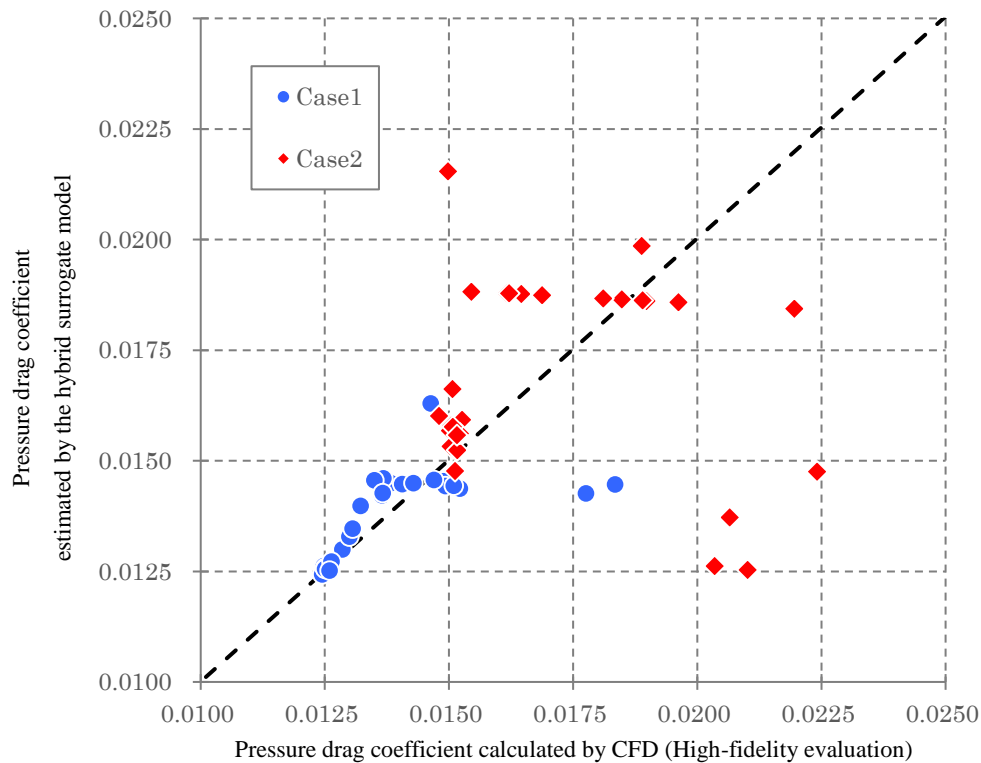


Figure 3-6 Results of LOOCV for the hybrid surrogate model.

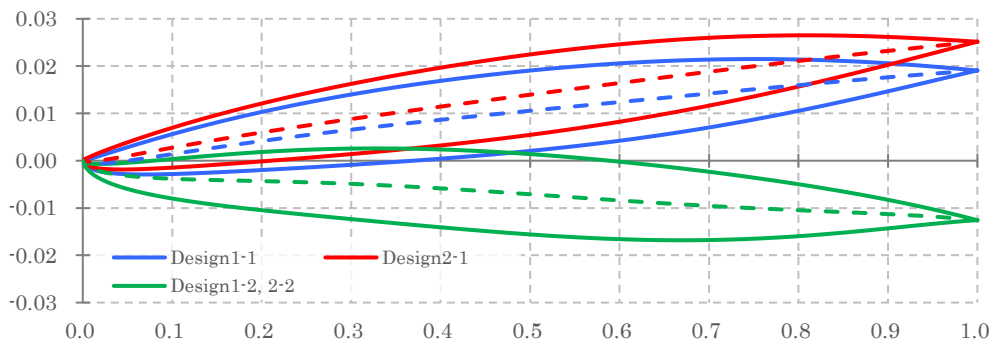
3.6.3 Difference between Low-Drag Airfoil Distribution for Each Case

3.6.3.1 Geometric Difference

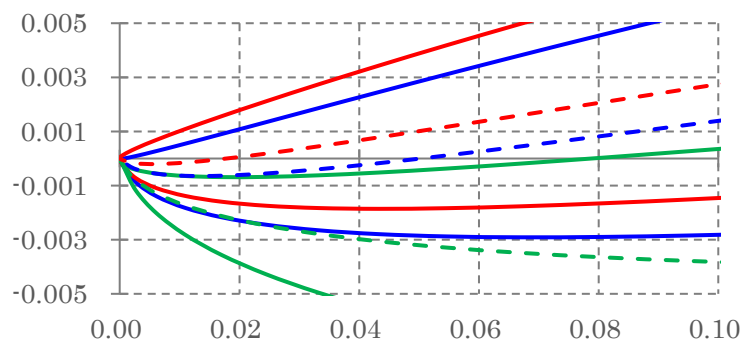
Figure 3-7 shows the airfoil geometries of the representative solutions at Cross section #2 at which most of the lift was generated. Design 1-1 is the lowest drag solution among the Case 1 solutions and Design 2-1 is the lowest drag solution among the Case 2 solutions. Design 1-2 is a relatively high-drag solution compared to the other Case 1 solutions. Design 2-2 is a relatively

low-drag solution compared to other Case 2 solutions, and it also has the same airfoil distribution as that of Design 1-2. Compared to Design 1-1 and Design 2-1, the largest difference was the twisted down angle and that of Design 2-1 was larger than that of Design1-1. It is assumed that the twisted down angle is one of the key factors of drag reduction.

Figure 3-7 shows that Design 1-2 and Design 2-2 are significantly different from the low-drag solutions of Design 1-1 and Design 2-1. The greatest difference is at the leading edge: Design 1-2 and Design 2-2 have an upward-pointing leading edge; in other words, their camber is convex downward, whereas the airfoil geometry at Cross sections #1 and #3 of Design 1-2 and Design 2-2 do not have such a leading edge.



(a) Overview.



(b) Detail of the leading edge.

Figure 3-7 Airfoil geometries of representative solutions at Cross section #2.

3.6.3.2 Aerodynamic Characteristics Difference

The distributions of the surface pressure coefficient C_p are shown in Figure 3-8. A higher pressure can be seen on the lower leading edges of Design 2-1 and Design 2-2 than that at the leading edges of Design 1-1 and Design 1-2. This phenomenon can be attributed to the fact that a wing with a small sweep leading edge tends to cause a shock wave, which affected the flow-field on the upper surface. The low pressure on the outer upper surface of Design 1-1 and Design 1-2 is lower than that for the upper surface of Design 2-1 and Design 2-2. To reduce drag in Case 2, it is required that the leading edge prevents the flow acceleration. Thus, twisted cross sections or an upward-pointing leading edge are effective to reduce the drag in Case 2. The cross-sectional C_p distribution along Cross section #2 is shown in Figure 3-9. It can be observed that in Case 2, the pressure rise of Design 2-2 at the leading edge which has an upward-pointed leading edge was weaker than that of Design 2-1 which has no upward-pointed leading edge. However, in Case 1, which has a large backward-swept angle, a shock wave does not tend to occur at the leading edge because of the swept-wing effect, even if the flow on the leading edge accelerates. Therefore, it can be observed in Figure 3-9 (a) that Design 1-2 cannot generate lift uniformly along the chord direction and the trim drag is high. This can be confirmed by consulting the flow fields: as can be seen in Figure 3-8, In Design 1-2, a strong shock wave can be seen at the leading edge of the horizontal wing compared to Design 1-1. As a result, the configuration of airfoil geometries in Design 1-2 cannot be a low drag solution for Case 1.

To focus on the interference between the wing and the engine, the distribution of the surface pressure coefficient C_p of the clean configuration solutions calculated by the Euler solver are shown in Figure 3-10, which, when compared to Figure 3-8, reveal the aerodynamic interference between the wing, engine intake and nacelle. The pressure on the upper wing surface of the trailing edge, from the root to the center of the clean configuration in Design 1-1 [Figure 3-10 (a)], is

clearly lower than that of the engine-integrated configuration of the same design [Figure 3-8 (a)]. A similar trend can be observed for Design 2-1 when comparing Figure 3-8 (c) and Figure 3-10 (b). These differences are caused by the interference with the upper-wing flow of the shock wave that occurs at the engine intake. Because force acts from a high-pressure region to a low-pressure region, the wing drag of the engine-integrated configuration becomes smaller than that of the clean configuration through the pressure on the upper wing surface of the trailing edge, from the root to the mid of the half span.

The pressure drag coefficient C_{DP} for each component of Design 1-1 and Design 2-1 are shown in Figure 3-11. While the wing C_{DP} was the highest among all components of Design 1-1, the component that shows the highest C_{DP} for Design 2-1 was the fuselage, as can be seen in Figure 3-11. The reasons for this difference are likely the interference between the fuselage and the wing, as well as the area rule. Figure 3-12 depicts the surface C_p distributions near the engine intake. A shock wave, caused by the engine intake, interferes with the flow on the upper surface of the wing in Design 2-1, and along the surface of the fuselage, though the shock wave which caused from the engine intake was not transferred to the surface of the fuselage and the wing in Design 1-1. This interference may cause wave drag, indicated by the higher fuselage C_{DP} of Design 2-1 than that for Design 1-1. Figure 3-13 shows the cross-sectional area distributions of Design 1-1 and Design 2-1. If a cross-sectional area distribution curve is close to the cross-sectional distribution curve of a Sears-Haack body [22], the area rule is satisfied and the aerodynamic drag at transonic to supersonic speeds becomes small. Figure 3-13 indicates that Design 1-1 was more similar to the Shears-Haack body than Design 2-1 was, and that the fuselage drag of Design 2-1 became larger than that of Design 1-1.

Observing Figure 3-12, the pressure on the surface of the engine nacelle in Design 2-1 is clearly lower than that in Design 1-1. In Design 2-1, the flow on the surface of the wing accelerated and

Chapter 3

expanded after it had reduced and compressed because of the shock wave generated at the entrance of the engine intake, and this expansion transferred to the flow on the engine nacelle. It is expected that the performance of the engine intake will not be reduced in this case, because compressed flow could appear. Figure 3-14 depicts the cross-sectional C_p distributions in the wing span direction, in which it can be observed that the positive pressure on the engine intake in Design 2-1 transfers to flow on the upper surface of the wing and interferes more strongly than in Design 1-1.

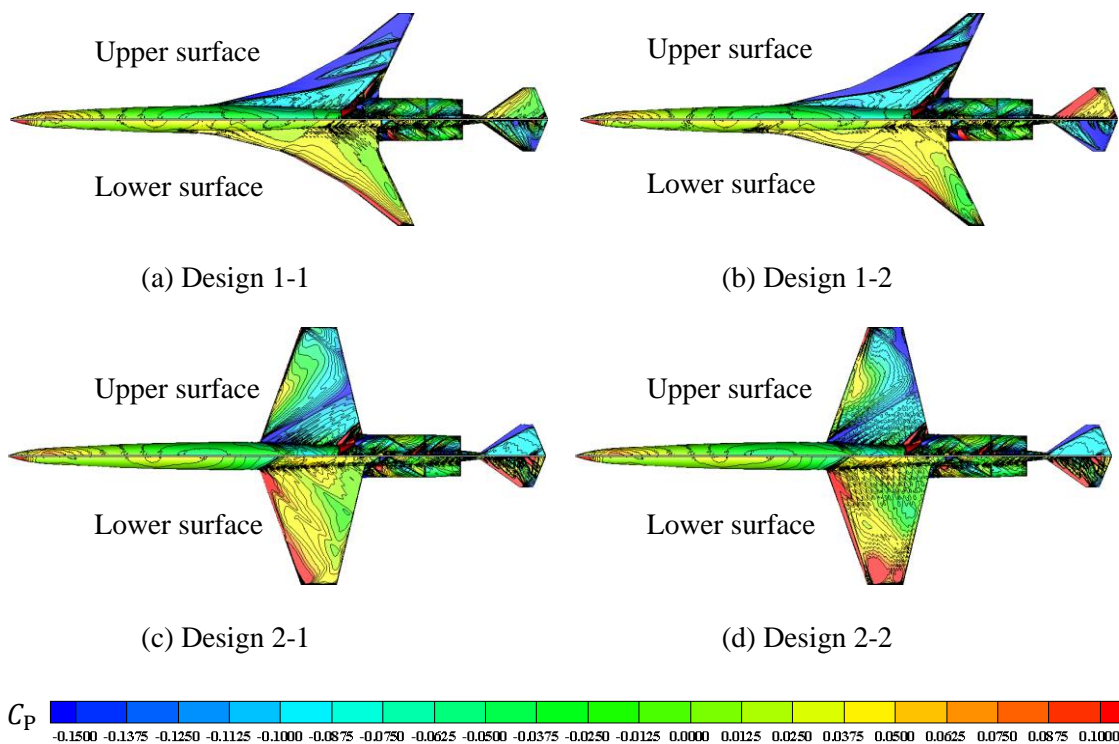


Figure 3-8 Surface C_p distributions of representative solutions (engine-integrated) by Euler simulation.

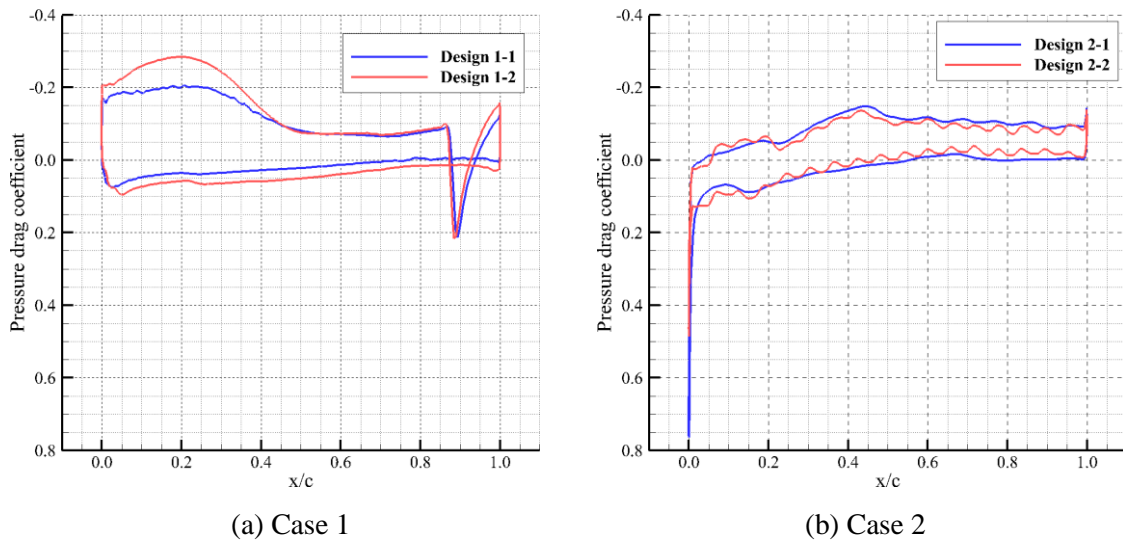


Figure 3-9 Cross-sectional C_p distribution for the representative solutions along Cross section #2.

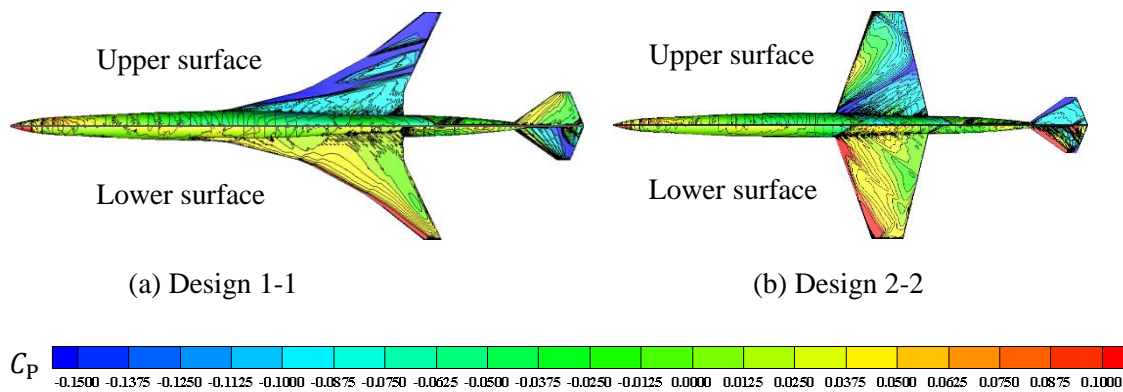


Figure 3-10 Surface C_p distributions of representative solutions (clean configuration) by Euler simulation.

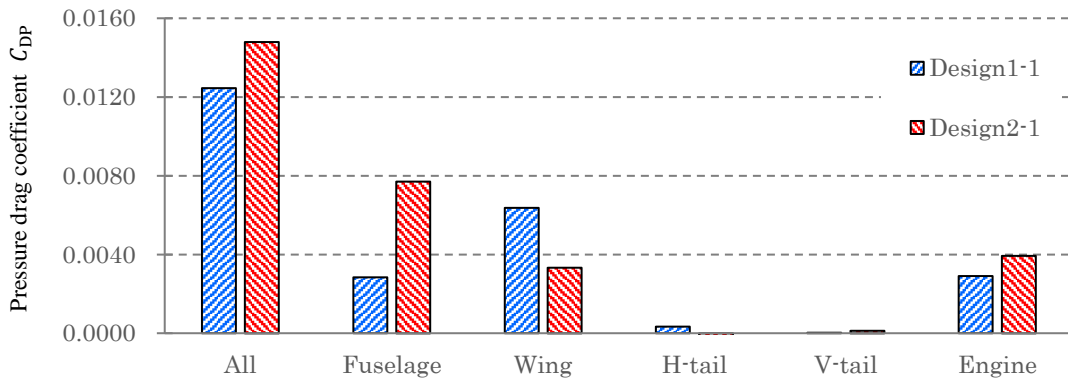


Figure 3-11 Values of C_{DP} for each component of the representative solutions by Euler simulation.

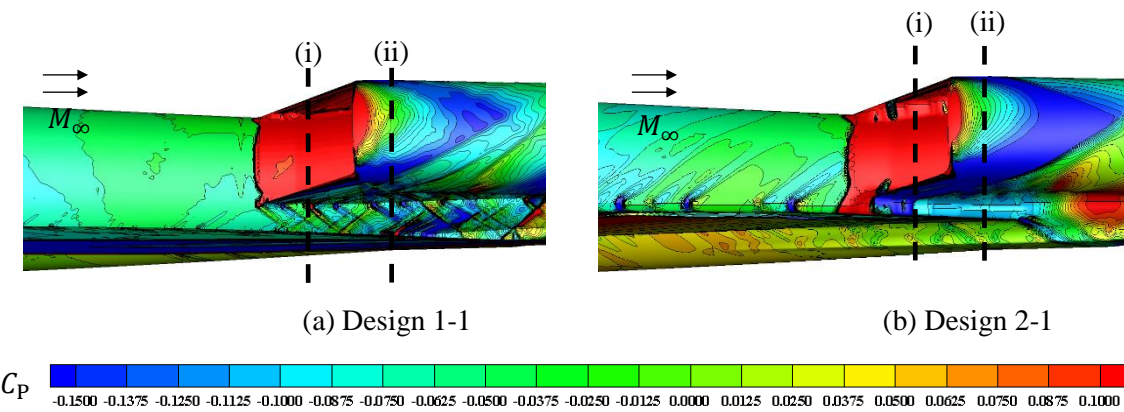


Figure 3-12 Surface C_p distributions near the engine intake and nacelle.

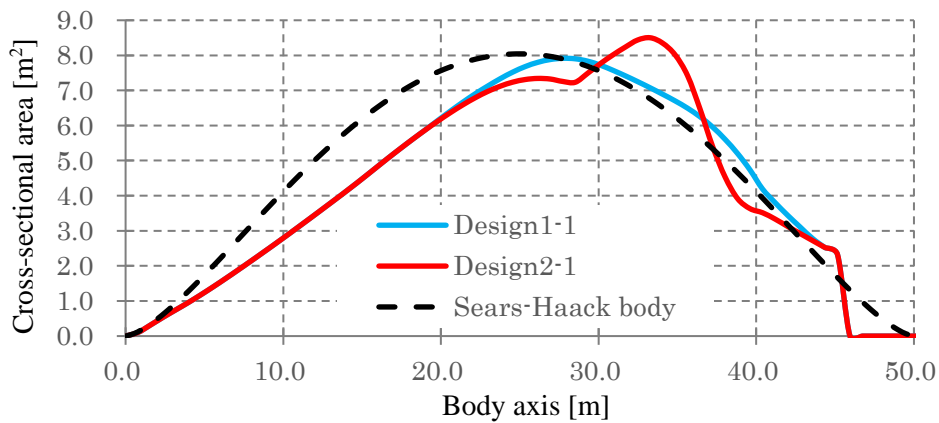


Figure 3-13 Cross-sectional area distribution along the body axis.

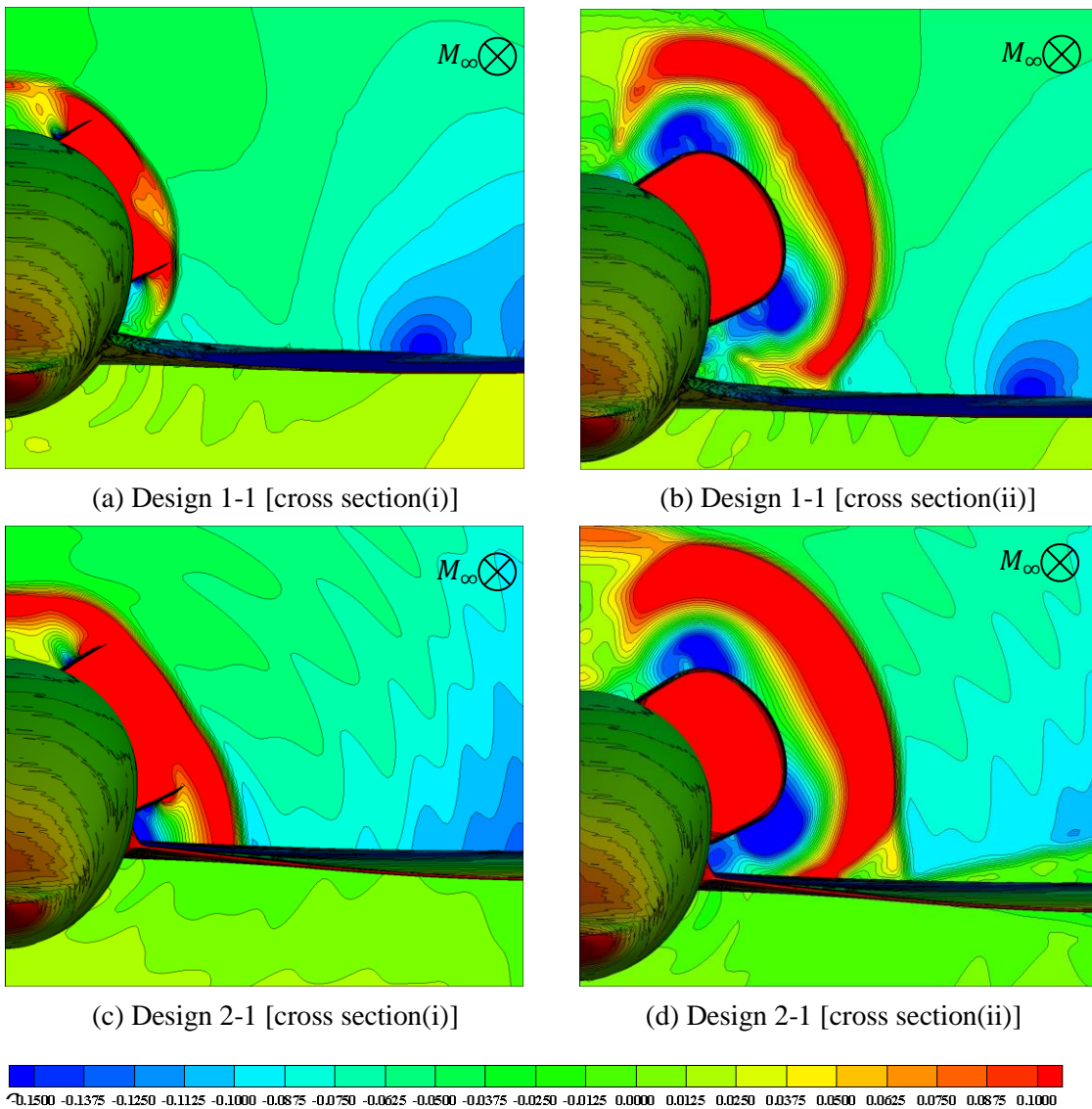


Figure 3-14 Cross-sectional C_p distributions near the engine intake (from front side).

The cross sections of each figure were defined in Figure 3-13.

3.6.4 Trend of Solution Space

3.6.4.1 Knowledge Discovery by Functional ANOVA

Figure 3-15 shows the contribution ratios of the design variables to the drag coefficient for the two cases evaluated. In both cases, $dv3$ (the location of the maximum camber at cross section #1) and $dv5$ (the twist angle of Cross section #2), which are the inner wing parameters, accounted for over 90% of the total contribution ratio. The high contribution ratio of $dv5$ confirms the assumption mentioned in Section 5.2.1 that the angle of twist is a key factor for reducing drag. The chord length of the outer wing was smaller than that of the inner wing; thus, the aerodynamic force on the outer wing was weaker than that on the inner wing and hence, the contribution ratios of the cross sections #1 and #2 are higher than that of Cross section #3. Notably, the order of the design variable contribution ratios is different for each case. For example, $dv3$ (the location of the maximum camber in Cross section #1) of Case 2 presents a higher contribution ratio than that of Case 1. Figure 3-16 present the deviations of the C_{DP} of the design variables, which indicate a high contribution ratio for the drag reduction shown in Figure 3-15. These figures show how the value of an objective function changes when the value of the design variables changes. Thus, the optimum value of the design variable can be estimated with these figures based on the surrogate model. According to Figure 3-16 (b), Case 1 and Case 2 exhibit a similar trend, and the value that exhibits the local minimum of deviation corresponds between the two (approximately $dv5 \approx 1.0$). This finding agrees with the theory that if a wing is twisted down a little, lift decreases on the outer wing, causing the wing tip vortices to become weak, thereby reducing the induced drag. Regarding $dv3$, on the contrary, a different trend can be observed from Figure 3-16 (a): There are more local minimum values in Case 2 than in Case 1. The design variable $dv3$ is located at the root of the wing, and thus, it might affect the aerodynamic interference between the wing, fuselage, and engine. In Case 2, a shock wave on the leading edge tends to be generated in supersonic cruise

because the backward-swept angle is small. Therefore, the aerodynamic drag is more sensitive to the shape of the leading edge in Case 2 than that in Case 1.

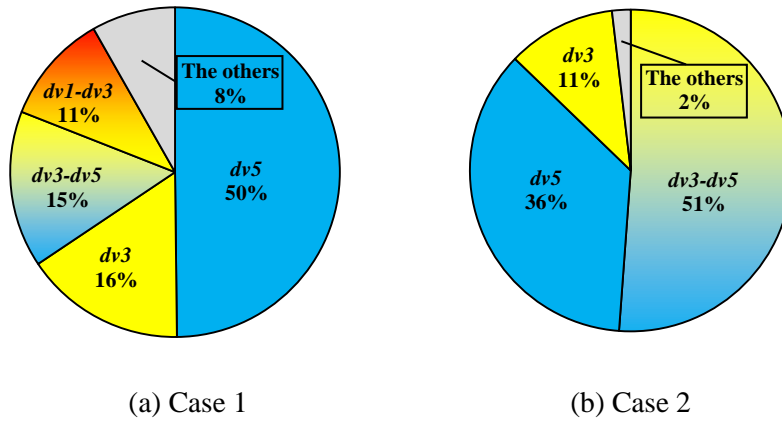


Figure 3-15 Contribution ratios of design variables to C_{DP} (the functional ANOVA results). (“The others” denotes the remaining design variables given in Table 3-1 but not shown.)

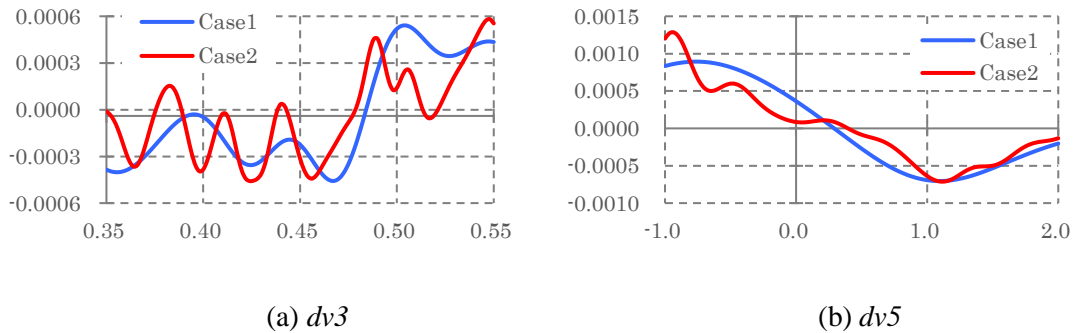


Figure 3-16 Local deviation of C_{DP} .

3.6.4.2 Knowledge Discovery by PCP

Figure 3-17 shows the PCPs of the initial and additional samples. In this figure, each line represents each design and their colors represent the magnitude of the pressure drag coefficient: blue indicates lower values and red indicates higher values. Thus, the most intense blue line indicates a low drag design that could likely be most successfully optimized.

The design variable $dv3$ (location of the maximum camber in Cross section #1) presented a

Chapter 3

high contribution ratio in Figure 3-15, indicating a potential low-drag solution for Case 1, when its value is approximately 0.44c, and in Case 2 when its value is approximately 0.42c. If $dv3$ becomes smaller, the leading edge of the cross section can be further changed. Case 2 tends to generate a shock wave at the leading edge of the wing; thus, Case 2 requires a thinner leading edge than Case 1 to avoid the generation of the shock wave.

For $dv5$ (twist angle of Cross section #2), the low-drag solutions in Case 1 are approximately 1.1° , while those in Case 2 are approximately 1.4 . Here, the cruising AoA for the low-drag solutions in Case 1 is approximately 3.8° , while that in Case 2 is approximately 3.0° . The actual AoAs against the freestream near Cross section #2 are approximately 2.7° in Case 1 and 1.6° in Case 2. This result can be considered reasonable because such a trend is required to obtain a lower wave drag in the case of a smaller backward-swept angle, such as in Case 2.

Thus, the optimization for Case 2 was advanced in the direction that $dv3$ converged to smaller value than that of Case 1 to improve the ability to describe the leading edge and $dv5$ converged to more horizontal value than that of Case 1.

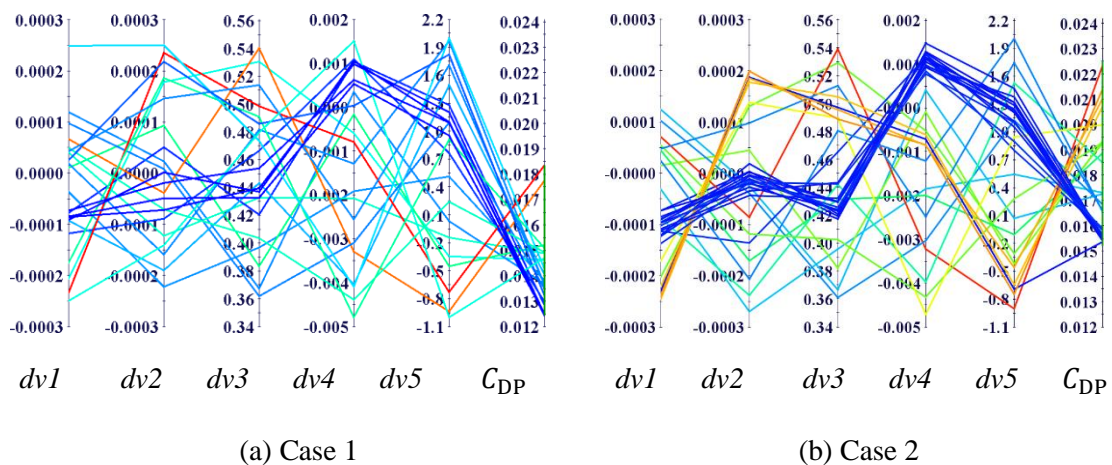


Figure 3-17 Visualization of design variables and C_{DP} for all samples determined by PCP.

3.6.5 Conclusion

In this study, to investigate the performance of different supersonic wing planform shapes with different backward-swept angles and an integrated engine intake, airfoil geometries distribution of wing were designed to minimize aerodynamic drag in supersonic cruise for a quadruple-tapered wing with a large backward-swept angle and a single-tapered wing with a small backward-swept angle. To improve the efficiency of the design process, a multi-fidelity design method with a hybrid surrogate model was applied to the wing optimization. An analysis of variance was used to discover the most influential design parameters and several sample designs were chosen to compare the wing performance.

According to the design results, the front camber shape and twist angle of the mid-span cross section were most efficient to promote drag reduction, regardless of the wing planform shape. For a wing planform with a large backward-swept angle, a cross section that has a positive camber at its leading edge and a slightly downward-twist angle were most effective in reducing drag in supersonic cruising. In contrast, for a planform with a small backward-swept angle, a cross section that has a negative camber at its leading edge, a thinner leading edge and a more prominent downward-twist angle is most effective in reducing drag in supersonic cruise.

Reference

- [1] Ariyarat, A., Sugiura, M., Tanabe, Y. and Kanazaki, M., “Hybrid Surrogate-Model-Based Multi-Fidelity Efficient Global Optimization Applied to Helicopter Blade Design”, *Engineering Optimization*, Vol.50, Issue 6, 2017, pp. 1016-1040. <https://doi.org/10.1080/0305215X.2017.1367391>
- [2] Jones, D. R., Schonlau, M., and Welch, W. J., “Efficient Global Optimization of Expensive Black-Box Function”, *Journal of Global Optimization*, Vol.13, Issue 4, 1998, pp.455-492. <http://doi.org/10.1023/A:1008306431147>
- [3] Deb, K., Pratap, A., Agarwal, S. and Meyarivan, T., “A fast elitist multi-objective genetic algorithm: NSGA-II”, *IEEE Transactions on Evolutionary Computation*, Vol.6, Issue 2, 2002, pp.182-197. <https://doi.org/10.1109/4235.996017>
- [4] Sacks, J., Welch, W.J., Mitchell, T. J., and Wynn, H. P., “Design and Analysis of Computer Experiments”, *Statistical Science*, Vol.4, No.4, 1989, pp.409-435. <http://doi.org/10.1214/ss/1177012415>
- [5] Buhmann, M. D., “Radial Basis Functions: Theory and Implementations (Cambridge Monographs on Applied and Computational Mathematics)”, *Cambridge University Press*, 2003.
- [6] Han, Z. -H., and Goertz, S., “Hierarchical Kriging Model for Variable-Fidelity Surrogate Modeling”, *AIAA Journal*, Vol. 50, No. 9, 2012, pp. 1885-1896. <https://doi.org/10.2514/1.J051354>
- [7] Zhang, Y., Han, Z-H., and Zhang, K-S., “Variable-fidelity expected improvement for efficient global optimization of expensive functions”, *Structural and Multidisciplinary Optimization*, Vol. 58, Issue 4, 2018, pp. 1431-1451. <http://doi.org/10.1007/s00158-018-1971-x>
- [8] Mitchell, M., “An Introduction to Genetic Algorithms”, A Bradford Book The MIT Press, 1998.
- [9] Eshelman, L. J. and Schaffer, J. D., “Real-coded genetic algorithms and intrval schemata, Foundations of Genetic Algorithms2”, *Morgan Kaufmann Publishers, Inc.*, 1993.
- [10] Inselberg, A., “The Plane with Parallel Coordinates”, *The Visual Computer*, Vol.1, Issue 2, 1985, pp.69-91. <http://doi.org/10.1007/BF01898350>
- [11] Sharov. D. and Nakahashi K., “Reordering Hybrid Unstructured Grid for Lower-Upper Symmetric Gauss-Seidel Computations”, *AIAA Journal*, Vol. 36, No. 3, pp. 484-486, 1998. <https://doi.org/10.2514/2.392>
- [12] Hashimoto A., Murakami K., Aoyama T., Ishiko K., Hishida M. and Sakashita M., “Toward

- the Fastest Unstructured CFD code “FaSTAR””, AIAA Paper 2012-1075, November 2012.
<https://doi.org/10.2514/6.2012-1075>
- [13] Lahur, P. R., “Automatic Hexahedra grid generation method for component-based surface geometry”, AIAA Paper 2005-5242, January 2005. <https://doi.org/10.2514/6.2005-5242>
- [14] Hahimoto, A., Murakami, K. and Aoyama, T., “Lift and Drag Prediction Using Automatic Hexahedra Grid Generation Method”, AIAA Paper 2009-1365, January 2009. <https://doi.org/10.2514/6.2009-1365>
- [15] Sobieczky, H., “Parametric Airfoils and Wings”, *Notes on Numerical Fluid Mechanics*, Vol.68, 1998, pp.71-88. https://doi.org/10.1007/978-3-322-89952-1_4
- [16] Kanazaki, M., Sato, T., and Matsushima, K., "Parametric Airfoil Representation Toward Efficient Design Knowledge Discovery under Various Flow Condition", *Transaction of The Japan Society for Aeronautical and Space Science, Aerospace Technology Japan*, Vol. 12, Issue APISAT-2013, 2014, pp. a93-a98. <https://doi.org/10.2322/tastj.12.a93>
- [17] Oyama, A., Obayashi, S. and Nakamura, T., “Real-Coded Adaptive Range Genetic Algorithm Applied to Transonic Wing Optimization”, *Applied Soft Computing*, Vol.1, Issue 3, 2001, pp. 179-187. [https://doi.org/10.1016/S1568-4946\(01\)00017-5](https://doi.org/10.1016/S1568-4946(01)00017-5)
- [18] Yotsuya, T., Kanazaki, M., Makino, Y., and Matsushima, K., "Multi-point Design of a Supersonic Wing Using Modified PARSERC Airfoil Representation", 10th World Congress on Computational Mechanics, Vol.1, No.1, 2012, São Paulo, Brazil. <https://doi.org/10.5151/meceng-wccm2012-16733>
- [19] Kanazaki, M., Utsuki, M., Sato, T. and Matsushima, K., "Airfoil Design for Martin Airplane Considering Using Global Optimization Methodology", *International Journal of Aerospace System Engineering*, Vol.2, No.2, 2015, pp.10-14.
- [20] Arai, S., Kanazaki, M. and Makino, Y., “Design Optimization of Supersonic Wing for Engine/ Airframe Configuration”, JSASS Paper 2015-5087, October 2015, (in Japanese).
- [21] Arlot, S. and Celisse, A., “A Survey of Cross-Validation procedures for Model Selection”, *Statistics Surveys*, Vol. 4, 2010, pp.40-79. <https://doi.org/10.1214/09-SS054>
- [22] Palaniappan, K. and Jameson, A., “Bodies Having Minimum Pressure Drag in Supersonic: Investigating Nonlinear Effects”, *Journal of Aircraft*, Vol.47, No.4, 2010, pp.1451-1454. <https://doi.org/10.2514/1.C031000>

Chapter 4 Planform Dependency of Low-Drag Low-Boom Supersonic Airfoil for a Wing-Body-Nacelle Configuration

4.1 Introduction

Chapter 2 and Chapter 3 focused on designs for drag reduction. Designs for sonic boom reduction are also required to realize SST. Backward-swept wings (such as delta cranked arrow wings) can reduce wave drag near sonic speeds; however, they have difficulty in significantly reducing sonic boom because of the lift caused by the horizontal tail and the tip of the main wing. Thus, satisfying “Darden’s rule”, which is a theoretically ideal equivalent of cross-sectional area distribution for sonic boom reduction, is difficult, and good design concepts that achieve simultaneous reduction of drag and sonic boom are required. A forward-swept wing is one such concept. In a study by Horinouchi [1], wind tunnel experiments and numerical calculations were conducted to evaluate the sonic boom of an SSBJ with a variable forward-swept wing. The results of the study suggested that a forward-swept wing is possibly superior to a conventional backward-swept delta wing for reducing the impact of sonic booms. This means that if the pressure propagation along the Mach cone caused by the tip of a forward-swept wing goes ahead of the Mach cone caused by the nose, sonic boom reduction through optimization of the lift equivalent cross-sectional area distribution (unless the actual cross-sectional distribution is drastically changed) can be achieved. However, few studies have investigated the sonic boom performance of a forward-swept wing. In the study by Horinouchi [1], only one forward-swept wing configuration was evaluated; the three-dimensional pressure propagation was not numerically calculated to estimate the impact of sonic boom. Thus, a higher fidelity investigation is required.

The purpose of this chapter is to demonstrate the potential of a forward-swept wing in reducing

aerodynamic drag and the impact of sonic boom, and to obtain design knowledge regarding the relationship between supersonic wing planforms, including a forward-swept wing. To accomplish these, two steps were carried out. First, a parametric study to investigate the aerodynamic performance of the wing planform was conducted with changing backward-swept and forward-swept angles. The sonic boom was evaluated based on three-dimensional pressure propagation using the Euler equation for near-field pressure distribution of aircraft. Multipole analysis [2] and an augmented Burgers equation [3] were then employed. Second, low-drag low-boom wing design problems were solved using a GA-based optimizer for an SSBJ with a forward-swept wing and one with a backward-swept wing to reveal design knowledge regarding the difference of optimum spanwise distribution of the airfoil geometry between the forward-swept and backward-swept wings. For the GA-based optimizer, a new multi-fidelity approach integrated with a multi-additional sampling concept and a multi-objective multi-fidelity efficient global optimization was developed and applied to solve these design problems to reduce the calculation time when optimizing samples.

4.2 Evaluation Method of Aerodynamics and Sonic Boom

4.2.1 Overview

A Mach 1.4 supersonic cruise at an altitude of 45,000 ft (13,716 m) was assumed as the freestream condition. Through aerodynamic evaluation, the pressure drag coefficient C_{DP} of the aircraft and the pressure distribution near the aircraft were determined under two constraints (considered to ensure level flight) as follows:

$$L = W$$

$$X_{CP} = X_{CG}$$

These two constraints are the same as those in the analysis in Chapter 2. The flow chart of the

aerodynamic evaluation is shown in Figure 4-1. Initially, to calculate the trimmed angle of the horizontal tail wing, the potential equation was solved for two configurations with different angle horizontal tails. After the trimmed angle of the horizontal tail wing was calculated, the Euler equation was applied for the trimmed configuration. Thus, the C_{DP} and the pressure distribution around the aircraft was obtained. Multipole analysis was applied to the pressure distribution around the aircraft. Subsequently, the augmented Burgers equation was solved to obtain the sonic boom signature on the ground and its amplitude.

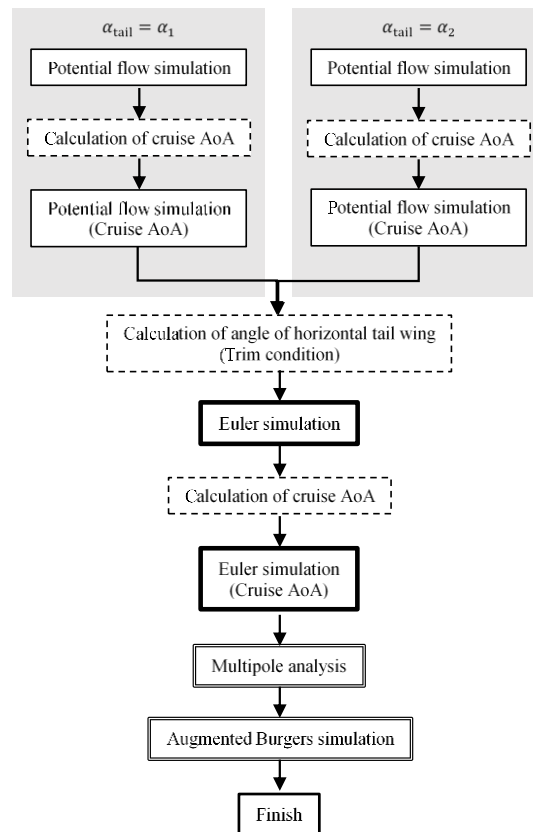


Figure 4-1 Flowchart of the numerical evaluation.

4.2.2 Aerodynamic Evaluation

The calculation method used to satisfy the trim constraint and estimate C_{DP} as the low-fidelity evaluation that is carried out in Section 4.4 solves the potential equation with the panel method

already described in Section 2.4. Calculations based on the potential equation were performed to evaluate the configuration in which the engine intake and nacelle were not present. At the trimmed condition, the Euler equation was solved, which is the same method as that described in Section 3.4.1.

4.2.3 Sonic Boom Evaluation

The strength of a sonic boom with a finite-thickness shock wave and pressure signature on the ground were obtained by solving the augmented Burgers equation after applying multipole analysis to the pressure distribution near the aircraft (based on the Euler simulation). In multipole analysis [2], near-field pressure signatures are modified to attenuate only in the circumferential direction, which is available by introducing the distributions of multipoles. Thus, a far-field pressure signature becomes independent of the location where the initial condition is obtained. In this process, MPnoise [4], a multipole analysis tool developed by JAXA, was used.

The augmented Burgers equation [3] is expressed in Eq. (4-1). In the Burgers equation, the gradient of the pressure difference along the ray [the left member of Eq. (4-1)] equals the summation of the non-linearity of the sound wave's finite amplitude (the first term of the left member) and the attenuation effect of the heat viscosity of atmosphere (the second term of the left member). In this equation, B is expressed in Eq. (4-2). $V(s)$ denotes Blokhintsev invariant, which is known that it is conserved along a ray tube in atmosphere flowing wind in liner case. In the augmented Burgers equation, the stratification effect of the atmosphere [Eq. (4-3)], the geometric expansion effect of the Mach cone [(Eq. (4-4)] and the attenuation effect of the vibrational relaxation of atmospheric molecules [Eq. (4-5)] are considered in addition to the Burgers equation.

$$\frac{\partial p}{\partial s} = \frac{\gamma + 1}{2} \frac{1}{2\rho_0 c_0^3} \frac{\partial p^2}{\partial \tau} - \frac{1}{2B} \frac{\partial B}{\partial s} p + a_{\text{ABeq}} + b_{\text{ABeq}} + c_{\text{ABeq}} \quad (4-1)$$

$$B = \frac{V(s)}{p^2} \quad (4-2)$$

$$a_{\text{ABeq}} = \frac{1}{2\rho_0 c_0} \frac{\partial(\rho_0 c_0)}{\partial s} \quad (4-3)$$

$$b_{\text{ABeq}} = \frac{\delta}{2c_0^3} \frac{\partial^2 p}{\partial \tau^2} \quad (4-4)$$

$$c_{\text{ABeq}} = \sum_{\nu} \frac{(\Delta c)_{\nu} \tau_{\nu}}{c_0^2} \left(1 + \tau_{\nu} \frac{\partial}{\partial \tau}\right)^{-1} \frac{\partial^2 p}{\partial \tau^2} \quad (4-5)$$

In this process, Xnoise [4], a far-field signature prediction tool developed by JAXA, was used. As a measure of the sonic boom strength, the perceived level (PL) [5] was used in this study. The PL was estimated using BoomMeter [4], a frequency analysis software developed by JAXA for sonic booms.

4.2.4 Validation of Grid Dependency

4.2.4.1 Standard Richardson Extrapolation (SRE)

The standard Richardson extrapolation (SRE) [6] was performed to confirm the validation of the calculation grids. In the SRE, the approximate solution f_{SRE} , when the distance between grids approaches zero, can be estimated using two different calculation grids the fine and the coarse. The total number of fine grids is larger than that of the coarse grids. The approximate solution f_{SRE} can be expressed as follows:

$$f_{\text{SRE}} = f_{\text{fine}} + \frac{f_{\text{fine}} - f_{\text{coarse}}}{3} \quad (4-6)$$

where f_{fine} and f_{coarse} are the solutions of the fine and the coarse grids, respectively. In this

study, the baseline configuration was used to calculate grid validation. The number of fine grids, which had a refinement box around the aircraft, was approximately 65 million, and that of the coarse grids, which did not have the refinement box, was approximately 9.5 million.

4.2.4.2 Results

The grid dependency for aerodynamic evaluation is shown in Figure 4-2. Focusing on C_{DP} , the difference between the coarse grid and the SRE result and the difference between the fine grid and the SRE result were within one drag count. Thus, the coarse grid facilitates a reasonable evaluation of C_{DP} performance. However, focusing on the PL of the sonic boom on the ground, a different trend can be observed. The difference between the fine grid and the SRE result was approximately 0.25 PLdB, whereas the difference between the coarse grid and the SRE result was more than 1.0 PLdB. Therefore, the fine grid was used for C_{DP} and PL evaluations in the following sections.

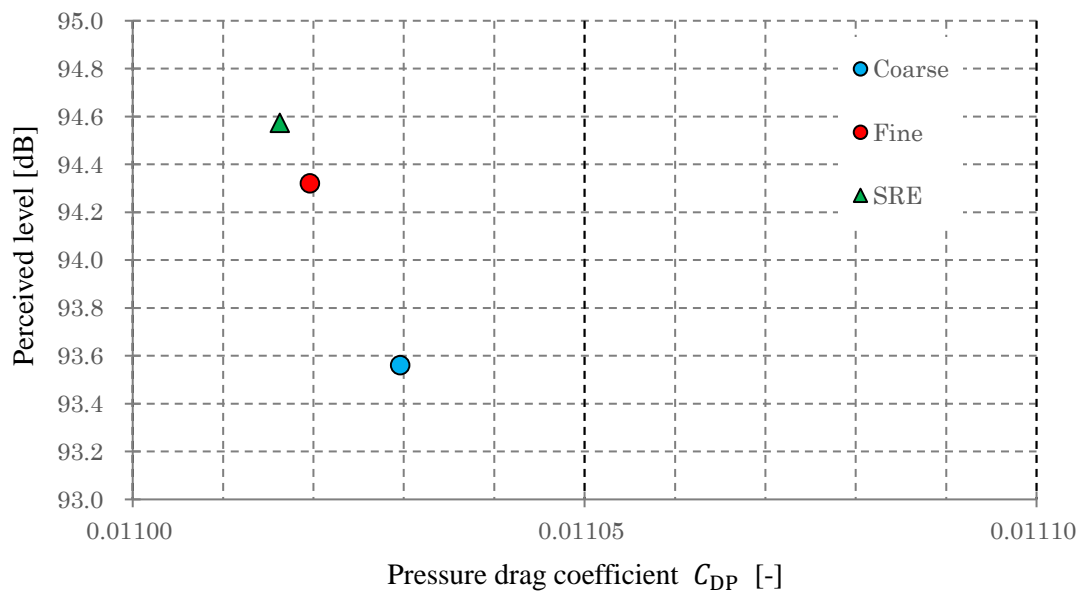


Figure 4-2 Calculation results of the grid validation.

4.3 Parametric Study of Aerodynamic Performance of a Forward-Swept Wing

4.3.1 Specifications of Target Aircrafts

In this study, an SSBJ concept model (Figure 4-3) [7] developed by JAXA, was defined as the baseline configuration. The baseline configuration consisted of a wing, fuselage, horizontal tail wing, vertical tail wing, and engine (engine intake and flow-through nacelle). Thirteen designs in which the backward-swept angle Λ of the outboard wing was changed are shown in Figure 4-4. All components except the outboard wing had the same configuration for each design in order to focus on the sensitivity of the aerodynamic performance by changing the wing planform. The specifications of the wing planform for each configuration and the airfoil geometries at the representative baseline positions are shown in Table 4-1 and Figure 4-5, respectively. The positions of the center of gravity and the aerodynamic center of each configuration are shown in Table 4-2 and plotted in Figure 4-4(b). Although the weight of a forward-swept wing is said to be heavy when using conventional metallic material, we can expect to realize a practical weight if a composite material and an aeroelastic tailoring technology [8, 9] are applied. Thus, investigating whether these forward-swept wing configurations are effective in low-boom design can be valuable for future SST design.

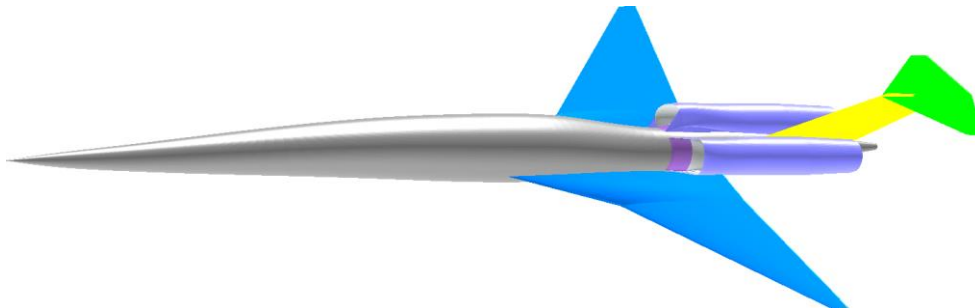


Figure 4-3 Baseline configuration.

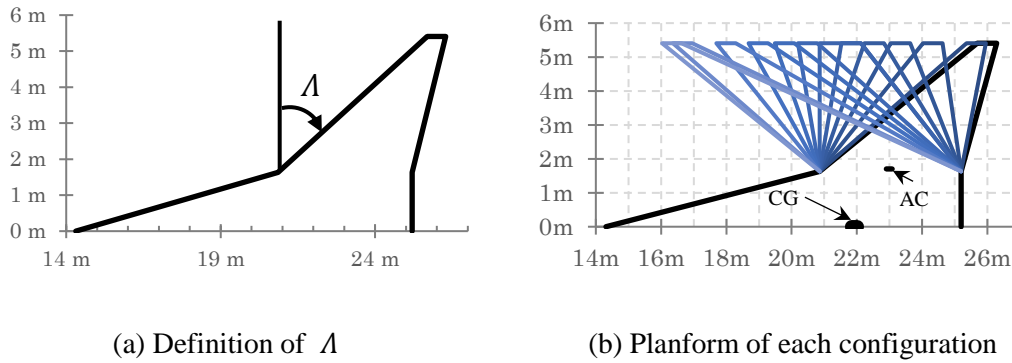


Figure 4-4 Overview of the evaluated wing planforms.

Table 4-1 Specifications of wing planforms for the evaluated aircrafts.

Wing area	45.3 m ²	
Aspect ratio	2.6	
Leading backward-swept angle	Inboard wing	76°
	Outboard wing	52°, 50°, 40°, 30°, 20°, 10°, 0°, -10°, -20°, -30°, -40°, -50°, -52°
Taper ratio	Inboard wing	0.40
	Outboard wing	0.14
Kink position	30.2 % semi-span	

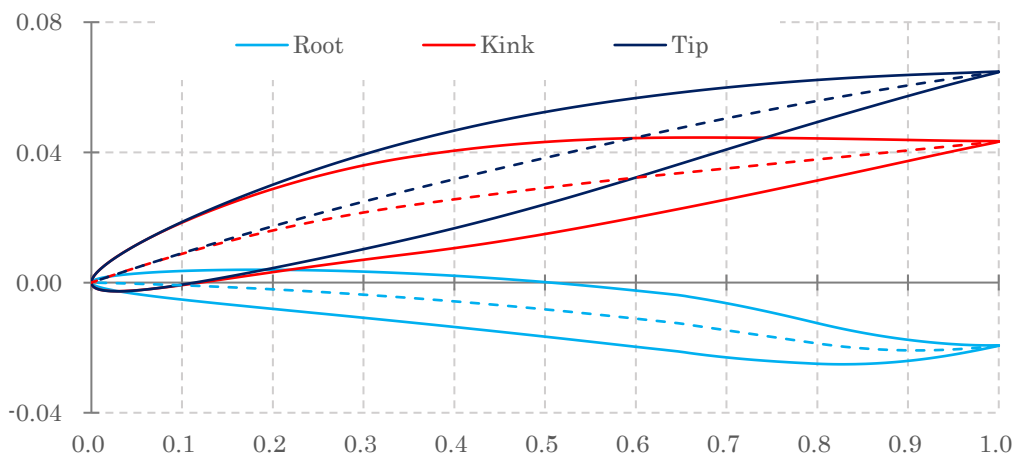


Figure 4-5 Airfoil geometries of the baseline.

Table 4-2 Positions of the center of gravity and the aerodynamic center for each configuration.

Λ	CG	AC	Λ	CG	AC
52°	22.01 m	23.08 m	-10°	21.91 m	22.98 m
50°	22.01 m	23.07 m	-20°	21.90 m	22.97 m
40°	21.98 m	23.05 m	-30°	21.89 m	22.95 m
30°	21.97 m	23.03 m	-40°	21.87 m	22.93 m
20°	21.95 m	23.02 m	-50°	21.84 m	22.91 m
10°	21.94 m	23.00 m	-52°	21.84 m	22.90 m
0°	21.93 m	22.99 m			

4.3.2 Results and Discussion

4.3.2.1 Comparisons between Backward- and Forward- Swept Wings

Figure 4-6 shows the relation between the pressure drag coefficient C_{DP} and the PL for each design. Each blue Λ plot indicates forward-swept wing designs and red indicates backward-swept wing designs. The calculation result of each design was obtained in the direction of the arrow colored with the Λ values. In other words, when the value of Λ decreases, the C_{DP} and PL values increase up to certain values. After that, the C_{DP} and PL values decrease. Therefore, we can say that selecting forward-swept wing planforms for wing design is an effective option for simultaneously minimizing C_{DP} and PL values at supersonic cruise. The PL value of the forward-swept wing was lower than that of the backward-swept wing and the maximum PL difference between them was approximately 4.8 PLdB. Specifically, diminution of the PL was predominantly observed at $30^\circ \leq \Lambda \leq 10^\circ$.

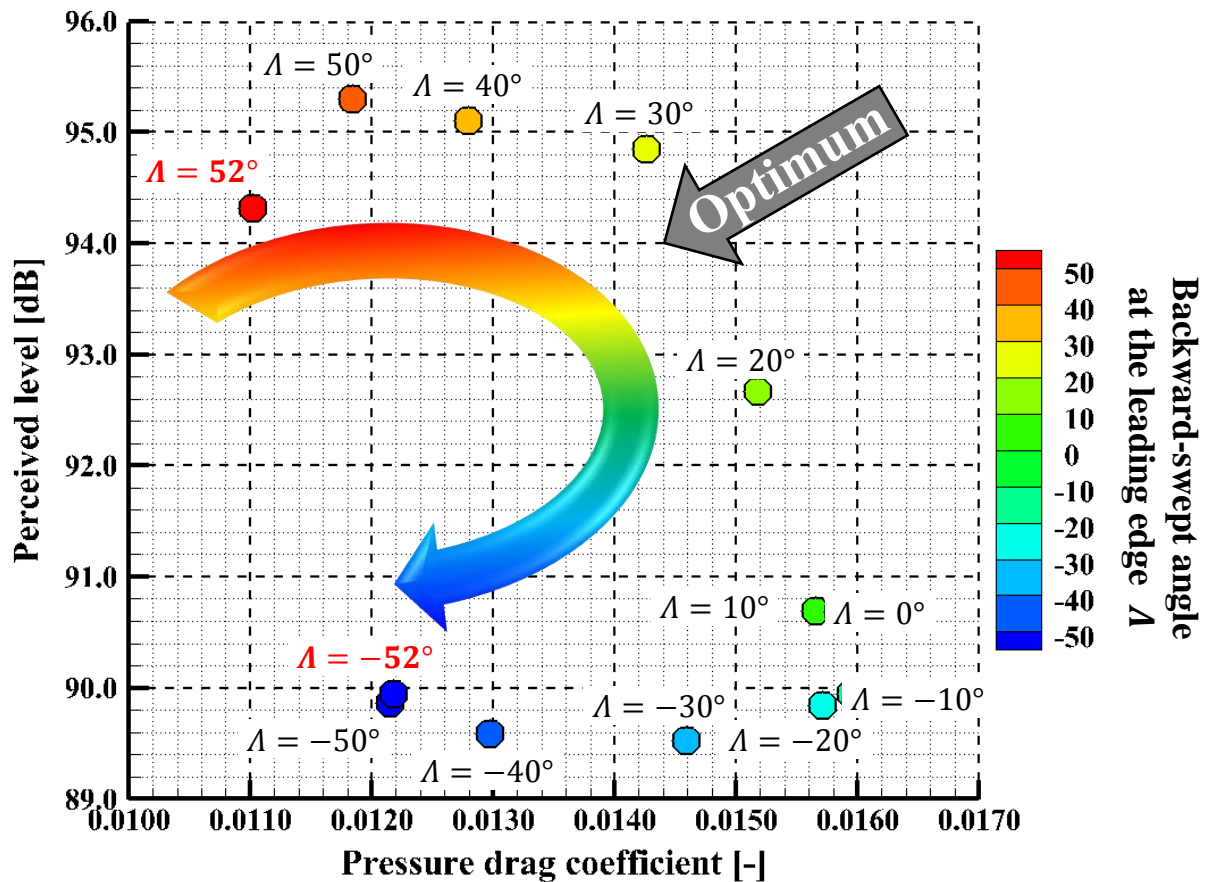


Figure 4-6 Evaluation results of each solution.

4.3.2.2 Comparisons of Pressure Fields

To discuss the change in the pressure signature of the sonic boom with a forward shift in lift distribution, the pressure signatures at the nearfield of the aircraft and the ground for the $\Lambda = 52^\circ$ configuration (the baseline with a backward-swept wing) and the $\Lambda = -52^\circ$ configuration (the baseline with a forward-swept wing) are shown in Figure 4-7. In addition, the pressure signatures during the process of ground propagation, the lift distributions of the aircraft along the body axis, and the surface C_p distributions are shown in Figure 4-8, Figure 4-9, and Figure 4-10, respectively. The lateral axes of Figure 4-7 (b) and Figure 4-8 denote the time when the sonic boom was heard. In Figure 4-7(a), pressure fluctuation up to 14 m occurred at the nose of the aircraft.

Chapter 4

In general, the pressure signature of the sonic boom on the ground is known to become N-shaped when an object flies at supersonic speed at high altitude. In this study, the positive peak of the pressure signature caused by the first pressure increase is called the “leading boom”. Additionally, the negative peak of the pressure signature caused by the pressure depletion after the leading boom is called the “trailing boom”.

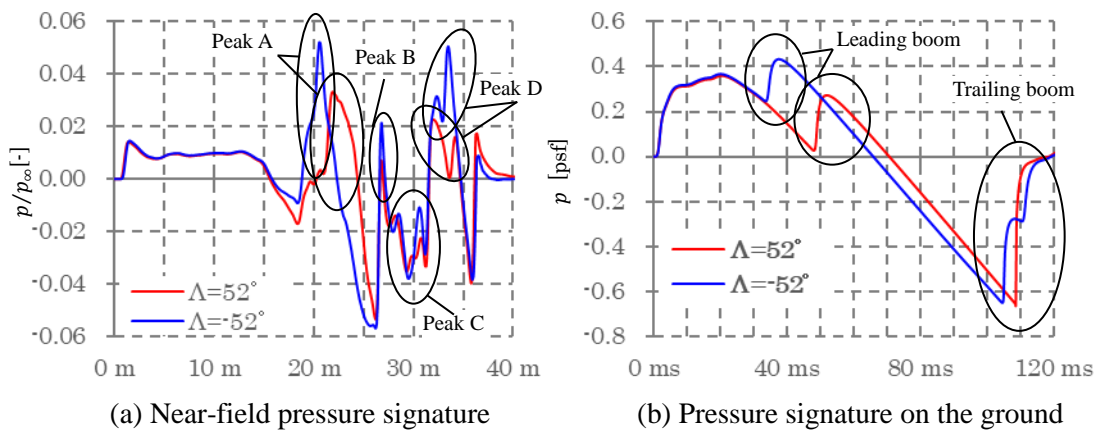
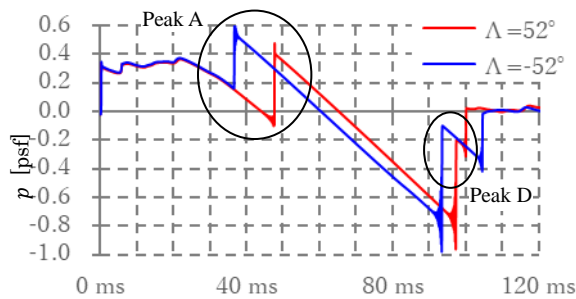
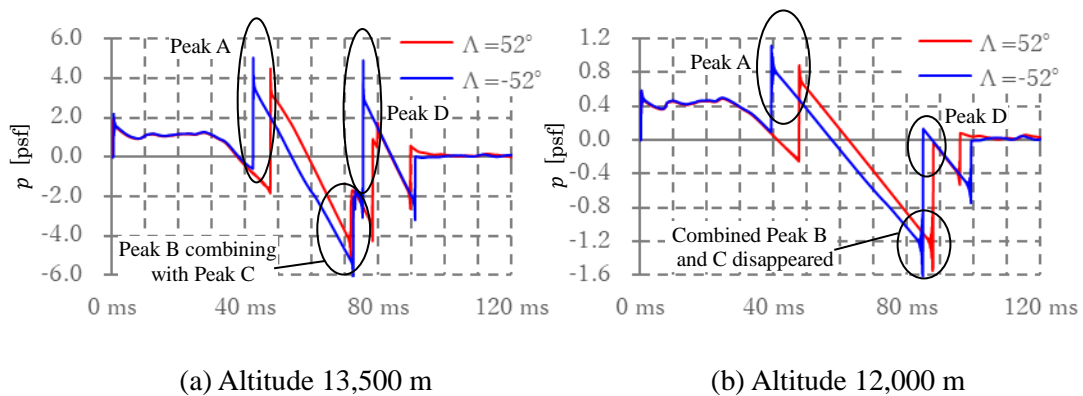


Figure 4-7 Pressure signatures at the near-field of the aircraft and the ground.



(c) Altitude 9,000 m

Figure 4-8 Pressure signatures during the process of propagating to the ground.

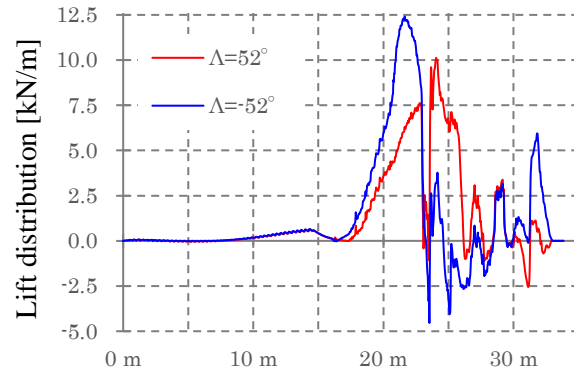


Figure 4-9 Lift distributions of the aircraft along the body axis.

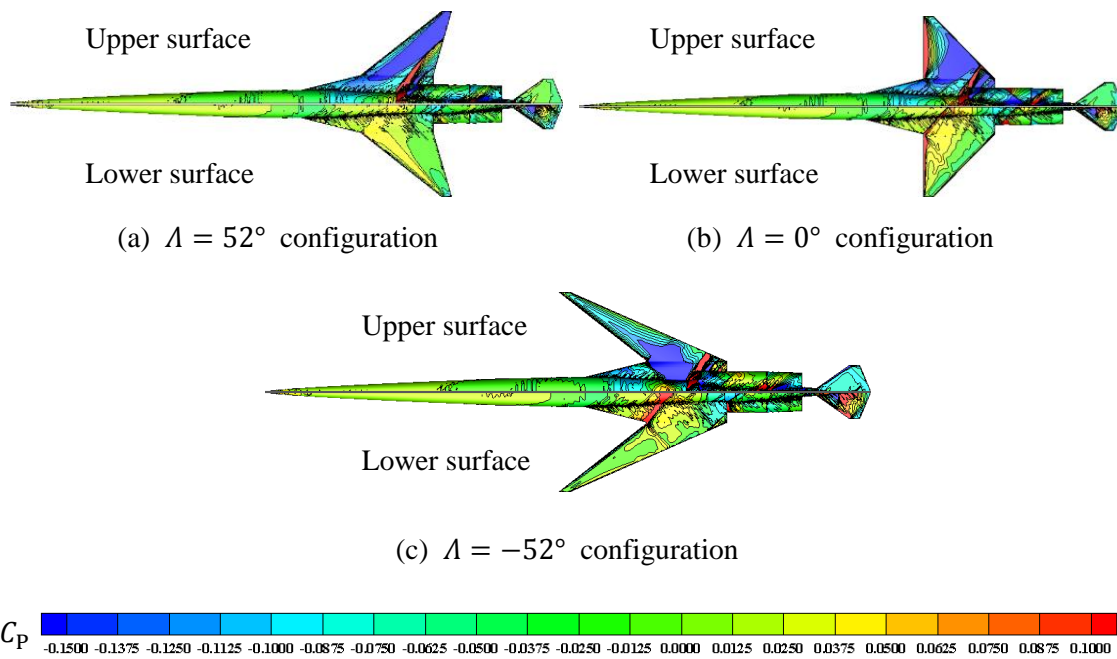


Figure 4-10 Surface C_p distribution for representative configurations.

4.3.2.2.1 Leading boom

According to Figure 4-8, the leading boom observed in Figure 4-7(a) was clearly propagated from Peak A. Peak A of the $\Lambda = -52^\circ$ configuration was preceded by that of the $\Lambda = 52^\circ$ configuration. This time difference was attributed to the difference in the peaks of the lift distribution. Figure 4-9 shows that the peaks of the $\Lambda = -52^\circ$ and $\Lambda = 52^\circ$ configurations were located at approximately 22 m and 24 m, respectively. When focusing on the amplitude of Peak A, the peak value of the $\Lambda = -52^\circ$ configuration was larger than that of the $\Lambda = 52^\circ$ configuration. In Figure 4-10(c), a high-pressure region can be observed on the wing's upper surface from the leading edge of the kink to the inboard trailing edge. This high-pressure region can also be observed in the $\Lambda = 0^\circ$ configuration; however, the increase in pressure of the $\Lambda = 0^\circ$ configuration was lower than that of the $\Lambda = -52^\circ$ configuration. In addition, these high-pressure regions were not observed in the $\Lambda = 52^\circ$ configuration. Thus, the difference in the amplitude of Peak A between each configuration resulted from these high-pressure regions. If we design forward-swept wings to avoid developing these high-pressure regions, greater reduction of C_{DP} and PL can be expected.

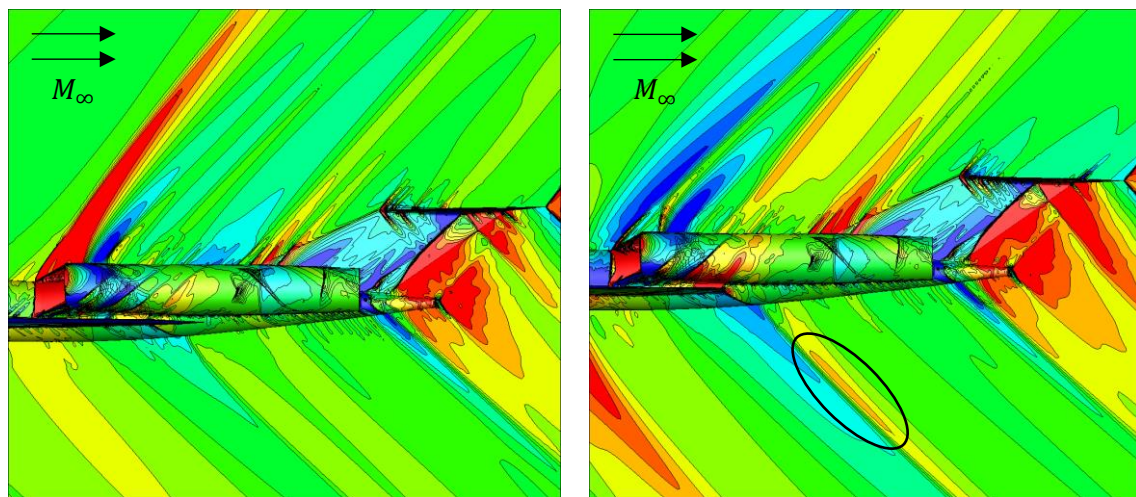
4.3.2.2.2 Trailing boom

According to Figure 4-8, Peaks B, C, and D in Figure 4-7(a) merged before reaching the ground and were observed as a trailing boom on the ground. This was cited as a factor that caused the PL of the $\Lambda = -52^\circ$ configuration to be lower than that of the $\Lambda = 52^\circ$ configuration, and a stepwise pattern for the rising part of the trailing boom for the $\Lambda = -52^\circ$ configuration. As periodic pressure alterations cause sound, the sound pressure level would also decrease if the time rate of the pressure change decreases.

According to Figure 2-7(a), Peaks B of both the $\Lambda = 52^\circ$ and $\Lambda = -52^\circ$ configurations were observed at the same time. The peak value of the latter was larger than that of the former. The lift distribution described in Figure 4-9 shows that lift recovery can be observed at approximately 23.4 m in both configurations and it may affect the difference in the pressure signatures. The entry of the air intake was located at approximately 23.4 m, where Peak B was observed. The surface C_p distribution on the aft body and the cross-sectional C_p distribution are shown in Figure 4-11. Here, a shock wave was observed, and it affected the lift distributions; the pressure signature of the sonic boom was subsequently changed. In Figure 4-11, the pressure increased between the engine nacelle and the wing in the $\Lambda = -52^\circ$ configuration. This pressure increase resulted from a compression wave in the $\Lambda = -52^\circ$ configuration, which is marked in black in Figure 4-11(b); this compression wave was not observed in the $\Lambda = 52^\circ$ configuration. The values of Peaks B and C of the $\Lambda = -52^\circ$ configuration were higher than those of the $\Lambda = 52^\circ$ configuration because of this pressure increase. Although these differences in Peaks B and C between two configurations can be observed, Peaks B and C had already disappeared on the ground after they were merged in both configurations. This is the reason that Peaks B and C were weaker than Peaks A and D.

Peak D had two peaks, which were caused by the trailing edge of the fuselage and the horizontal tail wing, respectively. The second peak of Peak D of the $\Lambda = -52^\circ$ configuration was stronger than that of the $\Lambda = 52^\circ$ configuration. The angle of attack (AoA) of the horizontal tail wing [the summation of the AoA of the cruising aircraft and the elevator (all-flying tail) angle] and the lift coefficients of the wing and the horizontal tail wing are shown in Table 4-3 and Table 4-4, respectively. These tables reveal that the AoA of the horizontal tail wing increased, and the lift of the horizontal tail wing became stronger when the Λ value decreased. The AoA of the horizontal tail wing of the $\Lambda = -52^\circ$ configuration was approximately 3° larger than that of the $\Lambda = 52^\circ$

configuration. This is the reason more lift at the horizontal tail wing was required in the forward-swept wing than in the backward-swept wing to balance the forward-shifted lift distribution at the wing. Thus, the lift coefficient of the forward-swept wing was lower than that of the backward-swept wing. The pressure increase at the trailing edge of the horizontal tail wing of the $\Lambda = -52^\circ$ configuration because of a shock wave was stronger than that of the $\Lambda = 52^\circ$ configuration, and it could be observed in the pressure signature at the near-field at the aircraft (Figure 4-11). In Figure 4-8, Peak D of the $\Lambda = 52^\circ$ configuration was damped and disappeared until the ground was reached. In contrast, Peak D of the $\Lambda = -52^\circ$ configuration remained on the ground. This was why the trailing boom of the $\Lambda = 52^\circ$ configuration formed a stepwise pattern. Thus, the key to forming a stepwise pattern peak to the Real boom was balancing the lifts of the wing and the horizontal tail wing.



(a) $\Lambda = 52^\circ$ configuration

(b) $\Lambda = -52^\circ$ configuration

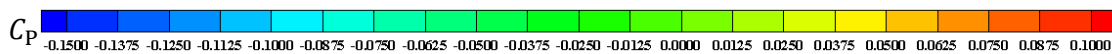


Figure 4-11 Surface C_p distribution on the aft body and cross-sectional C_p distribution.

Table 4-3 AoA of the horizontal tail wing for each configuration.

Λ	Cruising AoA	Elevator angle	AoA of the horizontal tail wing
52°	3.07°	-1.28°	1.79°
50°	3.30°	-3.34°	-0.04°
40°	3.05°	-0.49°	2.56°
30°	3.07°	-0.15°	2.92°
20°	3.09°	0.03°	3.12°
10°	3.10°	0.14°	3.24°
0°	3.13°	0.10°	3.23°
-10°	3.12°	0.32°	3.44°
-20°	3.13°	0.47°	3.60°
-30°	3.17°	0.71°	3.88°
-40°	3.27°	0.97°	4.24°
-50°	3.38°	1.35°	4.73°
-52°	3.40°	1.43°	4.83°

Table 4-4 Lift coefficients of each component.

Λ	Wing	Horizontal tail wing	The others
52°	0.0981	-0.0019	0.0238
50°	0.1099	-0.0156	0.0261
40°	0.0935	0.0023	0.0244
30°	0.0911	0.0043	0.0246
20°	0.0898	0.0053	0.0246
10°	0.0893	0.0058	0.0247
0°	0.0901	0.0052	0.0249
-10°	0.0890	0.0064	0.0245
-20°	0.0890	0.0072	0.0241
-30°	0.0869	0.0091	0.0240
-40°	0.0838	0.0119	0.0244
-50°	0.0802	0.0156	0.0245
-52°	0.0795	0.0164	0.0242

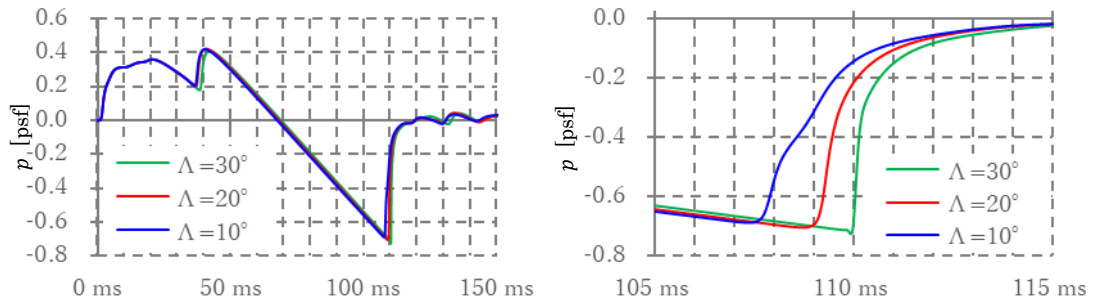
4.3.2.2.3 $\Lambda = 30^\circ, 20^\circ$, and 10° configurations

Figure 4-6 shows that the decrease of the PL was remarkable at $30^\circ \leq \Lambda \leq 10^\circ$. These pressure signatures are shown in Figure 4-12. No difference of pressure signature is observed in Figure 4-12 (a) until approximately 30 ms because of the increased pressure at the nose between each configuration. In general, downstream information cannot be transferred upstream in supersonic flow, in contrast to subsonic flow. Therefore, the pressure fluctuation around the wing did not involve the pressure signature at the front of the wing. Consequently, each pressure signature of the nose part became similar. A magnified figure of trailing boom is shown in Figure

4-12(b). To discuss details of the pressure signature features, a second-order differential of pressure was calculated and plotted, and the results are shown in Figure 4-12(c). In the $\Lambda = 30^\circ$ and $\Lambda = 20^\circ$ configurations, after the pressure signature at trailing boom recovered from the negative peak, the recovery was gradual and converged to zero. The $\Lambda = 10^\circ$ and $\Lambda = 20^\circ$ configurations both had pressure signatures recovering from their respective peaks at approximately 107.6 ms and the recovery became gradual, whereas pressure recovery became gradual at approximately 109 ms; subsequently, it intensified in the $\Lambda = 10^\circ$ configuration. In this time, as shown in the black circled area in Figure 4-12(c), the second-order differential of the pressure signature changed from negative to positive and then back to negative. This behavior of the second-order differential of pressure signature was not observed in the $\Lambda = 30^\circ$ and $\Lambda = 20^\circ$ configurations. In general, when the second-order differential of a function becomes sequentially negative, positive, and negative, the function can be described as a curved line, as shown in Figure 4-13. This behavior of the second-order differential of the pressure signature suggested a predictor to form a stepwise signature pattern. Considering the large difference in PL values between the $\Lambda = 10^\circ$ and $\Lambda = 20^\circ$ configurations, a pressure signature with an inflection point as in Figure 4-13 is effective for reducing the PL. Thus, design guidelines that catch this predictor are required to reduce the PL. Trailing pressure signatures at the ground of configurations with $\Lambda \leq 10^\circ$ are shown in Figure 4-14. According to this figure, the pressure signatures of all configurations in which Λ was smaller than 10° formed stepwise patterns. If the Λ value decreases, stepwise patterns of the pressure signature will become more remarkable.

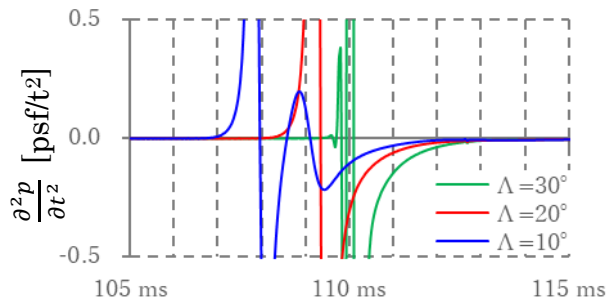
When the forward-swept angle increased with $\Lambda = 30^\circ, 20^\circ,$ and 10° , the lift of the horizontal tail wing increased to satisfy the trim condition, as shown in Table 4-3. This increase in the lift of the horizontal tail wing caused a pressure increase at the horizontal tail wing. In the $\Lambda > 20^\circ$ configurations, the peak caused by the pressure increase of the horizontal tail wing disappeared

until the sonic boom reached the ground. However, in the $\Lambda = 10^\circ$ configuration, the peak had already remained on the ground, and the trailing boom followed a stepwise pattern, and the PL significantly decreased than the $\Lambda = 20^\circ$ configuration. This result suggests that selecting forward-swept or low backward-swept wings with a low backward-swept angle is an effective solution for achieving a stepwise-patterned trailing boom to reduce the PL value. In addition, as an effective way to lift the distribution shifts forward, the mounting position of the backward-swept wing can be said to shift forward. However, if a backward-swept wing is mounted on the front of the fuselage, the horizontal-tail wing tail volume will increase and the aircraft will become over-stable. Additionally, the constructional material of the wing interferes with the thin nose and may compress the cabin. From this aspect, a forward-swept wing design can situate the fuselage further back than a backward-swept wing design. Therefore, a forward-swept wing enables flexibility in the contractual design unless the horizontal tail wing tail volume is changed.



(a) Pressure signature on the ground

(b) Magnified figure of the Trailing boom



(c) The second-order differential of pressure signature

Figure 4-12 Pressure signature at the ground for $\Lambda = 30^\circ, 20^\circ$, and 10° configurations.

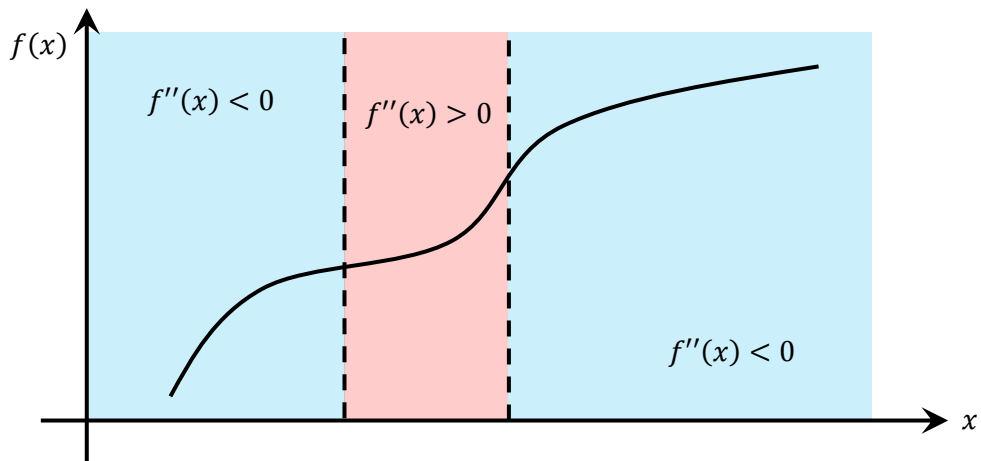


Figure 4-13 Function curve in which the second order differential takes negative, positive, and negative values in sequence.

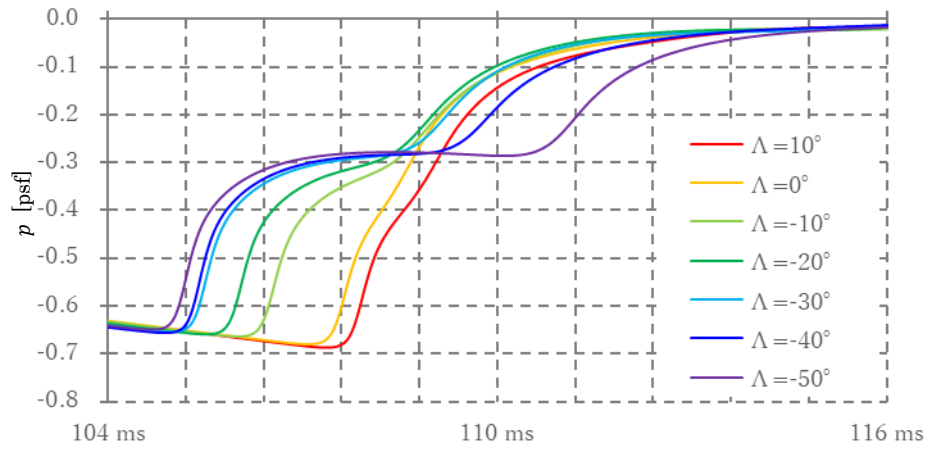


Figure 4-14 Trailing pressure signatures on the ground of configurations ($\Lambda \leq 10^\circ$).

4.4 Low-Drag Low-Boom Wing Design

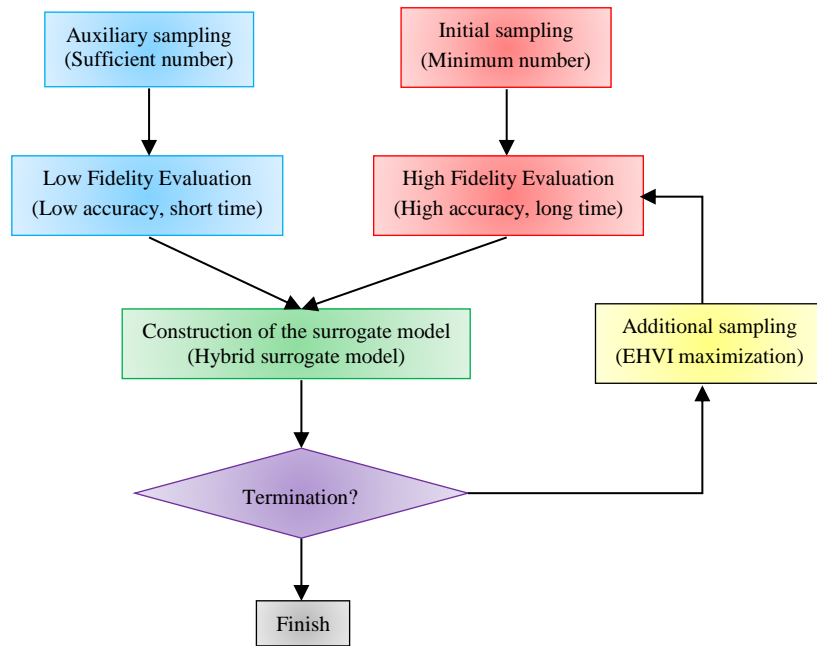
4.4.1 Design Method

4.4.1.1 Multi-objective Multi-fidelity Optimization with Multi-additional Sampling

4.4.1.1.1 Overview

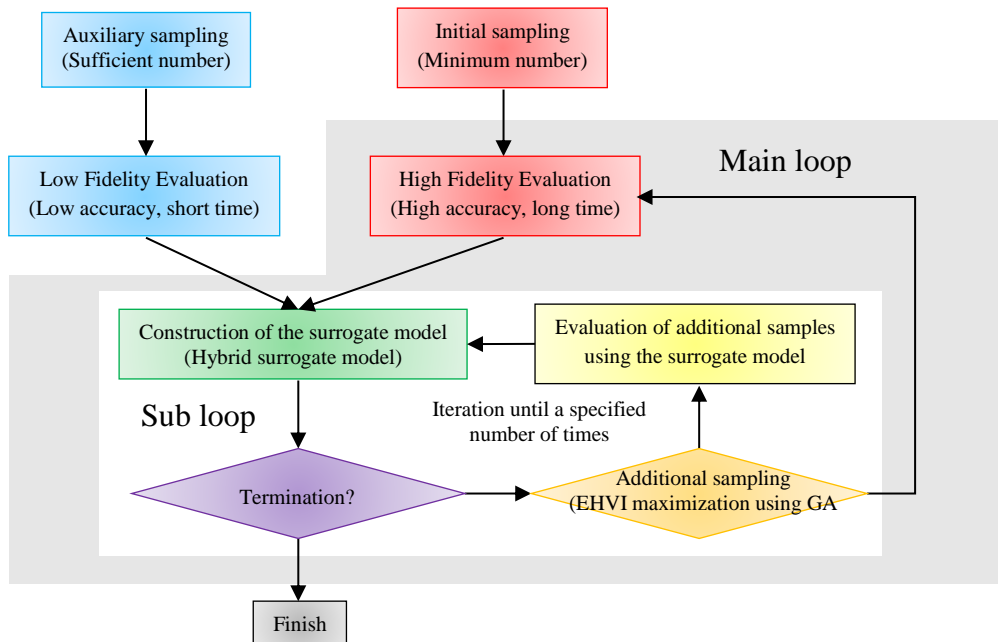
Figure 5-15 shows flow charts of multi-objective multi-fidelity optimization methods. The method described in Figure 4-15(a) was extended from the multi-fidelity global optimization method described in Section 3.2.1 to solve a multi-objective optimization problem. In the optimal search process, NSGA-II was applied to solve the maximization problem in which the expected hyper-volume improvement (EHVI) value [10] was used instead of EI. The selection, crossover, and mutation processes are described in Section 3.2.3. Considering a parallel calculation environment such as a high-fidelity evaluation process using a supercomputer, the fact that only one sample can be evaluated with high-fidelity evaluation per loop of additional sampling is not efficient.

Thus, to make the most of the advantages of a parallel calculation environment, a new design method was developed, in which a multi-additional sampling concept was adopted [Figure 4-15(b)] for a multi-fidelity efficient global optimization of the multi-objective optimization problem. This proposed approach is a sub loop that includes the conventional method. After the first optimal search, the maximum EHVI solution was searched and selected for the additional sample. This solution was not evaluated with the high-fidelity model but with the surrogate model in the proposed approach. Subsequently, the surrogate model was reconstructed and added to the result of the evaluation for the new solution. After iterating this sub loop a specified number of times, additional samples were evaluated using the high-fidelity model and the surrogate model was reconstructed using these results.



(a) Multi-fidelity efficient global optimization for the multi-objective optimization problem

(Present optimization approach)



(b) Proposed method

Figure 4-15 Flow chart of multi-objective multi-fidelity optimization methods.

4.4.1.1.2 Demonstration of Proposed Approach Using a Test Problem

Before applying the proposed approach to an aircraft design problem, a mathematical test problem was solved using both the proposed approach and conventional multi-fidelity efficient global optimization for the multi-objective optimization problem to validate the optimization performance of the proposed approach.

MOP2 in Van Valedhuizen's test suite (Fonseca and Fleming function) [11] was used for the test function. This function is a two-objective minimization problem and the objective functions are expressed as follows:

$$f_{\text{MOP2}_1}(\mathbf{x}_{\text{dv}}) = 1 - \exp \left[- \sum_{i=1}^m \left(x_{\text{dv}_i} - \frac{1}{\sqrt{m}} \right)^2 \right] \quad (4-7)$$

$$f_{\text{MOP2}_2}(\mathbf{x}_{\text{dv}}) = 1 - \exp \left[- \sum_{i=1}^m \left(x_{\text{dv}_i} + \frac{1}{\sqrt{m}} \right)^2 \right] \quad (4-8)$$

where $-4 \leq x_{\text{dv}_i} \leq 4$

The exact solutions (Pareto solutions) are expressed as follows:

$$f_{\text{MOP2}_2} = 1 - \exp \left[- \left\{ 2 - \sqrt{-\ln(1 - f_{\text{MOP2}_1})} \right\}^2 \right] \quad (0 \leq f_{\text{MOP2}_1} \leq 1 - e^{-4}) \quad (4-9)$$

where $x_{\text{dv}_i} = \left[-\frac{1}{m}, \frac{1}{m} \right]$

The low-fidelity model in Eqs. (4-7) and (4-8) can be expressed as follows:

$$f_{\text{MOP2}_1}(\mathbf{x}_{\text{dv}})|_{\text{Low}} = 1 - \exp \left[- \sum_{i=1}^m \left(0.5x_{\text{dv}_i} - 0.05 - \frac{1}{\sqrt{m}} \right)^2 \right] \quad (4-10)$$

$$f_{\text{MOP2}_2}(\mathbf{x}_{\text{dv}})|_{\text{Low}} = 1 - \exp \left[- \sum_{i=1}^m \left(0.75x_{\text{dv}_i} + 0.2 + \frac{1}{\sqrt{m}} \right)^2 \right] \quad (4-11)$$

Hereafter, m , which is the number of design variables, was assumed to be five. An example of the distribution of random solutions is shown in Figure 4-16. According to this figure, the difference in the Pareto front between the high-fidelity and the low-fidelity models increased near the center value of f_{MOP2_1} .

The optimization conditions are summarized in Table 4-5. In this validation, the main loop was iterated until 50 additional samples were obtained. The additional sampling results are shown in Figure 4-17. In this figure, several additional samples on the theoretical Pareto front were obtained for Cases 1 and 2 as the present optimization method. To compare the accuracy of the surrogate model between Case 1 and Case 2, the LOOCV result is shown in Figure 4-18. Based on this figure, it can be said that both Case 1 and Case 2 are accurate surrogate models. However, the number of Case 1 solutions on the theoretical Pareto front was larger than that of Case 2, which might be because the number of times the surrogate model was updated based on the high-fidelity evaluation of Case 1 was larger than that of Case 2. Therefore, the number of iterations of the main and sub loops should consider the high-fidelity evaluation time.

When a parallel calculation for sample evaluation is available, the evaluation time using the high-fidelity model per additional sampling would be almost the same for both proposed and present optimization approaches. Thus, when actually considering a solution to the design problem, a comparison between the proposed approaches and the present optimization approach matching the number of iterations of the main loop is required. Additional sampling results when the number of main loop iterations was matched in each case are shown in Figure 4-19. In this figure, few additional samples of the present optimization approach are located on the theoretical

Pareto front while several additional samples of Cases 1 and 2 are located on the theoretical Pareto front. It is evidently easier to obtain solutions near the theoretical Pareto front using the proposed approach than the present optimization approach when the number of the main loops is same in both methods. Considering the diversity of non-dominated solutions, the hypervolume history is shown in Figure 4-20. According to this figure, it is obvious that if the number of sub loop iterations (the number of additional samples per one additional sampling) increases, the hypervolume will also increase rapidly.

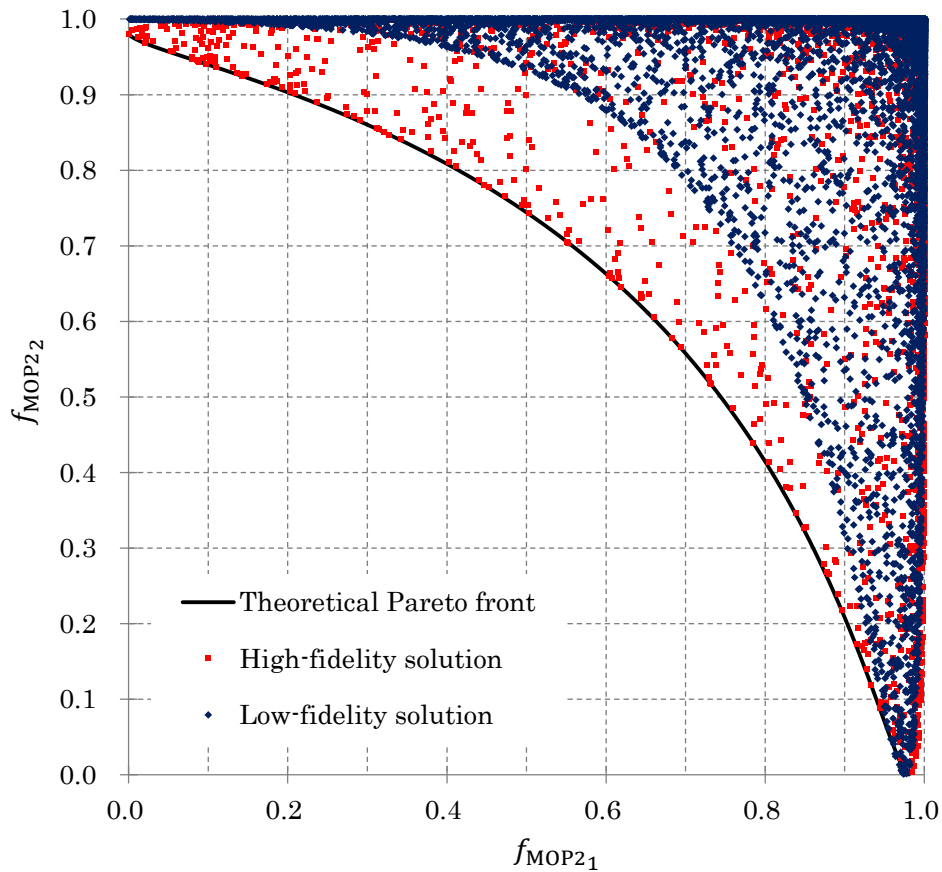


Figure 4-16 Example of distribution of random solutions ($m = 5$).

Table 4-5 Optimization conditions.

Case name	Case 1	Case 2	Present optimization approach
Total generation	50		
Population	20		
Number of initial samples	20		
Number of auxiliary samples	50		
Number of iterations of main loop	25	10	50
Number of iterations of sub loop	2	5	0

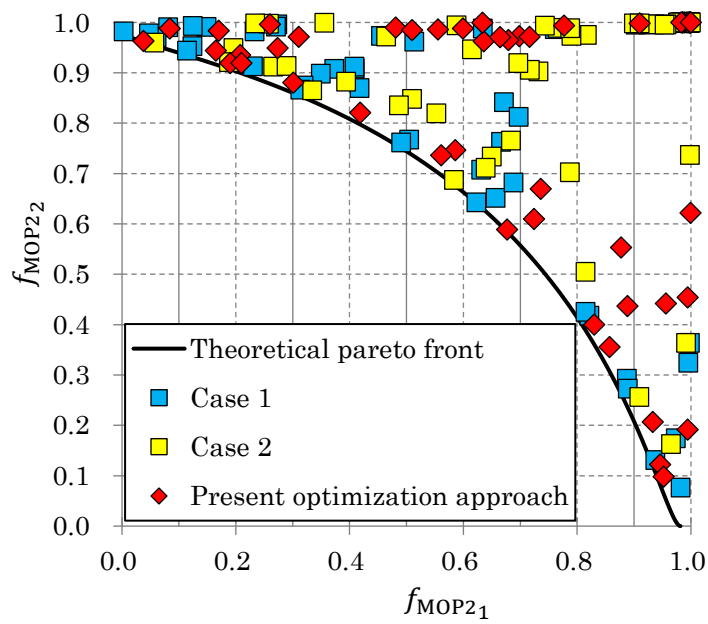


Figure 4-17 Additional sampling result for each case when 50 additional samples were obtained.

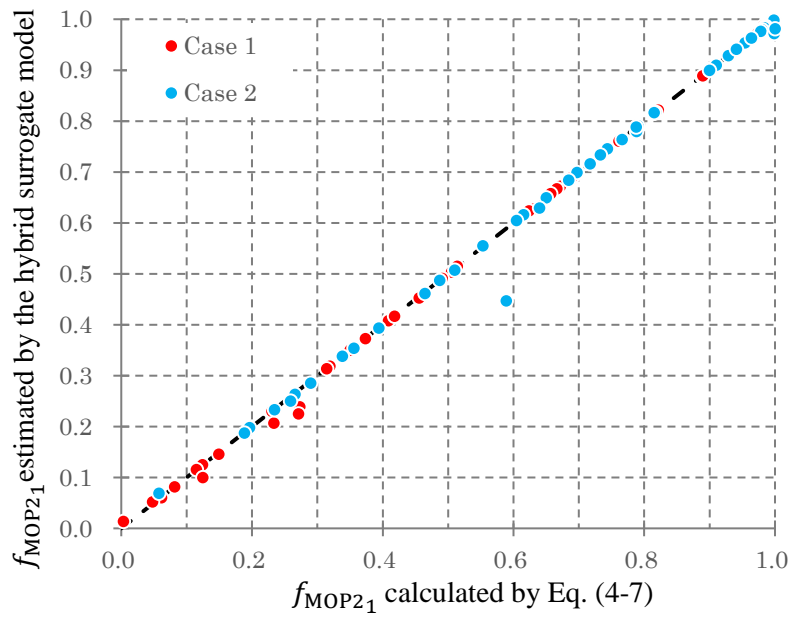
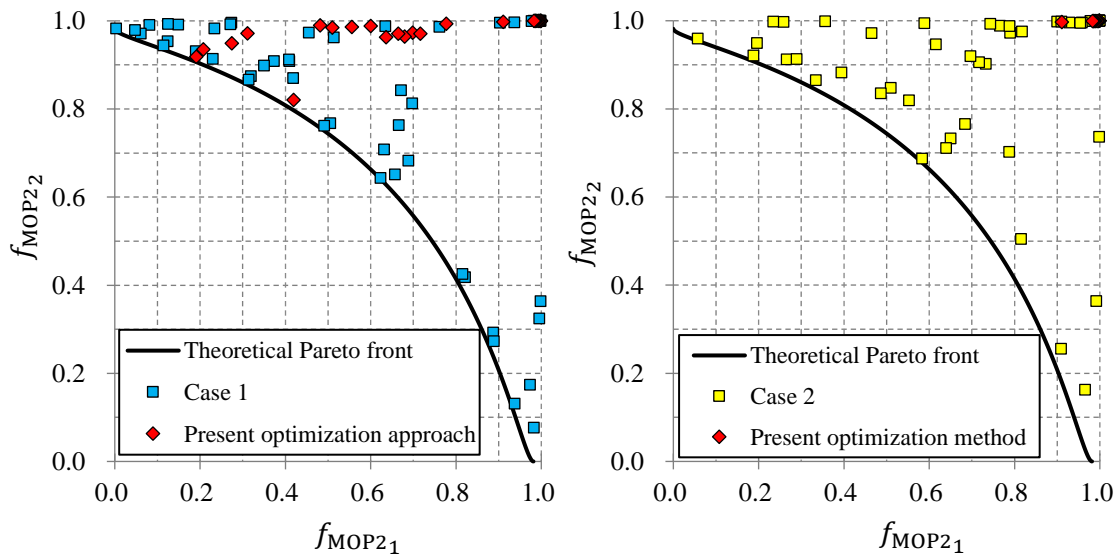


Figure 4-18 LOOCV results for each proposed approach case.



(a) Case 1 (Number of main loop iterations was 25) (b) Case 2 (Number of main loop iterations was 10)

Figure 4-19 Additional sampling result for each case (Number of main loop iterations was matched).

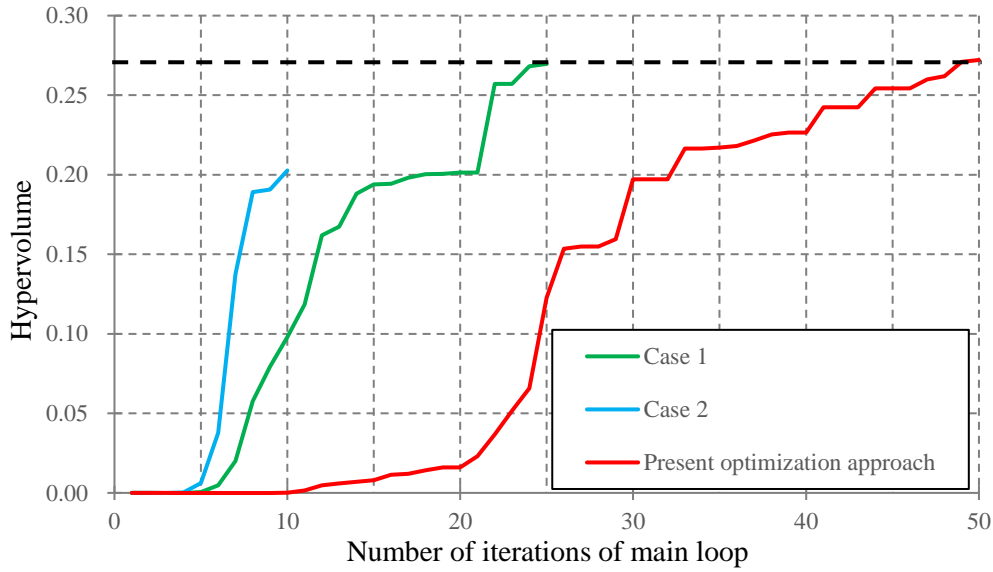


Figure 4-20 History of hypervolume.

4.4.1.2 Expected Hyper-Volume Improvement (EHVI)

The expected hyper-volume improvement (EHVI) value [10], instead of the EI, was used as an indicator of the selection of additional samples. EHVI is based on the theory of the hyper-volume indicator (HV) [12]. The concepts of HV and hyper-volume improvement (HVI) are shown in Figure 4-21. HV as an area is dominated by non-dominated solutions and upper-limited to a reference point. In other words, this area consists of an m -dimensional orthogonal polyhedron, and HV can be regarded as a sum set of hyper-rectangles that is parallel to the axis and shares the reference points. HVI is defined as the difference of HV between a current and new HV that is calculated by adding a new sample point \mathbf{x}_{dv} and reconstructing new response surfaces for all objective functions. EHVI can be regarded as an expected value that indicates by how much HVI would improve or the probability of the new sample point \mathbf{x}_{dv} becoming a non-dominated solution on the reconstructed response surface added to \mathbf{x}_{dv} . Assuming the number of objective functions to be M , EHVI can be expressed as follows:

$$EHVI \left[f_{obj_1}(\mathbf{x}_{dv}), f_{obj_2}(\mathbf{x}_{dv}), \dots, f_{obj_M}(\mathbf{x}_{dv}) \right] = \int_{-\infty}^{f_{obj_1}|_{ref}} \int_{-\infty}^{f_{obj_2}|_{ref}} \dots \int_{-\infty}^{f_{obj_M}|_{ref}} HVI \left[f_{obj_1}(\mathbf{x}_{dv}), f_{obj_2}(\mathbf{x}_{dv}), \dots, f_{obj_M}(\mathbf{x}_{dv}) \right] \times \phi_1(F_{rv_1})\phi_2(F_{rv_2}) \dots \phi_M(F_{rv_M})dF_{rv_1}dF_{rv_2} \dots dF_{rv_M} \quad (4-12)$$

If EHVI is used as the indicator for additional sampling, one sample will be enough per additional sampling when the number of objective functions is more than one.

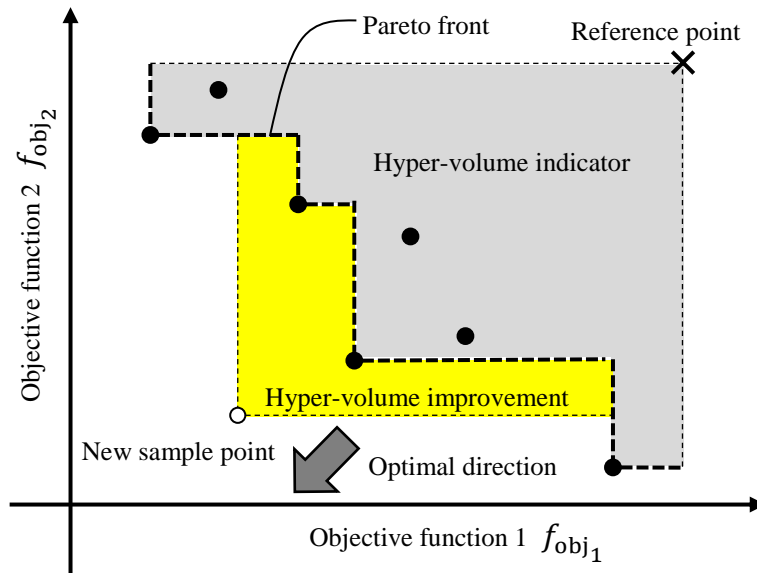


Figure 4-21 Concept of HVI (when the number of the object functions is two).

4.4.2 Design Problems

4.4.2.1 Design Targets and Design Cases

The JAXA's SSBJ concept model, described in Section 4.3.1, was used as the base for the backward-swept wing configuration. In this study, airfoil distributions of a forward-swept wing configuration (based on the planform of $\Lambda = -30^\circ$ configuration described in Section 4.3), named Case 1, and a backward-swept wing configuration (based on the planform of $\Lambda = 52^\circ$ configuration described in Section 4.3), named Case 2 were designed. An overview of the planforms, indicating the locations of the defined cross sections, is shown in Figure 4-22. The other components of both configurations were the same as in the SSBJ concept model, except for the wing.

In this study, a dihedral angle was considered for roll stability. In general, in a backward-swept wing, the produced roll moment is negative and proportional to the sine of twice the backward-swept angle. Thus, considering only roll stability, adding a backward-swept angle is equivalent to adding a dihedral angle. On the contrary, for a forward-swept wing, the forward-swept angle produces a negative dihedral effect. A backward-swept angle of 10° is said to provide approximately 1° of effective dihedral [13]. The dihedral angle of Case 2 was set as 0° . To balance the roll stability of both cases, the dihedral angle of Case 1 was set as 8° considering that the difference of backward-swept angle between each case was approximately 80° .

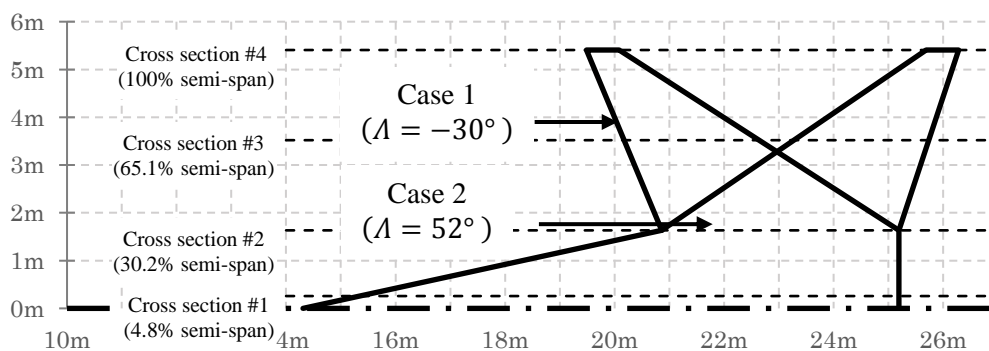


Figure 4-22 Cross sections of airfoil definition.

4.4.2.2 Design Space

The design space was defined for the four cross sections shown in Figure 4-22. The airfoil geometries of the definition cross sections were formed using modified PARSEC method to the twisted angle already described in Section 3.5.2. The airfoil inside Cross section #1 had the same geometry as that of Cross section #1. The geometry between other cross sections were interpolated by a spline curve. Design variables in this design problem are summarized in Table 4-6 and Table 4-7. The maximum thickness for each definition cross section was fixed, and were equivalent to JAXA's SSBJ concept model.

Table 4-6 Design space regarding thickness distribution.

		Lower bound	Upper bound	
Curvature radius at the leading edge	Cross section #1	<i>dv1</i>	0.00005	0.00200
	Cross section #2	<i>dv2</i>	0.0001	0.0010
	Cross section #3	<i>dv3</i>	0.0001	0.0010
	Cross section #4	<i>dv4</i>	0.0001	0.0010
Location of maximum thickness	Cross section #1	<i>dv5</i>	0.4	0.6
	Cross section #2	<i>dv6</i>	0.3	0.5
	Cross section #3	<i>dv7</i>	0.3	0.5
	Cross section #4	<i>dv8</i>	0.3	0.5
Curvature at maximum thickness	Cross section #1	<i>dv9</i>	-0.3	0.0
	Cross section #2	<i>dv10</i>	-0.2	0.0
	Cross section #3	<i>dv11</i>	-0.2	0.0
	Cross section #4	<i>dv12</i>	-0.2	0.0
Opening angle at the trailing edge	Cross section #1	<i>dv13</i>	0.0	6.0
	Cross section #2	<i>dv14</i>	0.0	5.0
	Cross section #3	<i>dv15</i>	0.0	5.0
	Cross section #4	<i>dv16</i>	0.0	5.0

Table 4-7 Design space regarding camber and twisted-down angle of airfoil.

		Lower bound	Upper bound	
Curvature radius of the camber at the leading edge	Cross section #1	<i>dv17</i>	0.000	0.001
	Cross section #2	<i>dv18</i>	0.000	0.001
	Cross section #3	<i>dv19</i>	0.000	0.001
	Cross section #4	<i>dv20</i>	0.000	0.001
Location of maximum camber	Cross section #1	<i>dv21</i>	0.2	0.5
	Cross section #2	<i>dv22</i>	0.2	0.5
	Cross section #3	<i>dv23</i>	0.2	0.5
	Cross section #4	<i>dv24</i>	0.2	0.5
Maximum camber height	Cross section #1	<i>dv25</i>	0.000	0.025
	Cross section #2	<i>dv26</i>	0.00	0.02
	Cross section #3	<i>dv27</i>	0.00	0.02
	Cross section #4	<i>dv28</i>	0.00	0.02
Curvature at the maximum camber	Cross section #1	<i>dv29</i>	-0.2	0.0
	Cross section #2	<i>dv30</i>	-0.2	0.0
	Cross section #3	<i>dv31</i>	-0.2	0.0
	Cross section #4	<i>dv32</i>	-0.2	0.0
Angle of the trailing edge	Cross section #1	<i>dv33</i>	-5.0	1.0
	Cross section #2	<i>dv34</i>	-2.0	4.0
	Cross section #3	<i>dv35</i>	-2.0	4.0
	Cross section #4	<i>dv36</i>	-2.0	4.0
Twisted-down angle of the airfoil	Cross section #1	<i>dv37</i>	-2.0	0.0
	Cross section #2	<i>dv38</i>	-1.0	4.0
	Cross section #3	<i>dv39</i>	-1.0	4.0
	Cross section #4	<i>dv40</i>	0.0	5.0

4.4.2.3 Objective Function and Constrains

The objective functions pertaining to the simultaneous reduction of drag and sonic boom in the supersonic cruise condition can be defined as follows:

$$\left\{ \begin{array}{l} \text{Minimize: } C_{DP} \\ \text{Minimize: PL} \end{array} \right. \quad \text{at } M_{\infty} = 1.4$$

$$\text{Subject to } L = W$$

$$X_{CP} = X_{CG}$$

Through the aerodynamic evaluation, the C_{DP} and PL values of each case under the freestream condition and two constraints described in Section 4.2.1 were calculated.

4.4.3 Results and Discussion

4.4.3.1 Sampling Results

In these optimization problems, 30 samples were evaluated with the high-fidelity solver as the initial samples and the low-fidelity solver evaluated 159 samples for Case 1 and 164 samples for Case 2 as the auxiliary samples. Each initial and auxiliary sample of Case 1 had the same combination of design variable values as those of Case 2. The number of sub loop iterations was five and the number of main loop iterations was four. In this optimization, the total generation number was 100 and the size of population was 20.

The sampling results are shown in Figure 4-23. In both cases, the obtained PL solutions were lower than the baseline of each case. However, drag solutions that were lower than the baseline of each case, were not obtained. These results suggest that it was more difficult to search for low-drag solutions than to search for low-PL solutions in this design problem.

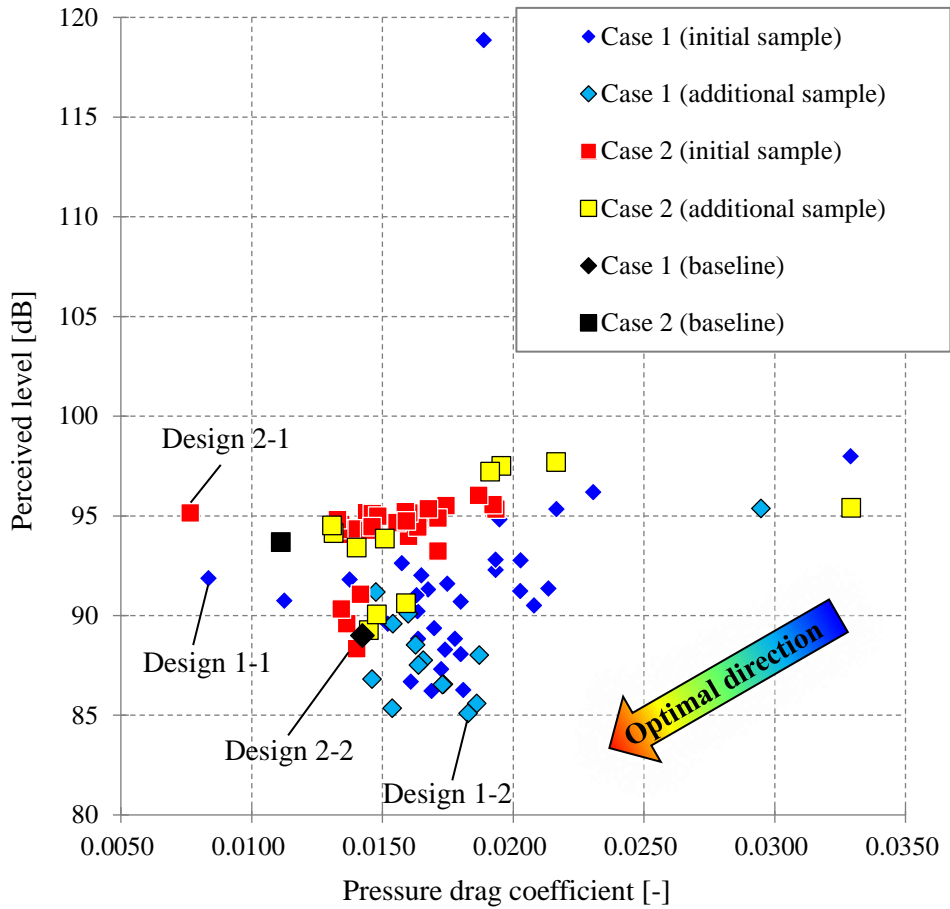


Figure 4-23 Sampling result.

4.4.3.2 Knowledge Discovery by Functional ANOVA

The contribution ratio of the design variables to each objective function based on the functional ANOVA is shown in Figure 4-24. The figure shows that design variables with high contribution ratios depend on each objective function. Especially, design variables related to cambers showed high contribution ratios in each objective function. It is presumed that the design variables of camber geometry contributed to reducing the drag and the PL rather than those of thickness distribution.

Focusing on drag reduction, two design variables $dv20$ (the curvature radius of the camber at the leading edge at Cross section #4) and $dv30$ (the curvature at the maximum camber at Cross

section #2) occupied approximately half of the contribution ratio in Case 1. In Case 2, several design variables, such as $dv24$ (the location of maximum camber at Cross section #4), $dv16$ (the opening angle at the trailing edge at Section #4), and $dv30$ (the curvature at the maximum camber at Cross section #2) indicated high contribution ratios on an average. In both cases, these design variables did not include inboard wing parameters because most of the lift was caused at the outboard wing.

Considering the reduction of the PL, $dv36$ (the angle of camber trailing edge at Cross section #4) made a significant contribution because the wing tip of the forward-swept wing passed through the freestream before the mid-span wing and affected the shock wave generation. Other design variables, such as $dv34$ (the angle of camber trailing edge at Cross section #2), $dv13$ (the opening angle at the trailing edge at Cross section #1), and $dv3$ (the curvature radius at the leading edge at Cross section #3) indicated high contribution ratio in Case 1. However, in Case 2, three design variables $dv15$ (the opening angle at the trailing edge at Cross section #3), $dv2$ (the curvature radius at the leading edge at Cross section #2), and $dv29$ (the curvature at the maximum camber at Cross section #1) accounted for over 90% of the whole contribution ratio. $Dv2$ and $dv29$, which involved the airfoil geometry distribution of the inboard wing, were ranked among these three design variables because, the inboard wing came in contact with the freestream before the outboard wing in the backward-swept wing. Thus, the inboard wing affected the shock wave generation rather than the outboard wing.

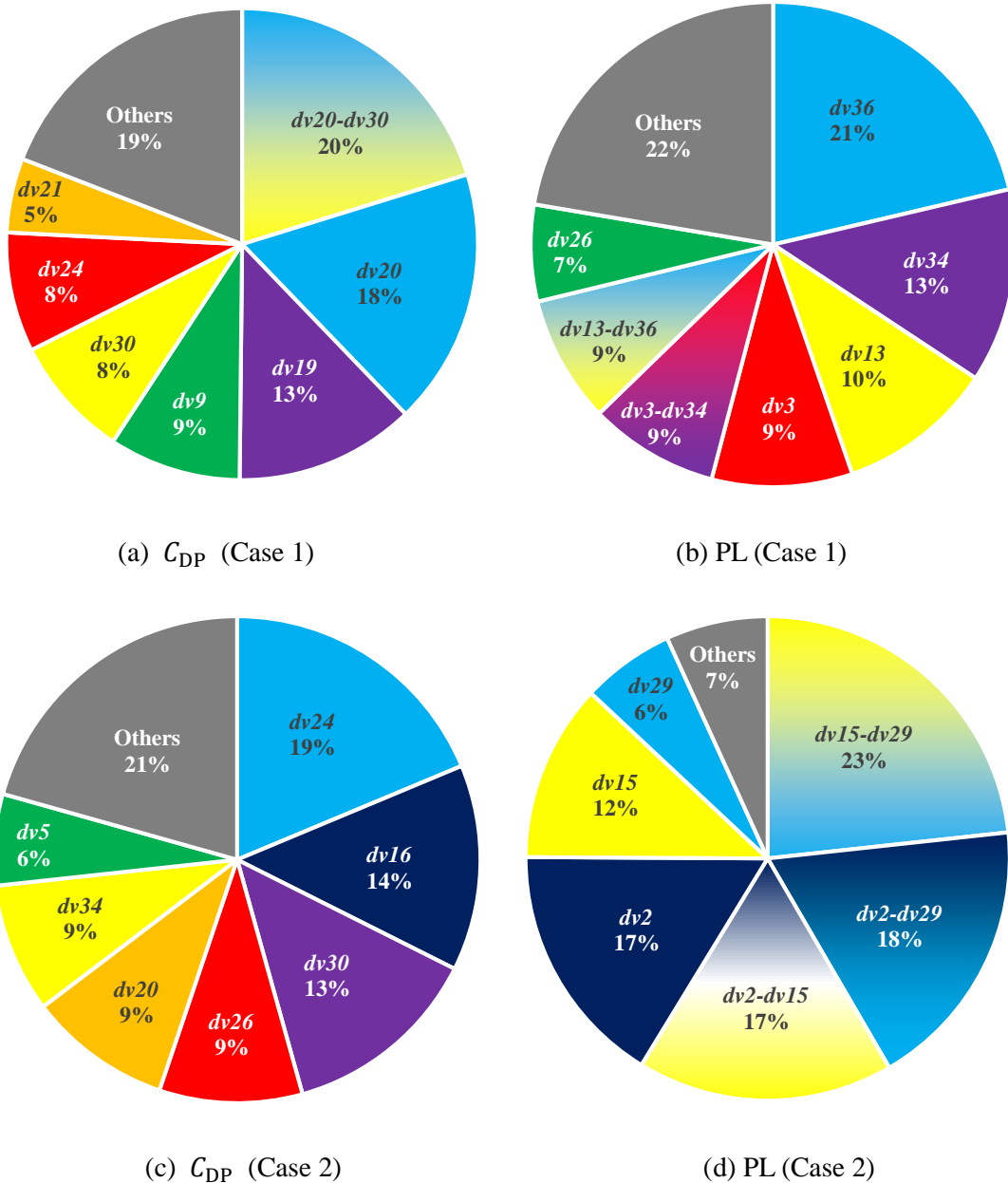


Figure 4-24 Contribution ratios of design variables to each objective function.

(The color of each element corresponds to each design variable.)

4.4.3.3 Comparison between Representative Solutions

In Figure 4-23, the lowest C_{DP} solutions among the Case 1 and Case 2 solutions are named Design 1-1 and Design 2-1, respectively. The lowest PL solutions among the Case 1 and Case 2

solutions are named as Design 1-2 and Design 2-2, respectively. Figure 4-25 presents surface C_p distributions for these solutions. Airfoil geometries of these solutions are shown in Figure 4-26.

When focusing on drag reduction in Figure 4-25(a) and (b), a shock wave was observed in Design 1-1 on the entire lower surface area of the outboard wing's leading edge, while no shock wave was observed in Design 2-1. This shock wave produces wave drag; thus, Design 2-1 has a lower-drag than Design 1-1. When observing Cross section #4 (tip) airfoil geometries in Figure 4-26(a), which highly contributed to drag reduction, the shape of the leading edge of Design 1-1 was similar to that of Design 2-1. The differences in airfoil geometry between Design 1-1 and Design 2-1 is that the former has a twisted-down angle and the latter has a camber shape. Cross sectional C_p distribution of these airfoils are shown in Figure 4-27(a) and (b). In Figure 4-27(a), a negligible pressure difference between the upper and lower surfaces can be seen because the tip camber of Design 1-1 is small. On the other hand, a large pressure difference between the upper and lower surfaces can be seen in Figure 4-27(b), before the lift because the camber of Design 2-1 was larger than that of Design 1-1. In forward-swept wing, the wing tip touched the freestream much earlier in the wing, and thus, the camber of the wing tip became smaller in order to avoid shock wave generation. On the contrary, in backward-swept wing, the wing tip touched the freestream much later in the wing, and thus, the camber of the wing tip was not critical in reducing wave drag when compared to the forward-swept wing.

Comparing airfoil geometries at Cross section #2 of both configurations described in Figure 4-26(b), the curve at the upper leading edge of Design 1-2 was gentler than that of Design 1-1. Therefore, in Figure 4-25(a) and (c), no shock wave was observed from the lower surface leading edge of the kink to that of the mid-span of the outboard wing in Design 2-1, while a shock wave was observed on the entire area of lower surface of leading edge of the outboard wing in Design 1-1. When comparing airfoil geometries at Cross section #2 of the both configurations described

in Figure 4-26(c), the maximum camber height of Design 2-2 was smaller than that of Design 1-1; thus, negative pressure on upper surface around the mid-span wing of Design 2-2 was weaker than that of Design 2-1, which is described in Figure 4-25(c) and (d). The pressure signatures of minimum PL solutions are shown in Figure 4-28 and Figure 4-29. For near-field pressure signature described in Figure 4-28(a), Peak A of Design 1-2 was stronger than that of Design 2-2 because of Design 1-2's shock waves around the outboard wing's leading edge. In Figure 4-27(c), this shock wave was clearly observed. After this shock wave, an expansion area at the leading edge of the lower surface was also observed. The shock wave and this expansion area produced drag, and thus, Design 1-2 had a larger drag than Design 1-1. In addition, this expansion area corresponded to Peak B in Figure 4-28(a). According to Figure 4-29, Peak B remained on the ground, and thus, a stepwise pattern was generated in Design 1-2. This stepwise pattern was not observed in Design 2-2. This difference caused Design 1-2 to have a lower PL than Design 2-2.

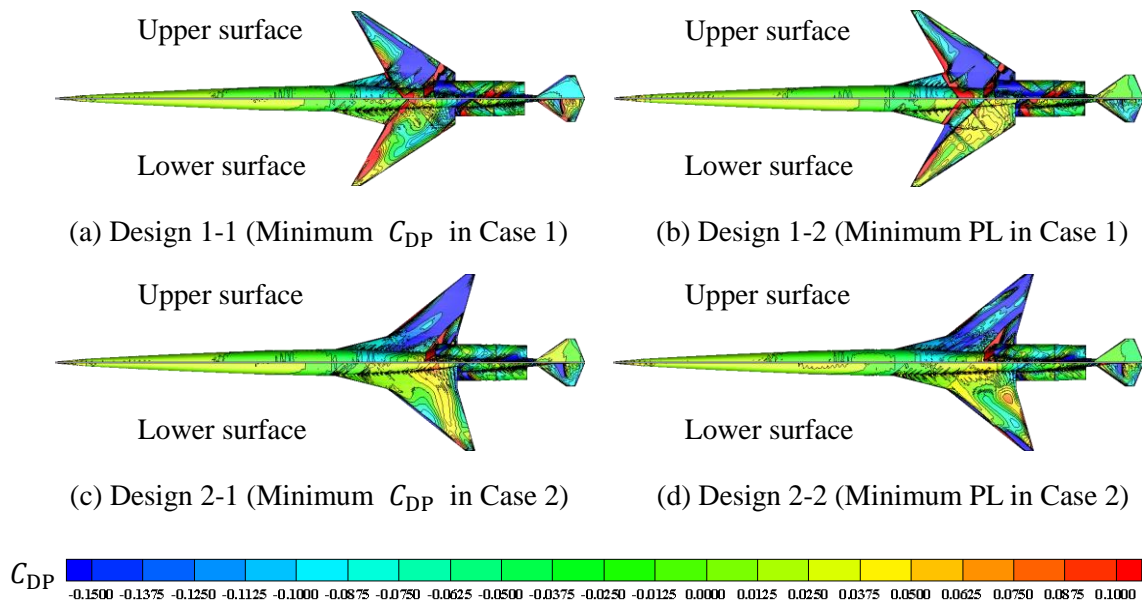
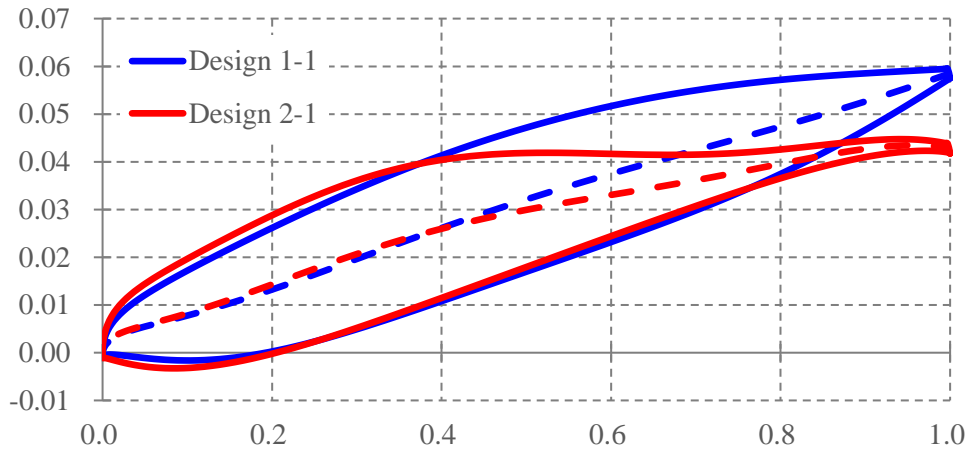
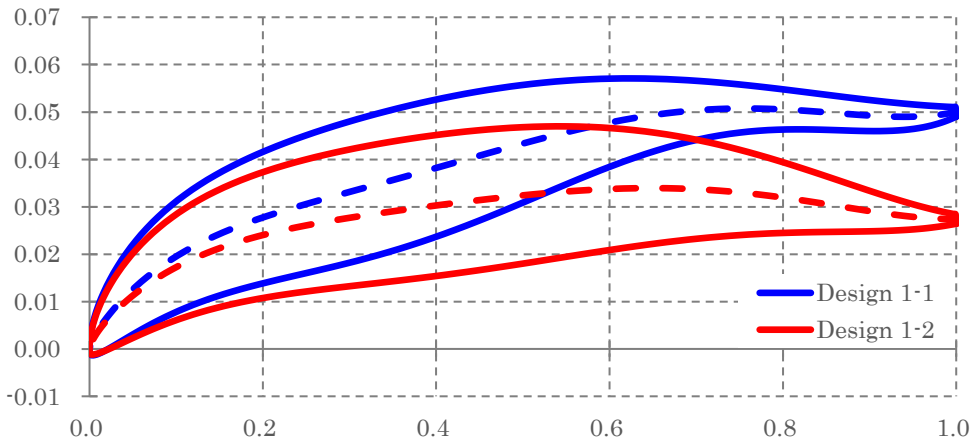


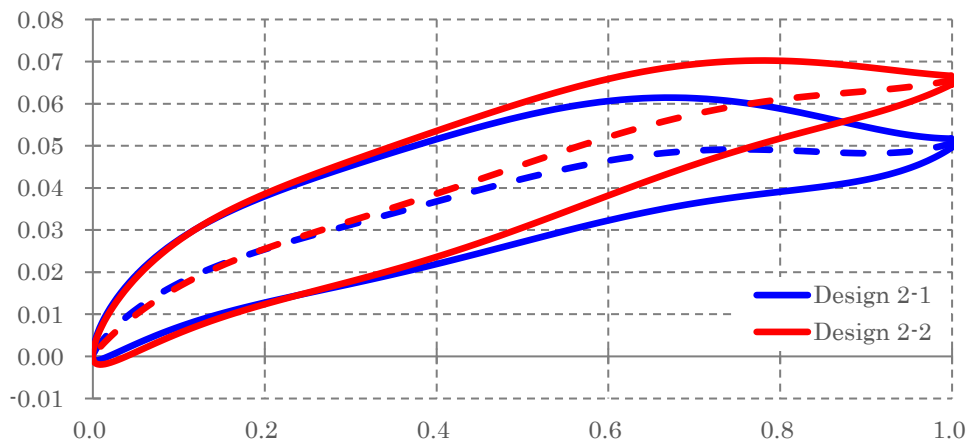
Figure 4-25 Surface C_p distributions for representative solutions.



(a) Cross section #4 (Minimum C_{DP} configuration in each case)



(b) Cross section #2 (Case 1)



(c) Cross section #2 (Case 2)

Figure 4-26 Airfoil geometries of representative solutions.

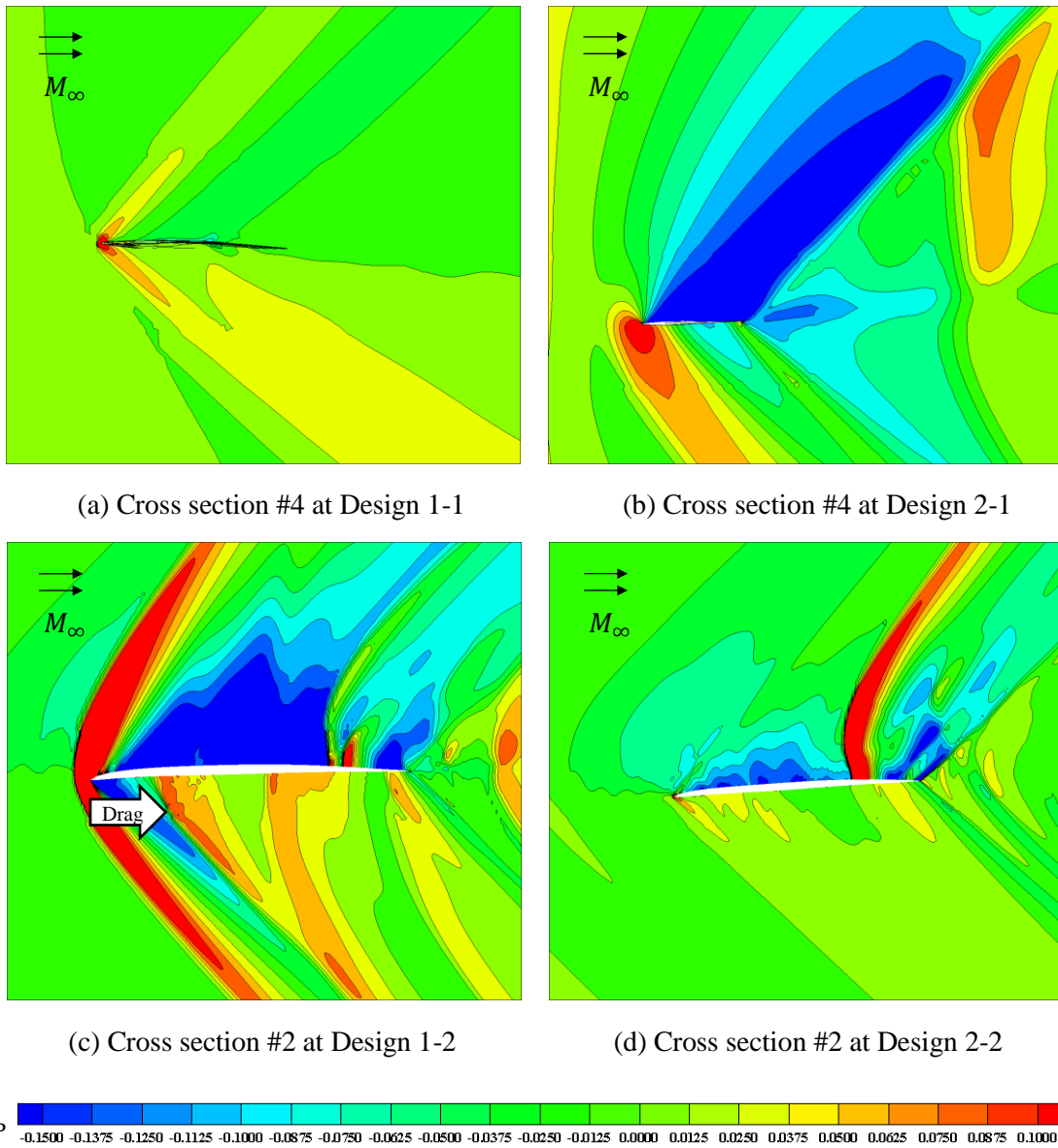


Figure 4-27 Cross sectional C_p distributions for representative solutions.

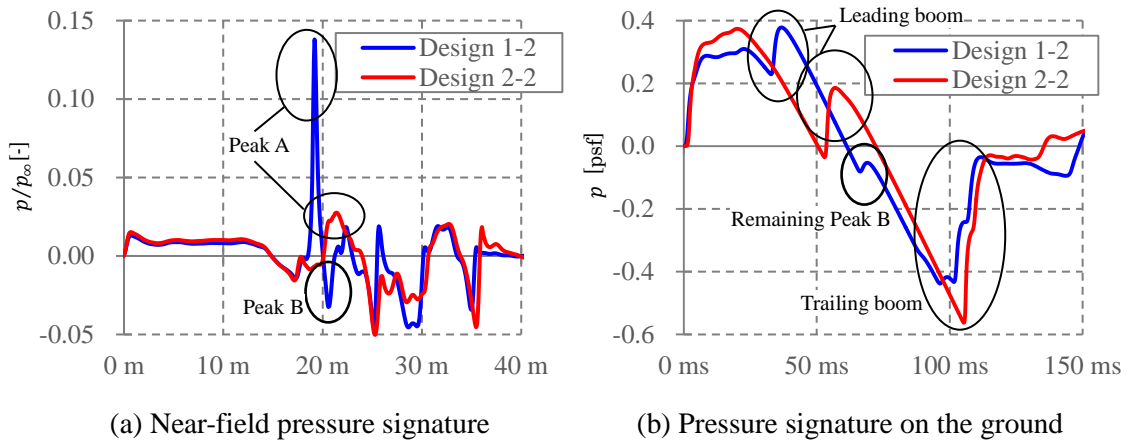


Figure 4-28 Pressure signature for minimum PL solutions.

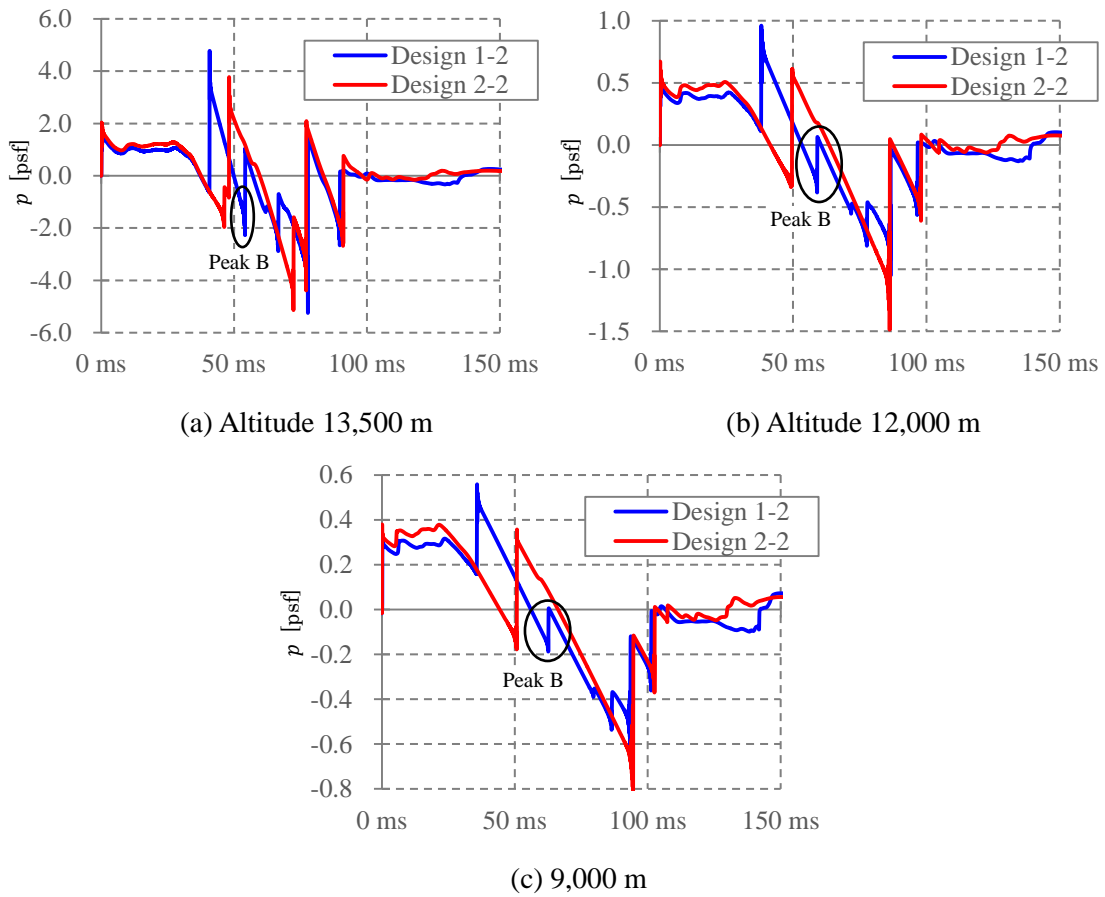


Figure 4-29 Pressure signatures for minimum PL solutions during the process of propagating to the ground.

4.5 Conclusion

In this chapter, the simultaneous reduction of aerodynamic drag and the impact of sonic boom was considered in the aerodynamic design of an airfoil for a forward-swept wing and a backward-swept wing. To improve exploration efficiency, multi-objective, multi-fidelity efficient global optimization with a multi-additional sampling was proposed. The proposed approach was demonstrated by solving MOP2, a test problem in Van Valedhuizen's test suite, before applying it to the wing design problems. The test results revealed that the proposed approach obtained more non-dominant solutions near the theoretical Pareto front than the present optimization approaches because the proposed approach obtained more additional samples than the present optimization approach per additional sampling loop.

Before applying the proposed approach to aerodynamic wing design, a parametric study was conducted to investigate aerodynamic drag and sonic boom performance of a forward-swept wing. The PL value of the forward-swept wing was lower than that of the backward-swept wing and the maximum PL difference between them was approximately 4.8 PLdB. The comparison of pressure signatures showed, stepwise patterns at the trailing boom of the pressure signature will become more remarkable with a decrease in the backward-swept angle; thus, the PL value was decreased.

The optimal wing design results for the forward-swept wing and backward-swept wing suggested that the optimal airfoil distributions and high contributed design variables to minimize drag and the impact of sonic booms differ by planform.

Reference

- [1] Horinouchi, S., “Conceptual Design of A Low Sonic boom SSBJ”, JAXA Research and Development Report, JAXA-RR-05-045, 2007, (in Japanese).
- [2] Page, J. A. and Plotkin, K. J., “An Efficient Method for Incorporating Computational Fluid Dynamics into Sonic boom Prediction”, AIAA Paper 91-3275, Maryland, 1991. <https://doi.org/10.2514/6.1991-3275>
- [3] Yamamoto, M., Hashimoto, A., Takahashi, T., Kamakura, T. and Sakai, T., “Long-Range Sonic boom Prediction Considering Atmospheric Effects”, Inter-noise 2011, September, 2011.
- [4] Makino, Y., Naka, Y., Hashimoto, A., Kanamori, M., Murakami, K. and Aoyama, T., “Sonic boom Prediction Tool Development at JAXA”, *Aeronautical and Space Sciences Japan*, Vol.7, Issue 7 (2013), pp. 237-242. https://doi.org/10.14822/kjsass.61.7_237
- [5] Stevens, S. S. “Perceived Level of Noise by Mark VII and Decibels (E)”, *The Journal of the Acoustical Society of America*, Vol. 51, No. 575 (1972), pp. 575-601. <https://doi.org/10.1121/1.1912880>
- [6] Roy, C. J., “Grid Convergence Error Analysis for Mixed-Order Numerical Schemes”, *AIAA Journal*, Vol.41, No.4 (2003), pp.595-604.
- [7] Horinouchi, S., “Conceptual Design of a Low Boom SSBJ, 43rd AIAA Aerospace Sciences Meeting and Exhibit”, AIAA Paper 2005-1018, 2005. <https://doi.org/10.2514/6.2005-1018>
- [8] Nakamichi, J., Ejiri, H., Kikuchi, T., Minegishi, M., Sotozaki, T., Kumakura, I., Noguchi, Y., and Isogai, K., “On The Aeroelastic Characteristics of The Forward Swept Wing Optimized by Aeroelastic Tailoring”, Technical Report of National Aerospace Laboratory, TR-1208, 1993, (in Japanese).
- [9] Isogai, K., “空力弾性テーラリングの歩みと展望”, *Aeronautical and Space Sciences Japan*, Vol.44, No.511, 1996, pp.461-465 (in Japanese). <https://doi.org/10.2322/jjsass1969.44.461>
- [10] Laniewski-Wollk, L., Obayashi, S. and Jeong, S., “Development of Expected Improvement for multi-objective problem”, JSASS Paper 2010-0168, June 2010.
- [11] Huband, S., Hingston, P., Barone, L. and While, L., “A Review of Multiobjective Test Problems and A Scalable Test Problem Toolkit”, *IEEE Transactions on Evolutionary Computation*, Vol.10, Issue 5, 2006, pp.477-506. <https://doi.org/10.1109/TEVC.2005.861417>
- [12] Zitzler, E. and Thiele, L., “Multiobjective Optimization Using Evolutionary Algorithms – A Comparative Case Study”, *Proceeding the 5th International Conference on Parallel Problem Solving from Nature*, 1998, pp.292-301. <https://doi.org/10.1007/BFb0056872>

Chapter 4

- [13] Raymer, D., "Aircraft Design: A Conceptual Approach Fourth Edition", *Amer Inst of Aeronautics*, 2006.

Chapter 5 Conclusion

This paper discussed planform dependency on a supersonic wing to enhance aerodynamic performance and sonic boom under cruise condition by developing an improved-efficiency design method. The objective of this research was to obtain design knowledge regarding the relationship between supersonic wing planforms and to reduce in aerodynamic drag and sonic booms using the proposed design method. In the proposed approach, an efficient global optimization (EGO) method employing a hybrid surrogate model was used along with a multi-fidelity approach and extended multi-additional sampling extended to solve multi-objective optimization problems.

The second chapter of this dissertation discussed the aerodynamic design optimization of an airfoil to reduce the aerodynamic drag for cranked arrow and single-tapered wings under transonic and supersonic cruise conditions using EGO. The design results suggested that the trend of optimal airfoil geometries differed for different cruise speeds. At supersonic speeds, the cranked arrow and single-tapered wings were similar from the viewpoint of effective design variables; this is because the aim to reduce wave drag defines the camber height of the kink airfoil. On the contrary, at transonic speeds, the dominant design variables of the two wings were different. In the cranked arrow wing, the camber height of the kink airfoil was dominant for supersonic speeds. In the single-tapered wing, the design variables for the tip were dominant owing induced drag at.

In the third chapter, the performance of different supersonic wing planform shapes for different backward-swept angles and an integrated engine intake were investigated. The airfoil geometry distributions of the wings were designed to minimize aerodynamic drag under supersonic cruise conditions using a quadruple-tapered wing with a large backward-swept angle and a single-tapered wing with a small backward-swept angle, employing multi-fidelity EGO using the hybrid surrogate model. According to the design results, the front camber shape and twist angle of the mid-span cross section were most efficient to promote drag reduction, irrespective of the wing

Chapter 5

planform shape. However, the optimal airfoil geometries differed between planforms.

In the fourth chapter, the aerodynamic design problems of an airfoil for the forward- and backward-swept wings under supersonic cruise condition to reduce aerodynamic drag and the impact of sonic booms were investigated using the proposed approach. In this case, to improve design efficiency, multi-additional sampling was integrated with the multi-fidelity approach. In addition, the expected hyper-volume improvement was introduced as an additional sampling criterion to solve the multi-objective problem. Before solving the design problems, a parametric study was conducted to demonstrate the performance of the sonic boom for forward-swept wings. As a result, selecting forward and backward- wings with a small backward-swept angle was confirmed to be an effective solution to a stepwise-pattern trailing boom to reduce the PL value. By solving optimal wing design problems for forward- and backward-swept wings using the proposed approach, knowledge regarding planform dependency on a supersonic wing for simultaneous reduction in the aerodynamic drag and sonic boom during cruising was obtained; for example, the optimal airfoil distributions and design variables that considerably contributed to minimize drag, and the impact of sonic booms differ between each planform. In addition, the proposed approach was demonstrated by solving a mathematical test problem before applying it to the wing design problems; the results demonstrated that the proposed approach can obtain non-dominant solutions near the theoretical Pareto front earlier than present optimization approaches because the proposed approach can obtain a higher number of additional samples than the present optimization approach per additional sampling loop.

Toward realizing innovative SST, several studies using the knowledge of planform dependency on a supersonic wing obtained in this study are required. The knowledge obtained from this study will help simultaneously design wing and tail wing for sonic boom reduction and improve forward-swept wing planform for wave drag reduction. Supersonic forward-swept wing should

be investigated from a broader perspective because of still a few researches and knowledge regarding supersonic forward-swept wing including this study. According to these studies, an original SST concept model can be proposed.

The proposed approach, the multi-fidelity multi-objective multi-additional sample optimization can be applied to solve the aerodynamic design problem for SST wing as well as other disciplinary design problems. Further, numerical simulation can substitute experimental evaluation for the high-fidelity evaluation. Thus, the proposed approach can be applied to solve other design problems such as thermal, structural or mechanical dynamic designs for industrial products.